

# THE INITIATION OF ELECTRIC ARCS AND THE POSSIBLE IMPACT IN INDUSTRIAL ENVIRONMENTS

A thesis presented in fulfilment of the requirement for  
the degree of

**Doctor of Philosophy**

**Sotiria G. Koutoula**

**2018**

**Department of Electronic and Electrical Engineering**

**University of Strathclyde**

**Glasgow, UK**

# Declaration of Authenticity and Author's Rights

‘This thesis is the result of the author’s original research. It has been composed by the author and has not been previously submitted for examination which has led to the award of a degree.’

‘The copyright of this thesis belongs to the author under the terms of the United Kingdom Copyright Acts as qualified by University of Strathclyde Regulation 3.50. Due acknowledgement must always be made of the use of any material contained in, or derived from, this thesis.’

Signed:

Date:

# Acknowledgements

---

First of all, I would like to acknowledge Dr. Igor Timoshkin for his amazing supervision, guidance and help without whom this project and thesis would have never been finished. I would also like to acknowledge Prof. Martin Judd for his supervision during the first two years of this research project without whom this project would never have started.

I kindly acknowledge the University of Strathclyde and GSE Systems to jointly funding this research. Moreover, I would like to thank the industrial collaborator, Emma Harrison, for her valuable contribution and for providing industrial data.

Many thanks to Dr. Nina Roscoe and the whole HVT Research Group for the opportunities and support provided and the High Voltage Mechanical Workshop for their help manufacturing the experimental set-up.

In particular, special thanks to my good friends Dr. Athanasios Mermigkas and Mohammad Burhan Tariq who were always willing to take the time to help and support me throughout my PhD. Furthermore, many thanks to Frank Cox for his assistance in the lab during manufacturing the voltage-dividing current shunt.

Special thanks to Prof. Pantelis Mikropoulos and Konstantinos Kerasnoudis for inspiring discussions during my holiday breaks, especially regarding black-box modelling with the former one.

I would also like to thank all my friends who tolerated my strange behaviour during my PhD, especially Konstantia Zisi, Kyriaki-Nefeli Malamaki and Georgia Tsigara.

My warmest and deepest sense of gratitude goes to my parents, Giorgos Koutoulas and Efi Sotiroudi, my brother Stergios Koutoulas, and my grandmother Pasxalina Sotiroudi who gave me support, encouragement and unconditional love.

Most importantly, I would like to express my gratitude to my partner, Ignatios Athanasiadis who gave me support and encouragement during the difficult periods of my PhD. Also, his significant contribution in developing my coding skills and my understanding in continuum mechanics is dearly appreciated.

# Abstract

---

Advancing knowledge and understanding of electrical arc flash and arc blast hazards through experimentation, modelling and analysis is the main goal of the present thesis. To achieve this, initially, significant work has been carried out to analyse existing data on arc flash hazards and mitigation engineering practices in industrial premises. Then, experimental investigations on the electrical arc characteristics have been conducted which together with the development of an analytical model for quantification of arc's energy components have formed the core of the research project. Electrical characteristics of the initial stage of the arc have been obtained experimentally using different test systems developed in the course of this study. Two different arc initiation mechanisms have been examined: self-breakdown spark gap (SBSG) and wire-guided spark gap (WGSG) discharge initiation. Data post-processing techniques have been developed to obtain arc voltage and current waveforms for calculating the electrical arc energy available in the discharge. An analytical model has been developed based on the hydrodynamic approach, to further analyse the energy dissipated and to obtain the energy components associated with thermal, acoustic-kinetic and light emission processes. This analysis of the energy components provides data for safety considerations which are currently not taken into account by the existing standards. Furthermore, analysis and evaluation of the suitability of black-box models for predicting the arc characteristics during its initiation taking into account electric circuit parameters have been performed. Initial conditions for analysis of the ratio of the arc current over voltage have been obtained from experimental waveforms to investigate the arc-electrical circuit interaction. This can be considered as a first step towards establishment of a complete accurate link between the microscale and macroscale manifestation of the arc flash and arc blast phenomena. It is envisaged that further understanding of the complex energy conversion processes taking place in the post-arc-initiation process can provide additional tools for quantifying arc energy components and improving arc flash and arc blast safety.

# Contents

---

<b>ACKNOWLEDGEMENTS.....</b>	<b>II</b>
<b>ABSTRACT.....</b>	<b>III</b>
<b>CONTENTS.....</b>	<b>IV</b>
<b>NOMENCLATURE.....</b>	<b>IX</b>
ABBREVIATIONS.....	IX
GREEK SYMBOLS.....	X
ROMAN SYMBOLS.....	XI
<b>CHAPTER 1 .....</b>	<b>1</b>
<b>INTRODUCTION.....</b>	<b>1</b>
1.1 MOTIVATION.....	1
1.2 AIM AND OBJECTIVES.....	2
1.3 NOVELTY.....	4
1.4 THESIS STRUCTURE.....	5
<b>CHAPTER 2 .....</b>	<b>7</b>
<b>LITERATURE REVIEW.....</b>	<b>7</b>
2.1 ELECTRICAL DISCHARGE FUNDAMENTALS.....	7
2.1.1 Breakdown in gases.....	8
2.1.2 Electrical gas discharge properties.....	8
2.1.3 Townsend discharge theory and Paschen's law.....	11
2.1.4 Streamer discharge theory.....	13
2.1.5 Spark discharge and arc discharge.....	14
2.1.6 Arc plasma transient impedance.....	16
2.2 THERMODYNAMICS AND FLUID DYNAMICS PRINCIPLES.....	17
2.2.1 Energy balance equation.....	18
2.3 ARC MODELS.....	19
2.4 ARC FLASH AND ARC BLAST INCIDENT.....	20
2.4.1 Arcing and bolted faults.....	20
2.4.1.1 Bolted fault.....	20
2.4.1.2 Arcing fault.....	21

2.4.2 Arc flash and arc blast hazards.....	22
2.4.2.1 Description of the phenomenon .....	22
2.4.2.2 Common causes of arc flash and arc blast incidents .....	25
2.5 RISK MANAGEMENT AND MITIGATION METHODS .....	25
2.5.1 Risk Management .....	26
2.5.2 Mitigation Methods .....	27
2.6 PREVENTION .....	27
<b>CHAPTER 3 .....</b>	<b>29</b>
<b>ARC FLASH STUDIES REVIEW .....</b>	<b>29</b>
3.1 ELECTRICAL SAFETY AND ARC FLASH CODES AND STANDARDS .....	30
3.1.1 IEEE Std. 1584 and NFPA 70E – USA.....	30
3.1.2 UK and Europe.....	30
3.1.3 Complying with the safety requirements .....	31
3.2 METHODOLOGY TO ASSESS ARC FLASH SEVERITY .....	31
3.2.1 Contributing factors to the arc flash intensity and severity.....	32
3.2.2 Basic steps to complete an arc flash study .....	33
3.2.3 Outcomes of the study.....	35
3.2.3.1 Incident energy calculations at working distance .....	35
3.2.3.2 Calculations of the arc flash protection boundaries.....	36
3.2.3.3 Arc-rated protective clothing and personal protective equipment selection .....	37
3.2.3.4 Arc flash warning labels displaying necessary arc flash information.....	37
3.3 MITIGATION TECHNIQUES AND RISK MANAGEMENT .....	38
3.3.1 State-of-the-art mitigation methods.....	38
3.3.1.1 Reduction of arc incident energy.....	39
3.3.1.2 Reduction of arc flash impact.....	39
3.3.1.3 Methods combination.....	39
3.3.1.4 Other mitigation methods: Practical engineering approaches .....	40
3.3.1.5 Predict and prevent faults.....	40
3.3.2 A comprehensive system to manage arc flash hazards.....	41
3.4 ARC FLASH HAZARD CALCULATION STUDIES RESULTS .....	41
3.5 ARC FLASH HAZARD RISK MITIGATION STUDIES RESULTS .....	45
3.6 CONCLUSIONS .....	48
<b>CHAPTER 4 .....</b>	<b>50</b>
<b>EXPERIMENTAL SET-UP .....</b>	<b>50</b>
4.1 EXPERIMENTAL DESIGN .....	50
4.1.1 Design requirements.....	50
4.1.2 Simplified block diagram of the experimental set-up .....	51

4.1.3	<i>SBSG topology</i> .....	51
4.1.3.1	SBSG equivalent circuit.....	56
4.1.4	<i>WGSG topology</i> .....	56
4.1.4.1	WGSG equivalent circuit.....	59
4.2	DIAGNOSTIC AND MONITORING TECHNIQUES.....	60
4.2.1	<i>Electrical parameters measuring techniques</i> .....	60
4.2.1.1	Current measurements.....	61
4.2.1.2	Voltage Measurements.....	61
4.2.2	<i>Errors and uncertainty</i> .....	62
4.2.2.1	Measurement circuitry rise time and sampling rate.....	62
4.3	PRELIMINARY TESTS AND SIMULATIONS.....	63
4.3.1	<i>Tests</i> .....	64
4.3.1.1	Propagation delay of the cables.....	64
4.3.2	<i>PSpice simulations</i> .....	66
4.3.2.1	Scope input impedance.....	66
4.3.2.2	Probe location.....	68
4.4	CONCLUSIONS.....	69
<b>CHAPTER 5</b>	.....	<b>71</b>
<b>ARC DISCHARGE ELECTRICAL CHARACTERISTICS</b>	.....	<b>71</b>
5.1	WAVEFORMS ACQUISITION.....	71
5.1.1	<i>Procedure</i> .....	71
5.1.2	<i>Lumped element model (LEM)</i> .....	72
5.1.2.1	LEM - SBSG topology.....	73
5.1.2.2	LEM - WGSG topology.....	75
5.1.2.3	Inductance, resistance and capacitance calculations.....	76
5.2	RESISTIVE AND INDUCTIVE VOLTAGE DROPS: SEPARATION METHODOLOGY.....	78
5.3	ARC VOLTAGE AND CURRENT.....	79
5.3.1	<i>Arc voltage</i> .....	80
5.3.1.1	Arc voltage - SBSG topology.....	80
5.3.1.2	Arc voltage - WBSG topology.....	82
5.3.2	<i>Arc current</i> .....	85
5.3.2.1	Arc current - SBSG topology.....	85
5.3.2.2	Arc current - WGSG topology.....	87
5.4	METHODOLOGY TO DETERMINE THE ARC DISCHARGE RESISTANCE.....	88
5.5	EXPERIMENTAL RESULTS.....	91
5.5.1	<i>SBSG topology</i> .....	91
5.5.1.1	Breakdown voltage.....	91
5.5.1.2	Arc current.....	92
5.5.1.3	Arc resistance.....	93

5.5.1.4 Arc energy.....	94
5.5.2 WGSg topology.....	96
5.5.2.1 Stabilised voltage.....	96
5.5.2.2 Arc current.....	97
5.5.2.3 Arc resistance.....	98
5.5.2.4 Arc energy.....	99
5.6 TRANSIENT ARC RESISTANCE.....	100
5.7 CONCLUSIONS.....	103
<b>CHAPTER 6 .....</b>	<b>105</b>
<b>ENERGY PARTITION DURING ARC INITIATION .....</b>	<b>105</b>
6.1 THERMODYNAMICS AND FLUID DYNAMICS PRINCIPLES AND THEIR APPLICATION IN THE ENERGY PARTITION MODEL DEVELOPMENT.....	105
6.1.1 Conservation of energy.....	106
6.1.2 Conservation of mass.....	106
6.1.3 Conservation of momentum.....	107
6.1.4 Model assumptions.....	109
6.2 ENERGY PARTITION MODEL DEVELOPMENT IN SPHERICAL COORDINATES.....	110
6.2.1 Initial conditions.....	115
6.3 SIMULATIONS RESULTS.....	117
6.3.1 Energy partition in SBSg topology.....	118
6.3.2 Energy partition in WGSg topology.....	122
6.3.3 Acoustic pressure approximation.....	126
6.4 SHOCK-WAVE APPROXIMATION.....	128
6.5 CONCLUSIONS.....	132
<b>CHAPTER 7 .....</b>	<b>134</b>
<b>BLACK-BOX APPROACH TO MODELLING THE INITIAL STAGE OF ARC .....</b>	<b>134</b>
7.1 ARC MODELS.....	134
7.1.1 Physical arc models.....	135
7.1.2 Mathematical black-box arc models.....	135
7.1.2.1 Mayr arc model.....	136
7.1.2.2 Cassie arc model.....	136
7.1.3 Limitations of black-box models.....	137
7.1.4 Research contributions.....	138
7.2 MODEL AND SIMULATIONS.....	138
7.2.1 Circuit analysis.....	139
7.2.2 Ratio of experimental arc current over voltage of the probe waveform calculation using experimental results.....	140



7.2.3 Arc initial conditions .....	141
7.2.4 Simulations results – The Mayr approach.....	142
7.2.4.1 Mayr parameters determination – $\tau_M$ and $P_M$ .....	142
7.2.4.2 Sensitivity of the model: variation of the Mayr parameters ( $\tau_M, P_M$ ).....	144
7.2.5 Simulations results – The Cassie approach.....	146
7.2.5.1 Cassie parameters determination – $\tau_C$ and $U_C$ .....	146
7.2.5.2 Sensitivity of the model: variation of the Cassie parameters ( $\tau_C, U_C$ ).....	149
7.3 CONCLUSIONS .....	151
<b>CHAPTER 8 .....</b>	<b>153</b>
<b>CONCLUSIONS AND FUTURE WORK .....</b>	<b>153</b>
8.1 CONCLUSIONS .....	153
8.1.1 Arc flash studies review.....	153
8.1.2 Arc onset.....	154
8.1.3 Hydrodynamic model analysis .....	155
8.1.4 Black-box model analysis.....	157
8.2 FUTURE WORK.....	157
<b>REFERENCES.....</b>	<b>159</b>
<b>APPENDIX A: PROTECTIVE CLOTHING AND PERSONAL PROTECTIVE EQUIPMENT</b> <b>.....</b>	<b>A.1</b>
<b>APPENDIX B: PCS EQUIVALENT CONSTANT RESISTANCE .....</b>	<b>B.1</b>
<b>APPENDIX C: EXAMPLE OF OBTAINING ARC CURRENT WAVEFORM (SBSG</b> <b>TOPOLOGY) .....</b>	<b>C.1</b>
<b>APPENDIX D: LIST OF PUBLICATIONS .....</b>	<b>D.1</b>

# Nomenclature

---

## Abbreviations

AC	alternating current
ANSI	American National Standards Institute
BJT	bipolar junction transistor
DC	direct current
EAWR	Electricity at Work Regulations
EU	European Union
HRC	hazard/risk category
HV	high voltage
IEEE	Institute of Electrical and Electronics Engineers
IR	infrared
LEM	lumped element model
LV	low voltage
NEC	National Electrical Code
NESC	National Electrical Safety Code
NFPA	National Fire Protection Association
ODE	ordinary differential equation
OSHA	Occupational Safety and Health Administration
PCS	plasma closing switch
PPE	personal protective equipment
PVC	polyvinyl chloride
RC	resistive and capacitive
RLC	resistive, inductive and capacitive
SBSG	self-breakdown spark gap
UK	United Kingdom
USA	United States of America
WGSG	wire-guided spark gap

## Greek symbols

$\alpha$	Townsend's first ionisation coefficient
$\alpha_{\text{eff}}$	effective ionisation coefficient
$\beta$	Townsend's attachment ionisation coefficient
$\gamma$	Townsend's second ionisation coefficient
$\delta Q$	energy added to the system due to heating processes [J]
$\delta U$	change in the internal energy of the system [J]
$\delta W$	energy lost by the system due to mechanical work [J]
$\zeta$	damping constant [rad/s]
$\eta$	Stefan-Boltzmann constant for air, $5.67 \cdot 10^{-8}$ [W/m <sup>2</sup> K <sup>4</sup> ]
$\theta$	angular component of spherical coordinates
$\lambda$	coefficient of bulk viscosity
$\mu$	coefficient of dynamic viscosity
$\mu_0$	magnetic permeability of free space, $4\pi \times 10^{-7}$ [H/m]
$\xi$	plasma channel emissivity factor, $\sim 0.1$
$\Pi$	stress tensor [Pa]
$\rho$	density [kg/m <sup>3</sup> ]
$\rho_0$	non-disturbed gas density, 1.2 [kg/m <sup>3</sup> ]
$\sigma$	electrical conductivity [1/Ω/m]
$\tau$	retarded time [s]
$\tau_C$	Cassie arc parameter for black-box models [s]
$\tau_M$	Mayr arc parameter for black-box models [s]
$\tau_{MC}$	general arc parameter for black-box models [s]
$\tau_r$	rise time [s]
$v$	velocity component parallel to axis y [m/s]
$\varphi$	angular component of spherical coordinates
$\chi$	distance away from the plasma discharge source [m]
$\Omega$	volume [m <sup>3</sup> ]
$\omega$	angular velocity of damped oscillations [rad/s]
$\Omega_{\text{sph}}$	volume in spherical coordinates [m <sup>3</sup> ]

## Roman symbols

$A$	cross sectional area [ $\text{m}^2$ ]
$B$	magnetic flux density [ $\text{Wb}/\text{m}^2$ ]
$BW$	bandwidth [Hz]
$C$	capacitance/capacitor [F]
$c$	speed of sound [m/s]
$C_1$ and $C_2$	avalanche pulse generator capacitors [F]
$C_{\text{arc}}$	capacitive element of arc plasma channel in SBSG and WGSG topologies [F]
$C_{\text{ca}}$	capacitive element of capacitor in SBSG and WGSG topologies [F]
$C_1$	capacitive element of current limiting resistance of voltage-dividing current shunt in SBSG topology [F]
$C_{\text{pcs}}$	capacitive element of plasma closing switch in SBSG topology [F]
$c_{\text{pv}}$	heat capacity ratio/ratio of specific heats, 1.4 for dry air at 20 °C
$C_s$	capacitive element of current sensing resistor of voltage-dividing current shunt in SBSG topology [F]
$d$	inter-electrode gap length [m]
$d_1$ and $d_2$	edge lengths of the rectangular cross section [m]
$dS$	surface element [ $\text{m}^2$ ]
$E_{\text{arc}}$	electric arc energy [J]
$E_{\text{internal}}$	internal energy [J]
$E_{\text{light}}$	light emission [J]
$E_{\text{stored}}$	energy stored in the capacitor [J]
$E_{\text{work}}$	mechanical work [J]
$\mathbf{f}$	force per unit area across a surface element [ $\text{N}/\text{m}^2$ ]
$f$	frequency [Hz]
$\mathbf{F}_m$	magnetic force vector [N]
$\mathbf{g}$	gravitational acceleration vector [ $\text{m}/\text{s}^2$ ]
$G$	arc conductance [S]
$g_r$	gravitational acceleration component in r-axis direction [m/s]
$h_{\text{cyl}}$	length of the arc plasma channel assumed of cylindrical shape [m]
$I$	current [A]

$I_0$	current constant [A]
$I_{af}$	arcing fault current [A]
$I_{arc}$	arc current [A]
$I_{bf}$	bolted fault current [A]
$I_{carc}$	capacitive leakage arc current [A]
$I_{Cs}$	capacitive current of the current shunt of the SBSG topology [A]
$K_p$	Braginskii's resistance coefficient, 0.9
$L$	inductance/inductor [H]
$L_{arc}$	inductive element of arc plasma channel in SBSG and WGSG topologies [H]
$L_b$	inductive element of busbar in SBSG and WGSG topologies [H]
$L_{b1}, L_{b2}$ and $L_{b3}$	inductive elements of copper braids in SBSG and WGSG topologies [H]
$L_{ca}$	inductive element of capacitor in SBSG and WGSG topologies [H]
$L_{cla}$ and $L_{csa}$	inductive elements of capacitor across the limiting and the shunt resistors in SBSG topology [H]
$L_d$	discharging circuit inductance [H]
$L_e$	inductive element of electrode in SBSG and WGSG topologies [H]
$L_l$	inductive element of current limiting resistance of voltage-dividing current shunt in SBSG topology [H]
$\log_e$	constant value obtained from Table 5.3 [ $\mu\text{H}/\text{cm}$ ]
$L_{pcs}$	inductive element of plasma closing switch in SBSG topology [H]
$L_s$	inductive element of current sensing resistor of voltage-dividing current shunt in SBSG topology [H]
$L_{stray}$	stray inductance [H]
$l_w$	length of the wire [m]
$\mathbf{n}$	unit vector normal to the surface
$P$	pressure in the plasma channel [Pa]
$p$	gas pressure [Pa]
$P_0$	atmospheric pressure, 101 [kPa]
$P_{ac}$	acoustic pressure in the radiated acoustic impulse [Pa]
$P_M$	Mayr arc parameter determined empirically [W]
$P_{MC}$	general arc parameter determined empirically [VA]
$q$	electric charge [Q]
$Q_e$	stored energy [J]

$Q_I$	power input [J]
$Q_L$	energy losses [J]
$R$	resistance/resistor [ $\Omega$ ]
$r$	radial component of spherical coordinates
$r$	arc plasma column/electrical discharge radius [m]
$r_0$	initial arc plasma channel radius (is considered 0 $\mu\text{m}$ ) [m]
$r_1$	arc plasma channel radius at the moment of interest – the time that the simulation starts (is considered 1 $\mu\text{m}$ ) [m]
$R_1$ to $R_7$	avalanche pulse generators resistors [ $\Omega$ ]
$R_{\text{arc}}$	arc resistance [ $\Omega$ ]
$r_B$	radial distance from the conductor [m]
$R_b$	resistive element of busbar in SBSG and WGSG topologies [ $\Omega$ ]
$R_{b1}$ , $R_{b2}$ and $R_{b3}$	resistive elements of copper braids in SBSG and WGSG topologies [ $\Omega$ ]
$R_{c1}$ and $R_{c2}$	resistive elements of cables in WGSG topology [ $\Omega$ ]
$R_{ca}$ and $R_{cb}$	resistive elements of capacitor in SBSG and WGSG topologies [ $\Omega$ ]
$R_{ch}$	charging resistor [ $\Omega$ ]
$R_{cla}$ and $R_{clb}$	resistive elements of capacitor across the limiting resistor in the SBSG topology [ $\Omega$ ]
$R_{csa}$ and $R_{csb}$	resistive elements of capacitor across the shunt resistor in the SBSG topology [ $\Omega$ ]
$r_{\text{cyl}}$	radius of the arc plasma channel assumed of cylindrical shape [m]
$R_d$	discharging circuit resistance [ $\Omega$ ]
$R_e$	resistive element of electrode in SBSG and WGSG topologies [ $\Omega$ ]
$R_{\text{eqarc}}$	equivalent constant arc plasma channel resistance [ $\Omega$ ]
$R_l$	resistive element of current limiting resistance of voltage-dividing current shunt in SBSG topology [ $\Omega$ ]
$R_{\text{pcs}}$	resistance of the PCS with the stray resistance of the remaining circuit [ $\Omega$ ]
$R_{\text{res}}$	resistance of the residual circuit loop excluding the arc resistance [ $\Omega$ ]
$R_s$	resistive element of current shunt in SBSG and WGSG topology [ $\Omega$ ]
$R_{\text{sf}}$	discharging resistor [ $\Omega$ ]
$R_{\text{stray}}$	stray resistance [ $\Omega$ ]
$R_{\text{total}}$	total resistance of the loop in WGSG topology [ $\Omega$ ]
$R_{\text{trarc}}(t)$	transient arc plasma channel resistance [ $\Omega$ ]

$R_{\text{var}}$	varying current limiting resistor [ $\Omega$ ]
$R_{\text{var1}}, R_{\text{var2}}$	exemplary values for varying current limiting resistor [ $\Omega$ ]
$r_w$	wire cross section radius [m]
$S$	surface [ $\text{m}^2$ ]
$t$	time [s]
$T$	plasma channel temperature [K]
$T_{\text{arc}}$	ideal plasma closing switch in SBSG and WGSG topology
$t_d$	duration of the electrical discharge [s]
$T_{\text{pcs}}$	ideal plasma closing switch that represents the discharge initiation in WGSG topology
$T_{\text{per}}$	average period [s]
$T_{\text{peri}}$	$i$ -th period [s]
$u$	velocity component parallel to axis $x$ [m/s]
$U_c$	arc parameter for Cassie model [ $\text{V}^2$ ]
$V$	voltage [V]
$\mathbf{v}$	velocity vector [m/s]
$V_0$	voltage constant [V]
$v_0$	initial velocity of the arc plasma channel radius (considered unknown) [m/s]
$V_{\text{arc}}$	arc voltage [V]
$V_{\text{br}}$	breakdown voltage [V]
$V_c$	capacitor voltage [V]
$V_{\text{cc}}$	avalanche pulse generator common collector voltage [V]
$V_d$	discharge voltage [V]
$V_{\text{in}}$	avalanche pulse generator input voltage [V]
$V_L$	inductive voltage measured across a circuit element [V]
$V_{\text{Ls}}(t)$	inductive part of shunt voltage [V]
$V_m$	voltage measured across a circuit element [V]
$V_{\text{out}}$	avalanche pulse generator output voltage [V]
$V_{\text{pcs}}$	voltage across the spark discharge in PCS and across the stray resistance of the remaining circuit [V]
$V_{\text{probe}}$	experimental acquired data from the HV probe [V]
$V_R$	resistive voltage measured across a circuit element [V]
$v_r$	velocity in $r$ -axis direction [m/s]

$v_{r1}$	velocity of the arc plasma channel radius at the moment of interest [m/s]
$V_{Rs}(t)$	resistive part of shunt voltage [V]
$V_s$	voltage across the current shunt [V]
$V_{source}$	DC voltage source [V]
$V_{spark}$	spark discharge voltage of the PCS [V]
$V_{st}$	stabilised voltage of the WGSF [V]
$V_t$	voltage across branch terminals [V]
$V_{trig}$	avalanche pulse generator triggering voltage [V]
$v_\theta$	velocity in $\theta$ -axis direction [m/s]
$v_\varphi$	velocity in $\varphi$ -axis direction [m/s]
$w$	velocity component parallel to axis z [m/s]
$X/R$	electrical system ratio of reactance to resistance
$Z_{af}$	non-linear fault impedance of the arc [ $\Omega$ ]
$Z_{b1}, Z_{b2}$	busbar 1, busbar 2 impedance [ $\Omega$ ]
$Z_{bf}$	fault impedance of the short-circuit [ $\Omega$ ]



# Chapter 1

---

## Introduction

This chapter introduces motivation, aim and objectives of the research. The primary focus and novelty of the thesis, which is the development of a model describing the energy conversion processes during the arc onset, is presented.

### 1.1 Motivation

In recent years, engineering societies have been strongly concerned with achieving a high level of safety in power systems, including minimisation of the risks associated with arcing faults on industrial premises. During the arcing fault, the electrical discharge which takes place can be very explosive with resulting high arc flash and arc blast hazard levels. In other words, the almost instantaneous dissipation of large quantities of electrical energy during the discharge causes thermal, mechanical and chemical emissions which can cause serious injuries and significant levels of equipment damages.

Although the electrical behaviour of the arc has been well understood, there is limited knowledge regarding the energy conversion processes taking place throughout its formation. Moreover, due to the dynamic behaviour of arcs, there are significant uncertainties in predicting the energy dissipation during arcing faults. Thus, selection of the most efficient protection approach poses a substantial challenge for power engineers and practitioners.

Quantification tools for the hazards related to different energy components in the arc are still under development, and further research and validation is required. Only the thermal hazard levels associated with an arc flash and arc blast incident can be addressed in accordance with current standards. A major collaborative research project between the Institute of Electrical and Electronics Engineers (IEEE) and the National Fire Protection Association (NFPA)

started in 2004 to experimentally investigate the heat and thermal energy, blast pressure, sound, and light during an arcing fault, to update the current standards concerning arc flash safety [IEEE1584], [NFPA70E], [LGZ+12], [GLZ+15].

Thus, advancing our knowledge and understanding of electrical arc flash and arc blast hazards through experimentation, modelling and analysis is the main goal of the present research. To achieve this, the research conducted has been consisted of two main parts.

The first part, which is presented in Chapter 3, focuses on understanding better the macroscale manifestation of arc flash and blast phenomena. During the initial stage of the project, significant work was carried out to analyse data provided by GSE Systems on arc flash hazards and mitigation engineering practices in industrial premises. The data was taken from arc flash and mitigation studies performed over decades. The severity of the fully developed phenomenon, which can last for several ms or even more, and the possible impact on the personnel and equipment are studied.

The second part, which is presented in Chapter 4 to Chapter 7, focuses on understanding better the microscale manifestation of arc flash and blast phenomena. During this stage of the project experimental and analytical work was conducted. Studying the initial phase of the arc discharge (ns/ $\mu$ s) provides valuable data on fundamental physical processes taking place. The development of the novel model is described providing significant data for safety considerations. The model allows the energy components associated with thermal, acoustic-kinetic and light emission processes during the initial stage of the arc to be obtained. Finally, an investigation on the potential way of linking arc's initial and fully developed phase is presented in Chapter 7.

## 1.2 Aim and objectives

More specifically, the main objectives associated with the evaluation of the industrial data on arc flash hazards were to:

- Analyse the results of the arc flash hazard assessments for a large range of sites to identify whether the bus voltage level or the facility type are good indicators of the expected arc flash hazard levels (thermal hazard only).

- Analyse the results of the arc flash hazard mitigation studies for a smaller range of sites to confirm significant reductions in the thermal hazard levels.

Thereafter, focusing on the arc flash phenomenon and more specifically examining the arc flash and arc blast during arc initiation provides an insight on the topic from a different point of view. The research has underpinned moves towards a quantitative and scientifically-based evaluation of energy conversion processes during the arc initiation. The main objectives associated with the work of this research on the experimental investigations on the arc onset and the development of the analytical model to predict the associated energy components were to:

- Design and built an experimental topology suitable for accurate acquisition of the electrical characteristics of the arc during its initiation phase.
- Examine two different initiation mechanisms: (1) self-breakdown spark gap (SBSG) discharge and (2) wire-guided spark gap (WGSG) discharge.
- Analyse the experimental waveforms to obtain the electrical voltage and current waveforms of the arc.
- Calculate the equivalent constant resistance of the discharge, following the technique developed by William Greason [Gre99] using the measured current waveforms.
- Calculate the electrical energy deposited in the discharge based on the equivalent constant resistance of the discharge.
- Compare the transient with the constant equivalent resistance of the discharge to verify that the latter represents adequately the relationship between the voltage and the current of the arc discharge.
- Develop an analytical model, based on hydrodynamic theory, which allows the energy components associated with thermal, acoustic-kinetic and light emissions during arc initiation to be obtained. The model has been developed using Braginskii's hydrodynamic energy balance equation [Bra58], which states that the electrical energy deposited in the plasma discharge by Joule heating is converted into the internal energy of the plasma and mechanical work done by the expanding plasma. Light emission has also been considered in the present model. The plasma channel is considered as a blackbody radiator with emissivity factor  $\sim 0.1$  [RCR+96].
- Verification of the present model was performed through comparison with the model developed by Braginskii based on the shock-wave theory. The results obtained for the two ways of the arc initiation were very similar, thus the model developed for the

thesis can readily describe the development of the phenomenon. The assumption made that the disturbance is not a shock-wave does not affect much the expected results.

Finally, aiming to do an initial step towards establishment of the complete and accurate link between arc initiation and its evolution, from an energy point of view, the following research tasks were performed:

- Analysis and evaluation of the suitability of the classical black-box models, Mayr [May43] and Cassie [Cas39] models, for predicting the arc-circuit interaction:
  - At the arc initiation stage with duration of a few  $\mu\text{s}$ ; (to date black-box models have been used for investigation of the arc behaviour within a time range of ms and longer).
  - Within a capacitive circuit; research to date has been focused on AC power system topologies.

### 1.3 Novelty

The thesis presents several elements of novelty, on the experimental side and on the analysis and modelling side. Original contributions of the thesis are:

- The accurate acquisition of electrical characteristics during arc initiation in a busbar to point electrode spark gap topology during two ways of initiation (free discharges (SBSG) and wire-guided discharges (WGSG)).
- The comparison between energy calculations during arc initiation based on transient and equivalent constant arc resistance parameters.
- The analytical model which allows the energy components associated with thermal, acoustic-kinetic and light emissions during arc initiation to be obtained providing useful information for safety considerations.
- The applicability of the hydrodynamic model on both ways of arc initiation: free discharges (SBSG) and wire-guided discharges (WGSG).
- The establishment of the suitability of the black-box models for predicting the arc-circuit interaction within a capacitive circuit during arc initiation (order of  $\mu\text{s}$ ).

- The analysis of industrial data on arc flash hazard studies and mitigation studies to derive conclusions regarding engineering practices related to the arc flash incidents.

Additional elements of novelty are highlighted in the conclusions of each chapter.

## 1.4 Thesis structure

The thesis is divided into 8 chapters:

*Chapter 1* introduces motivation, aim and objectives of the study. The primary focus and novelty of the thesis, which is the development of a model describing the energy conversion processes during the arc onset, is presented.

*Chapter 2* provides a multifaceted literature review. Fundamental concepts of electrical discharges in gases, such as the Townsend's discharge, Paschen's law, streamer discharge and arcs are reviewed. Emphasis is given to the initiation of the arc discharge and impedance analysis. An introduction on hydrodynamic theory is also presented. Additionally, focusing on the arc-electrical circuit interaction, arc models which can describe its behaviour within an electrical circuit are discussed. Furthermore, looking from an industrial point of view, the arc flash incident is described along with risk mitigation methodology.

*Chapter 3* gives a review of arc flash studies, where arc flash severity calculations are performed, for a large range of industrial premises. Results from mitigation studies, performed to reduce arc flash severity where possible, carried out for 26 sites are presented.

*Chapter 4* describes the design of the experimental set-up developed to obtain arc discharge electrical characteristics. The characteristics of the diagnostic equipment used and the preliminary tests conducted to validate the suitability of the set-up for subsequent testing are presented.

*Chapter 5* outlines the results of the tests conducted to investigate the electrical characteristics of the arc discharge. The investigation is focused on the initiation phase of the discharge. The electric energy deposited in the discharge in the form of Joule heating is calculated and subsequently used for further analysis in Chapter 6.

*Chapter 6* presents the analytical model, developed based on hydrodynamic theory, which allows the energy components associated with thermal, acoustic-kinetic and light emission processes during arc initiation to be obtained.

In *Chapter 7*, initial conditions obtained from experimental waveforms were used to investigate the suitability of the black-box model analysis for predicting the arc-circuit interaction within a capacitive circuit during arc initiation.

*Chapter 8* summarises the outcomes of the research and outlines additional avenues of research.

# Chapter 2

---

## Literature review

Chapter 2 introduces relevant background knowledge which underpins the present research project. Initially, fundamental concepts of electrical discharges in gases, such as the Townsend's discharge, Paschen's law, streamer discharge and arcs are reviewed. Emphasis is given to the initiation of the arc discharge and impedance analysis. An introduction on hydrodynamic theory is also presented. An application of this theory to analysing the energy components associated with thermal, acoustic-kinetic and light emission processes during the arc initiation is described. Thereafter, focusing on the arc-electrical circuit interaction, arc models which can describe its behaviour within an electrical circuit are discussed. Furthermore, the macroscale manifestation of a severe electrical discharge in power systems, often called as an arc flash incident, is reported. Fundamental aspects of the risk mitigation methodology are discussed; this methodology can be applied to reduce the arc flash and arc blast severity and probability.

Further detailed information on the important theoretical background used in each chapter is given in Chapter 3 to Chapter 7.

### 2.1 Electrical discharge fundamentals

Electrical discharges have been studied for over 150 years as they are used in different practical areas such as engineering and physics. However, electrical discharges can be extremely dangerous when they appear unexpectedly and evolve uncontrollably, for example in faulty conditions (flashovers and arcing faults) within power systems. The electric field, whether uniform or non-uniform, defines the initiation of the discharge and its subsequent evolution. During the discharge, measurable electrical parameters such as voltage and current and their  $V-I$  characteristic are always under study. Specific focus of this thesis is on the electrical discharges in gases and especially on the initial phase of the arc discharges,

often called spark discharge as well. It is important to understand the arc discharge onset. For this purpose, breakdown mechanism in gases should be described. Subchapters 2.1.1 to 2.1.6 present an analysis of breakdown mechanisms in gases, in order to understand how an insulator becomes a conductor, and important theoretical approaches with a specific focus on the arc discharge and its initiation.

### **2.1.1 Breakdown in gases**

The electrical breakdown mechanisms in gases are described by different models and theoretical approaches as they demonstrate well-defined physical properties which allow mathematical model formulation [Küc17], [KF01], [Coo14]. The main breakdown process in gases is the ionisation which creates charge carriers, positive and negative, that can form electron avalanches which in turn can evolve into plasma streamers [KZ94]. Thus, the insulating properties of the gas are compromised, and a rapid current flow is developed leading to a partial or complete breakdown [Xia16]. Two important theories describing gas discharges are the Townsend and streamer discharge theories, discussed in subchapters 2.1.3 and 2.1.4. Prior to introducing these theories, the electrical properties of a typical low-pressure discharge are discussed in Subchapter 2.1.2, to understand the diverse electrical behaviour of a discharge and demonstrate the extent of the forms the phenomenon can take.

### **2.1.2 Electrical gas discharge properties**

Gas discharge  $V$ - $I$  characteristic can take many forms depending on several factors. These characteristics primarily depend on: (a) the gas type and properties, e.g. pressure, (b) the environmental conditions such as humidity and pressure, (c) the electrical properties of the connected electric circuit, (d) the electric field within which the discharge is created and (e) the electrodes shape and spark gap distance. Figure 2.1 presents a typical direct current (DC) circuit with planar electrodes in a glass tube with a constant power source, uniform electric field, and a varying current limiting resistor. The circuit is schematically divided into two branches, the upper and lower branches i.e. the branch that lies above and below the schematic cut, respectively. This experimental set-up, that is traditionally used in the literature, allows for investigating the discharge electrical properties of a typical low-pressure discharge evolution [Bro55], [Pie10].



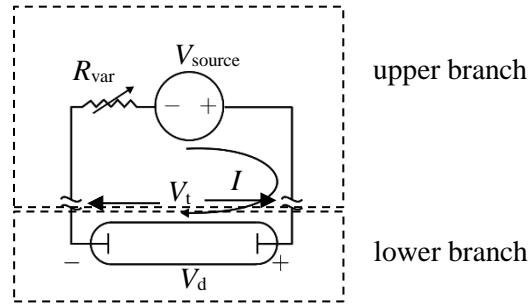


**Figure 2.1** Typical DC circuit with planar electrodes in a glass tube with a constant power source and a varying current limiting resistor.

Equation (2.1) describes the electrical behaviour of the experimental set-up of the upper branch,

$$V_t = V_{\text{source}} - IR_{\text{var}} \quad (2.1)$$

where  $V_t$  is the voltage across the branch terminals,  $I$  is the circuit current,  $V_{\text{source}}$  is the DC source voltage and  $R_{\text{var}}$  is the circuit resistance. This equation represents a family of curves in the  $V_t - I$  space that all cross  $V_t$  axis at  $V_{\text{source}}$  and have a negative slope. Two distinct  $V_t - I$  curves with the same  $V_{\text{source}}$  and different resistance values where  $R_{\text{var}1} > R_{\text{var}2}$  are schematically shown in Figure 2.2 with dashed red lines.

The electrical behaviour of the lower circuit branch (the evolution of the discharge voltage,  $V_d$ , that is equal to the terminal voltage, with varying circuit current) cannot be explicitly described by a function. A schematic representation of the electric behaviour of the lower branch is presented with the solid black curve in Figure 2.2. The non-linear relationship of the voltage drop across the electrodes (voltage of terminals of the lower branch) and discharge current can generally be separated to three regions:

- **Dark discharge** (or Townsend discharge) with currents up to  $\mu\text{A}$  order, before the breakdown in the gas occurs.
- **Glow discharge** with currents up to  $\text{mA}$  order, after the breakdown in the gas occurs.
- **Arc discharge** with currents larger than  $\text{A}$  order, where the voltage drops significantly, and an intense current flow happens.

There is also a **transition region** which bridges the glow with the arc discharge region. These regions are also shown roughly in Figure 2.2.

Further theoretical discussion of the discharge mechanisms is given in subchapters 2.1.3 and 2.1.4.

According to Kirchhoff's voltage law,  $V_d$  and  $V_t$  must be equal. Therefore, points of intersection of the curve described by Equation (2.1) and the non-linear curve of the discharge form the operational points of the circuit. As it can be observed in Figure 2.2, only in the case  $R_{var2}$ , an arc could be created since there is a potential operational point (AD) in the arc discharge region. This demonstrates how the electrical circuit in which the discharge is created plays an important role on the evolution of the discharge. In the case  $R_{var1}$ , the voltage drop across the discharge is not capable of creating an arc, but only able to create a Townsend discharge (TD). Thus, different operating conditions can produce different gas discharge phenomena with different discharge properties.

The experimental and analytical work conducted, which will be presented in Chapter 4 to Chapter 7, aims to analyse the electrical characteristics of the initial stage of the arc. Thus, the electrical characteristics of the discharges created and analysed in the present work lay on the transition region presented in Figure 2.2. The characteristics of the spark discharge or the initial stage of the arc discharge are analysed. Under certain conditions, the arc discharge can develop into a very severe incident where intense energy release might be dangerous for personnel and equipment located in the vicinity of the incident. Results from studies performed for the calculation of the severity of such potential incidents in power systems are presented in Chapter 3.

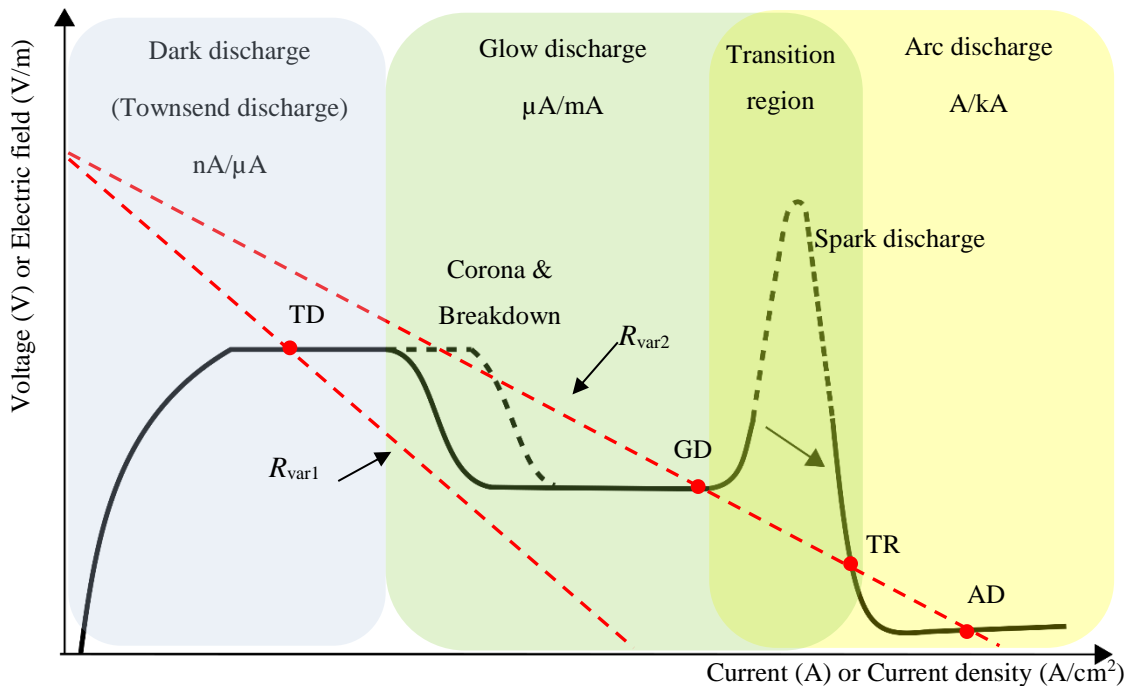


**Figure 2.2** Electrical discharge  $V$ - $I$  plot [Fri08], [SJB+98], [Xia16].

### 2.1.3 Townsend discharge theory and Paschen's law

Townsend discharge theory describes the breakdown of the gaseous medium based on the electronic avalanche concept [Tow14]. The gas electrical conductivity is very low under its normal temperature and pressure which results in considering the gaseous medium as almost excellent insulator (air conductivity at low electric fields  $\sim 10^{-16}$ - $10^{-17}$  A/cm<sup>2</sup>).

Initially, some primary electrons appear in the gaseous medium due to natural ionisation. These primary electrons accelerate in the applied electric field and generate more charged particles (electrons and positive ions) through ionising collisions. Thus, an electron multiplication process starts in the form of electronic avalanches and, eventually, the electrical conductivity of the gas increases compromising the insulating properties of the gas.

Figure 2.3 presents the current and voltage relationship at the beginning of a discharge process (light-blue region, Figure 2.2). Initially, current increases almost proportionally with the voltage increase (light-blue region, Figure 2.3), showing an almost ohmic behaviour. Thereafter, the current remains almost the same with voltage increase. This is known as saturation phase (light-green region, Figure 2.3) where no new electrons, in average, are produced since the available energy is not sufficient to cause excess ionisation compared to recombination mechanism for loss of charged particles. However, as voltage increases, its value is sufficient to cause ionisation and trigger electron avalanche, where the number of electrons generated increases exponentially (light-yellow region, Figure 2.3). According to Townsend, breakdown in the uniform fields (self-sustained discharge) happens when the applied voltage increases to a certain value which exceeds the threshold value, known as breakdown criterion (see Figure 2.3).

To quantitatively explain this current increase, Townsend introduced a quantity known as Townsend's first ionisation coefficient,  $\alpha$  (number of new electrons generated per unit length of the path within an electric field). Townsend also introduced two more coefficients,  $\beta$  and  $\gamma$  (attachment and second ionisation coefficient correspondingly) to quantitatively describe the whole process of gas ionisation. The coefficient  $\beta$  is used to describe a number of electrons per unit length attached to the neutral molecules of the electro-negative gas (with formation of negative ions), thus these electrons are "lost" for the discharge process and the effective ionisation coefficient in this case is  $\alpha_{\text{eff}} = \alpha - \beta$ . The coefficient  $\gamma$  is used to describe the process of secondary electron emission from the cathode, i.e. the number of secondary electrons produced when positive ion strikes the cathode.

Townsend built his theory for gas discharges under uniform field at low pressure and with a small spark gap distance. For different conditions, the evolution of the discharge will change. A modified Townsend criterion might be useful to describe this kind of discharge evolution.

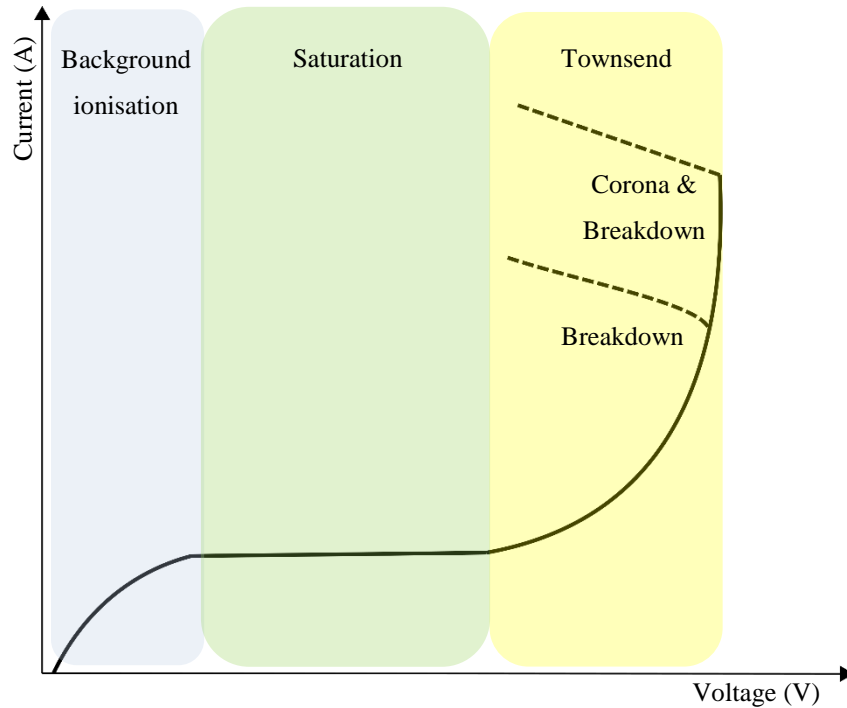


**Figure 2.3** Current and voltage curve showing different regions with different characteristics in a typical discharge in a uniform electric field at low pressure [KZ94].

The Paschen law, which states that the breakdown voltage in uniform fields depends on the product of spark gap length,  $d$ , and pressure of the gas,  $p$ , is presented to complete the theory describing the breakdown mechanisms. When this criterion is fulfilled, the avalanche starts evolving in a self-sustained manner resulting in a loss of the dielectric strength in the gap [Fri08].

The relationship of the breakdown voltage and the  $p \times d$  product is schematically presented in Figure 2.4. For each possible  $p \times d$  product the corresponding breakdown voltage value can be predicted by the graph. Three main regions can be distinguished along the curve: (a) where the Townsend mechanism takes place (b) the transition region and (c) the streamer discharge.

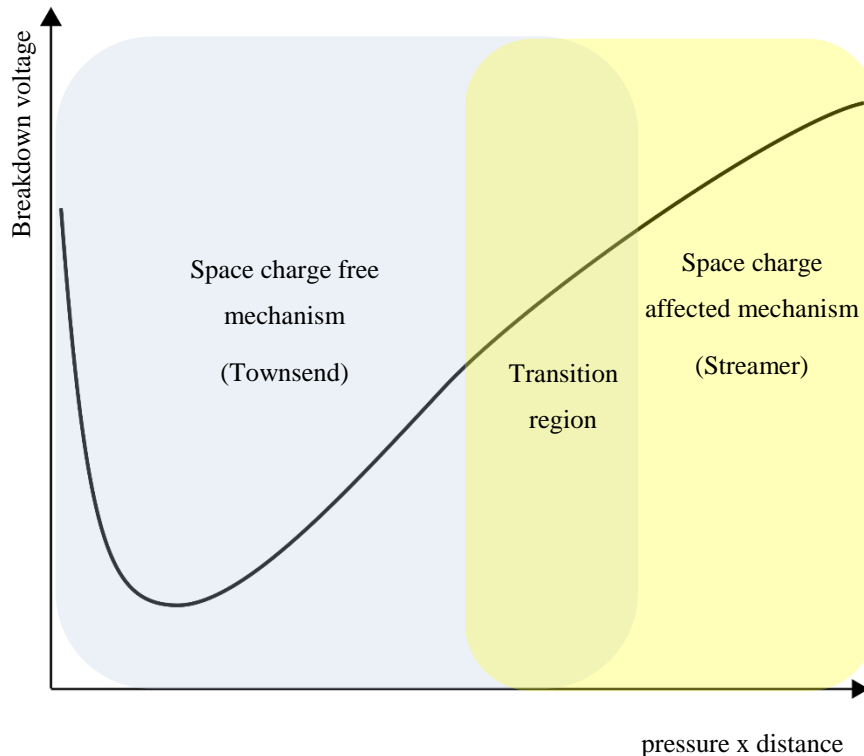


**Figure 2.4** Typical curve showing the relationship of the breakdown voltage and the product of pressure and distance, known as Paschen's curve.

### 2.1.4 Streamer discharge theory

Townsend discharge theory states that successive electronic avalanches are prerequisite for the breakdown [Tow14]. However, some phenomena, such as the rapid occurrence of the breakdown under an applied voltage, sometimes faster than the time an electron needs to travel the gap, are difficult to explain. Thus, Reather, Loeb and Meek proposed the streamer theory which considers the effect of space charge to explain the discharge development and complements the Townsend theory to describe the breakdown [Mee40], [LM40].

The streamer discharge theory is based on the phenomena that occur due to the significant electric field distortion caused by the space charge at the head of the avalanche, Figure 2.5. The charged particles energy causing the ionisation can increase due to this distortion. When these charged particles of the avalanche head reach a critical concentration (for uniform electric field is  $\sim 10^8$ ) or, in other words, the space charge field strength reaches a certain value, the avalanche transforms into a streamer. The streamer is a pathway consisting of plasma that is the fourth state of matter. Plasma is macroscopically electrically neutral, yet it is electrically highly conductive due to the plasma composition i.e. combination of co-

existing unbounded positive and negative particles. In the streamer case in gaseous media, the plasma is an ionised gas channel that bridges the electrodes, and breakdown occurs.

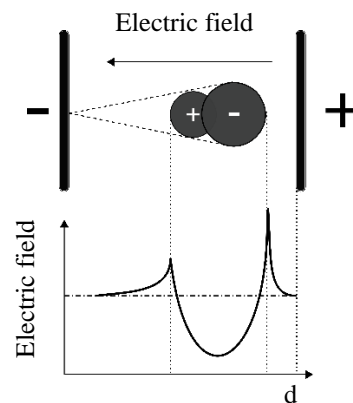


**Figure 2.5** Electric field distortion across an avalanche under uniform field conditions across a spark gap with  $d$  length.

The streamer plasma, which is formed during the initiation of the discharge, is in non-thermal-equilibrium which means that the electrons have much higher temperature than the heavy particles. This property of the plasma changes during the discharge evolution (given that the necessary energy is supplied) and becomes a thermal equilibrium plasma where electrons and heavy particles are considered to have the same temperature.

### 2.1.5 Spark discharge and arc discharge

Following the gas breakdown, the initial breakdown which has the form of a spark discharge may transit to an arc discharge.

The spark discharge or spark breakdown is a short living transient arc plasma discharge where current flows and the insulating properties of the medium are compromised. A shock-wave is created in the surrounding medium during the formation of the spark. The shock-wave is a pressure wave which is considered that it does not move or transfer gases or mass during the phenomenon. However, it is a significant part of the energy release during this phenomenon.

Given that the power supply continues to provide current to the discharge, the spark can rapidly evolve into an arc which is a continuous arc plasma discharge. The continuous discharge current results in a further increase in the plasma temperature [Küc17], [KZ94].

Thus, both arc and spark discharges describe different manifestations of the same phenomenon. The main differences are discharge time duration and energy, resulting in different levels of impact in the surrounding environment.

In the literature, terms of “arc” and “spark” are often used interchangeably [Kim09]. There can be cases that an arc is interrupted, and this can be done electrically or mechanically. Thus, sparks and interrupted arcs are generally considered the same [IUPAC14].

In the remaining subchapter, additional information regarding arc discharge is given.

The arc discharge is a conductive plasma with low resistance, high temperature and high energy transport capability. It should be noted that not all conductive plasmas show these characteristics. For example, the glow discharge is a high resistance plasma with low temperature and low energy transport capability.

During the arc discharge, several physical processes take place; electromagnetic and fluid dynamic/thermodynamic as well as chemical that are not always possible to be accurately defined [Ede61], [SJB+98], [PS16]. In the power industry, the processes during the arc discharge are often collectively referred as arc flash and arc blast incident. In Subchapter 2.4.2, arc flash and arc blast hazards during a severe arcing incident are described in more detail.

The arc shows a negative  $V$ - $I$  characteristic and the arc plasma column is developed, Figure 2.6. During the initial phase of the phenomenon, the voltage drop across the arc is large, resulting in a small current increase until a certain value. Thereafter, the  $V$ - $I$  characteristic does not have a negative slope [AGS+10], [Bro55]. When the arc plasma resistance reaches its minimum value, the voltage increases with current.

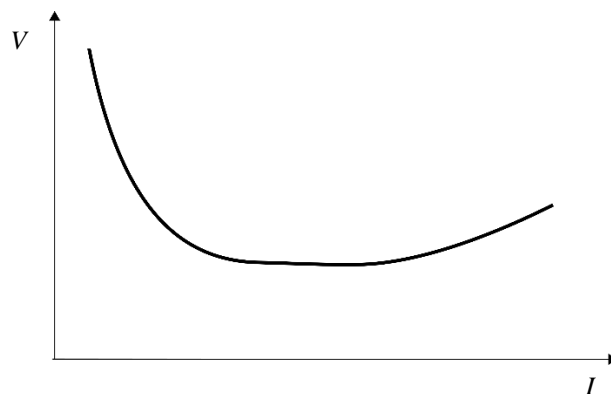


**Figure 2.6** The arc  $V$ - $I$  characteristic.

A simplified schematic presentation of the arc's three regions: the anode, the cathode and the plasma column can be seen in Figure 2.7. The anode and cathode are plasma and electrode transition regions [AGS+10]. The arc discharge's plasma column is the high energy plasma area. The associated voltage drops of the anode and cathode are of significant importance during the fully developed stage of the arc. However, in the present work, since the focus is on the initial stage of the arc, no voltage drops at the anode and the cathode are taken into consideration.

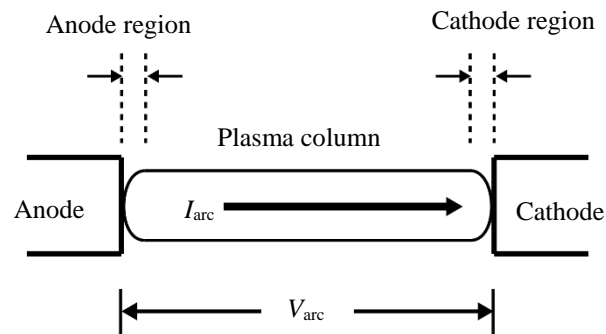


**Figure 2.7** Arc regions: arc plasma column, anode and cathode region.

Variables involved in the arc plasma column development (length, geometry) are [AGS+10], [Bro55], [Jon88]:

- nature and state of the gas medium (gas temperature and pressure)
- electrode material (vaporisation and shrapnel)
- density and velocity of charge carriers (rates of current change)
- electric field strength (electromagnetic forces)
- energy losses due to thermal radiation
- length of the arc (spark gap length)
- arc extinction and re-striking
- thermal convection

### 2.1.6 Arc plasma transient impedance

The time dependent arc impedance has resistive, inductive and capacitive parts [EDK89], [AKK+88], [PVG+92]. The most dominant part of the impedance is the resistive part. In the literature, the plasma channel resistance is defined as a function of the current. The diameter of the arc channel is also a function of the current and arc length, temperature and pressure,



and it is used to calculate the arc plasma resistance. The plasma channel diameter, initially, has a very small cross-section which increases with the energy delivered in the discharge.

The arc plasma transient resistance function proposed in the literature, either links the arc resistance,  $R_{\text{arc}}$ , with the inverse arc current integral,  $(\int I_{\text{arc}} dt)^{-1}$  or the inverse arc current to the  $n^{\text{th}}$  power,  $I_{\text{arc}}^{-n}$ . Both approaches are suitable for modelling the plasma resistance in the first quarter of the cycle of arc current [Toe06], [RW44], [BVL75], [PPP74], [DMS+68], [KKB85], [Vla72], [GR71].

Braginskii [Bra58] proposed an equation describing the plasma channel radius evolution based on the energy balance equation and the hydrodynamics principles. Comparison with the experimental results obtained by Maas on plasma resistance validated Braginskii's model [Maa85]. Braginskii's methodology was followed in the present thesis in Chapter 6. The detailed description of this methodology is presented in Chapter 6.

The transient behaviour of the arc plasma resistance is of great importance. On the other hand, there were approaches in the literature where this characteristic of the discharge was estimated roughly with an equivalent constant resistance. William Greason [Gre97], [Gre99] developed a technique to measure the equivalent constant resistance of a spark discharge between two spherical electrodes using the measured discharge currents for underdamped and forced overdamped cases. The discharge circuit is considered as a series resistive, inductive and capacitive (RLC) system. Based on this analysis, in Chapter 5, analysis of the obtained experimental results has been conducted. The detailed description of the methodology is presented in Chapter 5.

## 2.2 Thermodynamics and fluid dynamics principles

An alternative description of the arc phenomenon during its initiation phase is achieved by assuming that the arc plasma channel behaves like a fluid which interacts with the atmospheric air, and it is treated as a continuum. Flow of plasma is, therefore, described by three fundamental macroscopic conservation laws of:

- energy
- mass
- momentum

More detailed description of the conservation law equations is presented in Chapter 6.

These principles are used for description of arc initiation solely. For established arcs, additional phenomena take place and, therefore, more conservation laws must be considered.

This thermodynamic approach was used for the development of a novel arc energy partition model presented in Chapter 6. The model was developed according to Braginskii's hydrodynamic energy balance equation [Bra58], which states that the electrical energy deposited in the plasma discharge by Joule heating is converted into the internal energy of the plasma and mechanical work done by the expanding plasma.

### 2.2.1 Energy balance equation

The energy conservation equation, in the context of thermodynamics, states that the energy is conserved in a closed thermodynamic system and only transforms from one form to another. The conservation of mass equation (equation of continuity) states that the mass is conserved inside a closed volume. Thus, the rate of decrease of mass in the volume within the fluid equals the mass flux out of this volume. The conservation of momentum equation states that the rate of change of momentum should be equal to the total force exerted on the fluid (see Subchapter 6.1)

Combining the three conservation equations of energy, mass and momentum, along with additional assumptions used in the present study (see Subchapter 6.2) results in the energy balance equation, Equation (6.11), schematically presented in Figure 2.8. This equation links the pressure in the plasma channel and its volume with the electrical energy delivered to the plasma. Light emission has also been considered in the present model.

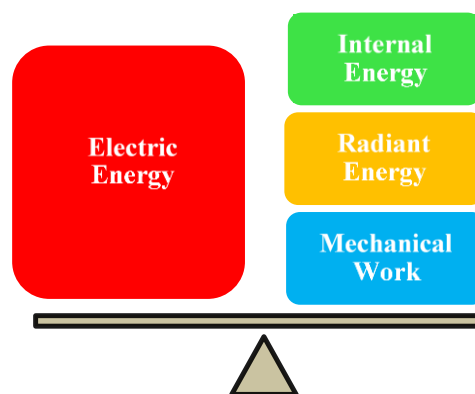


**Figure 2.8** Energy balance: the basis of arc energy partition model given in Equation (6.11).

## 2.3 Arc models

The majority of models that describe the arc phenomenon once an arc has been established are generally addressed as arc models. The arc plasma is considered to be a fluid and is affected by several coupled processes of electromagnetic, chemical and fluid-dynamic nature. Furthermore, in engineering applications, the complexity of the plasma phenomenon is enriched by the variety of boundary conditions resulting from the range of circuit elements.

The theoretical behaviour of arc plasma may be described by the Maxwell equations and the fluid conservation equations.

An arc can be completely described by the following equations [Jon88]:

- the coupling between voltage and electric field (Maxwell equations)
- the Poisson equation (which provides the electric field distribution in the presence of space charge)
- the charge carrier balance
- the electron current density
- the ion current density
- the energy balance in the spark discharge
- the Saha equation (which establishes the link between plasma, temperature and conductivity)

A wide range of arc models have been developed using different approaches tailored for specific applications. In general, these models can be roughly divided in two wide categories: physical and mathematical black-box models.

The mathematical black-box model is developed based on the energy balance equation. The arc conductance can be expressed as a function of the stored energy which is the excess energy resulting from the deduction of the energy losses from the electrical power input [Bro55]. Cassie and Mayr developed their specific models applying additional assumptions.

More detailed description of the physical and mathematical models is given in Chapter 7 that focuses on Mayr's and Cassie's black-box models [May43], [Cas39].

## 2.4 Arc flash and arc blast incident

Significant research on dielectric breakdown, plasma and arcs have been conducted over the years contributing substantial knowledge and further understanding of their physics and their behaviour. However, due to the dynamic behaviour of arcs, there are still significant uncertainties in predicting the energy dissipation during arcing faults. Moreover, there are some unanswered questions, for example, (i) how does the arc electrical energy convert into arc flash and arc blast energies? (ii) which factors control this conversion? and others. Additionally, quantification tools for the hazards related to the different energy components in the arc are still under development, and further research and validations are required. Therefore, selection of the most efficient protection approach(es) poses a substantial challenge for power engineers and practitioners.

Thus, arc-related topics which have not been adequately investigated to date are the science of the arc flash and the arc blast energy which are becoming of increasing importance in the power industry.

More specifically, Subchapter 2.4.1 describes the behaviour of the arcing and bolted faults in the power systems, highlighting their main differences. Subchapter 2.4.2 presents the arc flash and arc blast hazards during a severe arcing incident. Additionally, the main factors that govern arc flash and arc blast severity and common causes and consequences are presented in subchapters 2.4.2.1 to 2.4.2.2.

### 2.4.1 Arcing and bolted faults

The electrical faults occurring in power systems can be generally categorised as bolted (short-circuit) or arcing faults. The main differences between these faults are the fault impedance, the fault current and the energy dissipation.

#### 2.4.1.1 Bolted fault

In the case of a bolted fault between busbar 1 with impedance,  $Z_{b1}$ , and busbar 2 with impedance,  $Z_{b2}$ , Figure 2.9(a), the low fault impedance of the short-circuit,  $Z_{bf}$ , results in a relatively high fault current,  $I_{bf}$ . Bolted faults occur when a solid conductive path is built within the electrical system allowing the relatively high fault current to flow. An example of a bolted fault is shown in Figure 2.9(a) which depicts an accidental short-circuit between two

busbars by a metallic tool resulting in a low impedance fault with high current. Given that an adequate power system protection scheme is implemented, the fault will probably be detected rapidly and will be cleared quickly without allowing large quantities of energy to be dissipated. It should be noted though that, under certain conditions, the bolted fault can potentially evolve to a severe arcing fault. For example, if the short-circuit fault has a duration which results in melting the solid conductive path and the power system is capable of supplying energy in the fault, the short-circuit fault will escalate to an arcing fault.

#### 2.4.1.2 Arcing fault

An arcing fault is a high power electrical discharge between two or more electrical conductors. In the case of an arcing fault, Figure 2.9(b), the high time-varying non-linear fault impedance of the arc which is considered to be a mainly resistive impedance,  $Z_{af}$ , resulting in a relatively low fault current,  $I_{af}$ , [Lee82]. Arcing faults occur when a conductive path is built through the gas, usually air (which was previously considered as insulating material), within the electrical system, allowing a relatively low fault current to flow. The power system protection scheme might not be able to sense this kind of fault rapidly due to its relatively low current resulting in the dissipation of large amounts of energy. The arcing faults can potentially be very violent due to the almost instantaneous energy dissipation. The main adverse consequences of the arcing faults include power supply interruption, fires, arc flashes and arc blasts with all their dangerous effects.

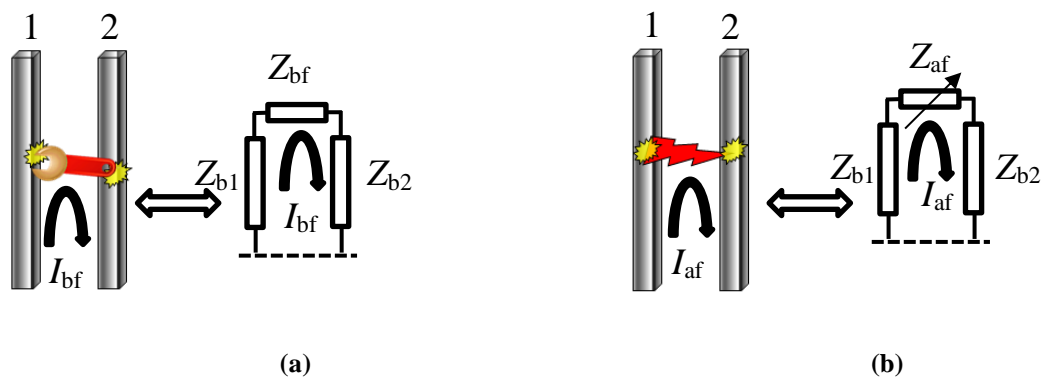


**Figure 2.9** (a) Bolted fault where the current,  $I_{bf}$ , is high due to the solid conductive path (for example a metallic tool) and the impedance,  $Z_{bf}$ , relatively low (b) arcing fault where the current,  $I_{af}$ , is low due to the relatively high non-linear impedance of the arc,  $Z_{af}$ .

## 2.4.2 Arc flash and arc blast hazards

### 2.4.2.1 Description of the phenomenon

Arc flash and arc blast incidents can potentially occur at a wide range of installations, often causing severe damages to the electrical system and injuries or death to personnel in close vicinity of the incident. An arcing fault usually occurs between phase busbars or between phase and neutral or ground, within an enclosure, such as switchgear, or in the open air. Arcs can be formed in DC and AC electrical power systems and can appear as series or parallel arcing faults. The main difference between the series and parallel arcs is that the series arcs always have lower current magnitudes than parallel arcs [AGS+10]. When the electrodes of the arc are located freely in air, the arc formed in this case is called non-axisymmetric or a free burning arc. In contrast, an axisymmetric or stabilised arc is created when the arc is formed at electrodes located in a confined location [AGS+10].

The duration and current magnitude of an arcing fault can vary widely. Under certain conditions that sustain the arc, arcing faults develop into dangerous arc flash and arc blast incidents. Clearing time of the upstream protective device defines the arcing duration. An arcing fault impedance (higher than short-circuit impedance) controls the arcing current, as described in Subchapter 2.4.1.2. Generally, power systems with voltage magnitudes lower than 120 V AC or 50 V DC are considered as systems which cannot sustain an arc. It is well known that, for typical arcing faults in power systems, the current magnitudes are expected to be of the order of a few kA's.

When an arc flash and arc blast occurs, significant amounts of energy can be dissipated in a very short time in the form of thermal and mechanical energy and chemical discharges. During a severe incident, the energy release causes ionisation and vaporisation of the conductive metal and insulating materials or air (creating a high density and high temperature, conductive plasma continuing to vaporise and ionise materials) and heating of the ambient air that creates a rapid volumetric expansion of arc plasma and, consequently, an explosion [Lee82], [Lee87]. Unlike spark discharge, the shock-wave created during the arc flash and arc blast in the surrounding medium is accompanied by mass transport. This is a result of the presence of material vapour, molten droplets and shrapnel. This mass transport is also responsible for thermal convection contributing to the stochastic and dynamic nature of the phenomenon [AGS+10].

In the power industry, the term “arc flash” is generally used to describe the thermal energy dissipated during the phenomenon. This energy of the arc is considered to be the 30% -40% of the total available energy.

The term “arc blast” is generally used to describe additional hazards beyond the thermal hazard of arc flash. Primarily, arc blast refers to the acoustic shock-wave accompanied by shrapnel created by high electrical energy density.

To be more specific, an arc flash and arc blast incident, as indicated in Figure 2.10 [NFPA70E], comprises:

- Intense heat, intense light (IR and UV radiation) and high temperature (>3,000°C sometimes up to 20,000°C)
- Metal (e.g copper) or insulating material vapour and hot air expansion
- Pressure and sound waves (e.g. 203 kPa at 0.6 m)
- Shrapnel/debris (e.g. ~1000 km/h), molten material
- Flames, smoke and toxic gases

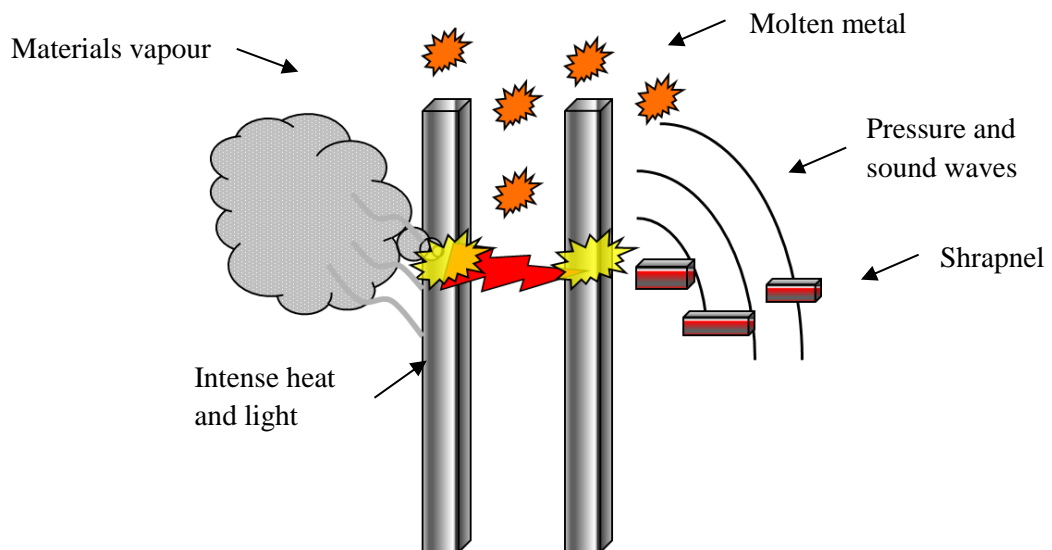


**Figure 2.10** Arc flash and arc blast according to NFPA [NFPA70E].

Due to aforementioned hazards, consequences to human and business can be severe. Personnel exposed to arc flash and arc blast can suffer [Nei08], [AGS+10], [SS06], [SW11]:

- severe thermal burn
- lung damage
- vision loss
- eardrum ruptures

- and even death

During a severe arc flash and arc blast incident, an important arc characteristic can be observed; its ability to move under certain conditions. An arc during the fault can possibly move due to the magnetic forces created by the high levels of current. For instance, Figure 2.11 presents this potential motion of an arc between two busbars. Equation (2.2) gives the magnitude of the Lorentz forces on a charge carrier in the arc developed during the fault and the direction given by the right-hand rule [Lan08]. The magnitude of the magnetic field is given by Equation (2.3).

$$\vec{F}_m = q\vec{v} \times \vec{B} \quad (2.2)$$

where:

$\vec{F}_m$  : magnetic force vector [N]

$q$  : electric charge [Q]

$\vec{v}$  : velocity vector [m/s]

$\vec{B}$  : magnetic flux density [Wb/m<sup>2</sup>]

$$\vec{B} = \mu_0 I / 2\pi r_B \quad (2.3)$$

where:

$\mu_0$  : magnetic permeability of free space ( $4\pi \times 10^{-7}$ ) [H/m]

$I$  : arc current [A]

$r_B$  : distance from the conductor [m]

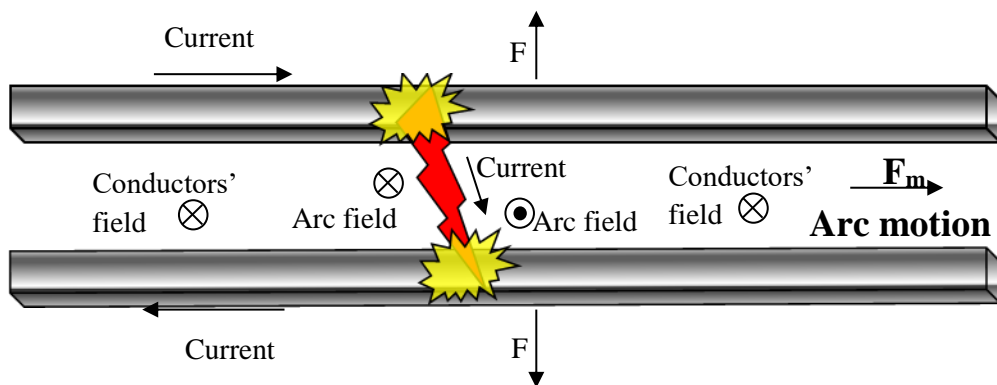


**Figure 2.11** Arc motion due to magnetic force created by the current.



### 2.4.2.2 Common causes of arc flash and arc blast incidents

There are several known common causes of arc flash events that can generally be separated in causes due to [Das12]:

- **human error:** accidental touch or accidental touching/dropping of tools, nuts-bolts, metal parts, dropping or misplacement of the tools and other parts, improper installation practices, wrong rated tools used
- **mechanical failure:** voids in insulation and insulations breakdown, failure of insulating materials, partial discharges, breaker failures in contacts, springs, stabs etc, loose connections and bolts, warping due to shifts in floor, aging connectors etc
- **intrusion:** varmint or insect entrance, snakes, mice, rats, raccoons, bees, snapping of leads at connections due to human, rodents or birds
- **environmental issues:** dust, contamination, moisture, impurities, corrosion
- **sparks:** produced during racking of breakers, replacement of fuses, breakers/ fuses closing into faulted lines

## 2.5 Risk management and mitigation methods

Since 1982, when the electric arc flash and arc blast were introduced as another electricity-related hazard by Ralph Lee [Lee82], [Lee87], research on the topic has been conducted. In recent years, engineering societies have been strongly concerned with achieving a high level of safety in power systems, including minimisation of the risks associated with arcing faults on industrial premises.

There are significant research efforts concentrated on how to improve control and management of the risk of arc flash and arc blast incidents and how to mitigate the related hazards [Nei06]. A major collaborative research project between the IEEE and the NFPA started in 2004, to investigate experimentally the heat and thermal energy, blast pressure, sound and light during an arcing fault, to update the current standards concerning arc flash safety [IEEE1584], [NFPA70E], [LGZ+12], [GLZ+15]. In addition, research is focused on the energy transfer mechanisms within an arcing fault and the electrical energy conversion processes [SS07], [GG15].

### 2.5.1 Risk Management

Risk management is an iterative and continuous process that aims to reduce the risk and incorporate best practice [Rob12], [ISO31000]. Risk is defined as a combination of possibility and severity, and gives the likelihood that a hazard will be harmful. Figure 2.12 shows the risk management procedure according to risk management principles and guidelines presented in [ISO31000].

Risk assessment involves risk identification, risk analysis and risk evaluation of the arc flash. Risk analysis is performed to estimate the likelihood of an arc flash incident and the severity of arc flash hazards. Risk can be high even in cases where only likelihood is high or in cases where only severity is high. Likelihood is affected by two main factors: the number of interactions with energized electrical equipment and the condition of electrical equipment. Severity is the degree of harm that results from the exposure. Risk evaluation should be conducted to determine if the risk is acceptable. If not, risk treatment, risk control and mitigation procedures are required to reduce arc flash risk and hazard. Selection of personal protective equipment (PPE), placement of warning labels indicating the hazards and training of operators are also essential parts of risk management.

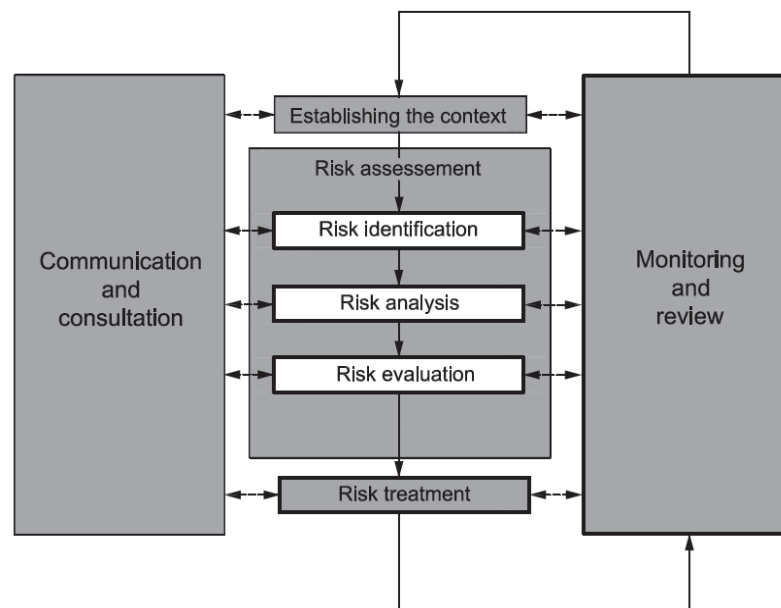


**Figure 2.12** Risk management process according to [ISO31000].

## 2.5.2 Mitigation Methods

Since fault duration and current magnitude determine the intensity and severity of the phenomenon, conventional control measures aim to sense the arcing fault and disconnect the supply as quickly as possible before it develops into the dangerous arc flash condition. Within the risk assessment, arc flash hazard analysis is crucial in order to evaluate the arc flash risk and decide which mitigation techniques are appropriate to control it. In some cases, the hazard can be reduced without significant investment in equipment. In cases where significant arc flash hazard reduction is difficult to achieve, implementation of innovative mitigation techniques provides an alternative way [DNA+13], [SW11].

However, it should be noted that only the thermal hazard levels can be addressed in accordance with the current standards. NFPA 70E and manufacturers are beginning to address some of the arc blast hazards, e.g., hearing protection and impact resistant face shields [GLZ+15].

The philosophy and methodology of arc flash hazards and risk mitigation is discussed further in Chapter 3. The importance of mitigation measures in the framework of a complete and ongoing arc flash risk management is discussed. Furthermore, an overview of conventional and innovative mitigation methods is presented.

## 2.6 Prevention

When trying to predict and prevent arcing faults, it is important to investigate the conditions that cause them. Knowledge of the conditions helps to anticipate and eliminate the occurrence of the incident [LRB+11], [HHJ+12]. One relevant technique is to monitor insulation integrity and electrical system condition. There are several maintenance tools that can be used to provide us with the necessary information of a potential failure in the electrical system. However, prediction and prevention techniques are quite difficult to implement, and their outcomes cannot always be reliable.

Partial discharges detection is used for continuous online monitoring for transformers, cables, motors, generators and switchgear using permanently installed sensors. Infrared (IR) thermography can indicate a location when an overheated electrical connection or component might exist. In the cases where IR windows or ports are pre-located in the

electrical system, the procedure can be conducted while keeping the panels of the switchgear closed, and this reduces exposure to energised parts of the switchgear.

Currently there is a strong tendency to secure safety during design phase. For instance, barriers are located into the switchgear. Every effort should be made during the design phase to achieve the highest possible level of prevention of the hazard.

# Chapter 3

---

## **Arc flash studies review**

Data [GSES15] derived from arc flash studies for a large range of sites, from power generation plants to office facilities, are reported in Chapter 3. Analysis of arc incident energies pre- and post-mitigation shows that risk control measures can lead to significant reductions in thermal hazard levels. Although there are several cost-effective risk mitigation techniques which can be used to minimise arc flash severity [Das12], [DSB09], it is not always possible to reduce this severity down to the desired levels. This shortfall, along with the fact that only the thermal hazard levels can be addressed in accordance with the current standards, instigates further research on the topic. Quantifying other hazardous components of the arc and better understanding of its initiation and behaviour define the main objective of this research.

Subchapter 3.1 briefly introduces codes and standards regarding electrical safety and risks during an arc flash incident (see Chapter 2.4 for information on arc flash and arc blast incidents). A widely used method for the calculation of arc flash severity in power systems in accordance with the IEEE Standard 1584 – Guide for Performing Arc-Flash Hazard Calculations [IEEE1584] allied to NFPA 70E Standard – Standard for Electrical Safety in the Workplace [NFPA70E] is presented in Subchapter 3.1. The importance of mitigating the hazard levels and reducing the likelihood of the arc flash occurrence in the framework of a complete and ongoing arc flash risk management is discussed in Subchapter 3.3. Results from arc flash studies, where arc flash severity calculations are performed, conducted for a large range of industrial sites are reported in Subchapter 3.4. Results from mitigation studies, performed to reduce arc flash severity where possible, are reported in Subchapter 3.5. Finally, conclusions and discussion are given in Subchapter 3.6.

## **3.1 Electrical safety and arc flash codes and standards**

### **3.1.1 IEEE Std. 1584 and NFPA 70E – USA**

To date, the arc flash electrical safety has not been fully addressed in the official documents which are publicly available. However, guidance in assessing and improving the arc flash safety is documented in the IEEE Std. 1584 [IEEE1584] and NFPA 70E [NFPA70E], which are widely accepted as the definitive current global standards in this field. Additional documents which provide safeguarding of personnel and equipment from electricity hazards are the (i) Occupational Safety and Health Administration (OSHA) CFR Title 29, (ii) National Electrical Safety Code (NESC) (or also known as American National Standards Institute (ANSI) C2), and (iii) NFPA 70: National Electrical Code (NEC) [Phi11].

An ongoing major collaborative research project between the IEEE and the NFPA started in 2004 is focused into quantification of several thermal and non-thermal hazards of the arc flash [LGZ+12], [GLZ+15]. Through further extensive research and testing on the arc flash phenomena, the project collaborators aim to investigate the heat and thermal energy, blast pressure, sound, light and other hazards during an arcing fault, to update the current standards concerning arc flash safety.

### **3.1.2 UK and Europe**

Since there is a lack of European standards for assessing arc flash severity, the USA standard, IEEE 1584 [IEEE1584], is widely used in the UK and Europe. Additionally, there are several national safety regulations that should be followed. For reference, in the UK, Regulation 14 of the Electricity at Work Regulations (EAWR) [EAWR89], [HSE15] defines the conditions to be met when working on energised systems and requires risk assessments to be performed. Furthermore, the European legislation through Directive 89/391 – European Union (EU) Workplace Health and Safety Directive [CD89/391EEC] states that appropriate risk assessments should be performed. The European Arc Guide [DuPont] provides a step by step approach to determine and evaluate the risks associated with the arc flash and establish electrical safety practices.

### **3.1.3 Complying with the safety requirements**

Updates on the safety requirements are performed regularly as a response to new information on the arc flash hazards and mitigation methods and data on electrical incidents at industrial plants and facilities. It is essential for the industry to keep up to date and to comply with the requirements defined in the safety standards to achieve the highest level of safeguarding of personnel and assets [PF12]. Compliance with codes, standards and regulations helps the industry to address electrical safety issues and to meet all legal requirements. There are ongoing efforts to improve safety codes, standards and regulations referring to arc flash in a way that they will include state of the art methods to provide better electrical safety and electrical performance [FJ13].

A method, widely and primarily used in the power industry for assessing the arc flash hazard severity is presented and discussed in Subchapter 3.2. The associated arc incident energy levels are determined based on calculations in accordance with IEEE Std 1584 allied to NFPA 70E Standard. Although, there are alternative ways to estimate the arc flash hazard severity, i.e. using directly the hazard/risk tables given in NFPA 70E Standard (see Appendix A), a comprehensive arc flash hazard calculation study is considered to provide the most reliable results for the electrical system under consideration.

Regardless of methods used to define the severity of the arc flash in an electrical power system, quantifying the hazards is the first and most important step of the procedure towards achieving arc flash safety. Depending on the predicted arc flash severity, mitigation methods might need to be implemented to reduce the levels or the impact of the hazards. For example, retrofitting critical components of the system might be suggested to reduce the hazard levels and/or the use of personal protective equipment (PPE) may be instructed to personnel to reduce the risk. These recommendations are the part of an iterative and continuous risk management process which aims to reduce the risk and incorporate best practice, as performed in power systems analysis industry [Rob12], [ISO31000].

## **3.2 Methodology to assess arc flash severity**

The scope of the study is to determine the available arc energy levels at all locations/buses within the power system under consideration and to provide detailed information about the potential hazards and required personal protective equipment. Although, this project does not

consider all possible arc flash hazards in details, through this study, the thermal energy hazard is analysed.

Two main factors, along with other factors such as equipment type and gap distance, should be defined for the arc incident energy calculation:

- The prospective fault current, bolted and arcing, at all switchboards/distribution boards/panels.
- The operating time of the upstream protective device, including circuit breaker mechanical opening time if applicable, at all switchboards/distribution boards/panels.

According to the IEEE Std. 1584[IEEE1584], for the arc energy assessment, it is recommended to consider two scenarios for the system infeed fault level (a) 100% and (b) 85% which cause variation on the arcing current and duration (protective device time). A lower current value might result in the protective device to operate slower than in the case of a higher current value yielding higher arc incident energy levels. The worst-case results between these two cases should be considered for safety recommendations.

The calculation method depends also on the voltage level. The IEEE Std. 1584 provides detailed guidance on performing the arc flash hazard calculations based on the voltage levels:

1. For systems operating from 208 V to 15 kV (three-phase), empirically derived formulae for arc flash calculations are provided.
2. For systems operating at voltages greater than 15 kV (three-phase and single-phase), physics-based models are provided, which involve the analysis of heat flow from the arcing element in open air [Lee82].

The contributing factors to the arc flash intensity and the severity are presented in Subchapter 3.2.1. Subchapter 3.2.2. details the basic steps to complete the calculation study. The four essential outcomes of the study are presented in Subchapter 3.2.3.

### **3.2.1 Contributing factors to the arc flash intensity and severity**

Factors that affect the intensity and severity of the phenomenon are:

- The electrical arc current
- The electrical system voltage and frequency
- The electrical arc duration



- The conductors gap into the electrical system
- Enclosed in a box or open-air arc
- The working distance
- X/R electrical system ratio
- Electrical installation type, layout, electrodes configuration, conductors' tips termination
- Earthing/grounding system
- Other factors such as
  - Gas nature/state
  - Conductors material
  - Equipment age/condition
  - Environmental issues

Analysis of the impact of several of the aforementioned factors considering any possible important interactions between the variables has been allowed during the testing conducted by the IEEE. However, not all the factors have been taken into account in the developed equations. For example, the nature of insulating gas or the environmental issues are factors which are extremely difficult to be addressed.

Based on experimental tests, the importance of certain parameters has been defined, and the arc current has been identified as the most important parameter [IEEE1584], [Das12]. The arc current depends primarily on the available fault current. The bus gap, system voltage and grounding type are factors with smaller impact on the incident energy. System X/R ratio and electrode material has very little effect on the arc current.

The IEEE Std. 1584 considers three-phase arcs which produce the greatest possible arc-flash hazard in the AC equipment. Arcs have been created within AC power systems energised with 50-60 Hz. Thus, it is not possible to estimate other types of faults or DC faults using the IEEE 1584 equations.

### **3.2.2 Basic steps to complete an arc flash study**

The electrical power system should be accurately modelled and analysed under its normal operational condition at 100% and 85% of the system infeed fault level. Additionally, different scenarios of altered operational conditions should be evaluated to establish the maximum prospective arc incident energy levels.

The basic steps for conducting the arc flash hazard calculation study are listed in [IEEE1584] and they are:

- Electrical system and installation data collection
- Scenario modelling (electrical system operation modes determination)
- Bolted fault currents determination (acquired from short circuit study)
- Arc fault currents determination
- Protective device characteristics and arc duration determination (acquired from coordination study)
- Electrical system voltages and classes of equipment identification
- Working distances identification
- Incident energy calculation for all equipment
- Determining the PPE requirements
- Arc flash protection boundary calculation for all equipment
- Arc flash warning labels production
- Initial mitigation considerations with potential recommendations for protective device settings changes/retrofitting equipment/remote access restrictions etc. Often mitigation recommendations are not a trivial task to perform, thus, a separate mitigation study should be performed to provide detailed information on what could be done to lower or eliminate the arc flash risks.
- Final report production

The most demanding part of the study is the data collection. The proposed methodology for data collection and verification involves record drawings verification, electrical network including protection details, ratings and settings, transformer and motor details and cable size, type and length (will be approximated from site survey or scale on layout drawings). Additionally, the switchgear should be examined, general condition, existing protection measures, environment and labelling. All circuits, distribution boards and switchboards with protective devices of 100 A and above in general are suggested to be surveyed.

During a site survey for an arc flash study, panels, switchboards, switchgear, and similar equipment may need to have their covers removed to obtain necessary data. In the absence of an arc flash study, it is the best approach to select personal protective equipment to be worn for data collection based on NFPA 70E tables.

### 3.2.3 Outcomes of the study

Four essential outcomes of the study are listed and discussed:

- Incident energy calculations at working distance (Subchapter 3.2.3.1)
- Arc flash protection boundaries calculations (Subchapter 3.2.3.2)
- Arc-rated protective clothing and personal protective equipment selection (Subchapter 3.2.3.3)
- Arc flash warning labels displaying necessary arc flash information (Subchapter 3.2.3.4)

#### 3.2.3.1 Incident energy calculations at working distance

The term “incident energy” [ $\text{cal}/\text{cm}^2$ ] refers to the thermal energy release in the arc flash at a certain distance away from the arc, which is usually the working distance. Heat energy of  $1.2 \text{ cal}/\text{cm}^2$  can cause a second-degree burn<sup>1</sup>. Thus, the severity of the arc flash is quantified through the calculations of the incident energy. The higher the incident energy, the more severe the arc flash thermal hazard. Engineering practice suggests calculating the incident energy for all locations of the electrical installation where an arc flash could potentially occur. These calculations can be performed according to the IEEE Std. 1584 [IEEE1584]. Once the incident energy is defined, it is a common practice to link the energy value with a certain hazard/risk category according to NFPA 70E [NFPA70E]. Table 3.1 presents the hazard/risk categories (HRC) with the corresponding incident energy intervals that were established by the USA NFPA. Depending on the HRC, the requirements for the protective clothing and other protective equipment can be defined when working within the arc flash boundary (see Subchapter 3.2.3.2). Appendix A presents extracts from NFPA 70E showing protective clothing and personal protective equipment tables.

---

<sup>1</sup> The calorie (cal) is the energy needed to raise the temperature of one gram of water by one °C at one atmosphere pressure. One calorie is  $\sim 4.2$  joules.

**Table 3.1** Arc flash incident energy levels with the corresponding hazard/risk category [NFPA70E].

Hazard/Risk Category (HRC)	Incident Energy
0	<1.2 cal/cm <sup>2</sup>
1	1.2-4 cal/cm <sup>2</sup>
2	4-8 cal/cm <sup>2</sup>
3	8-25 cal/cm <sup>2</sup>
4	25-40 cal/cm <sup>2</sup>
Dangerous	>40 cal/cm <sup>2</sup>

### 3.2.3.2 Calculations of the arc flash protection boundaries

The risk of electric shock when working with electricity is widely known and addressed by defining the shock protection boundaries (limited, restricted and prohibited approach boundaries) [NFPA70E]. However, the risk of the electric arc flash has only recently and gradually started to be considered in power industry risk assessments. The corresponding protection boundary for the arc flash hazard defines the closest working distance to the energised conductor or circuit part at which it is safe for the personnel to be within, without any need of further protection from the arc flash hazard [NFPA70E].

Shock and arc flash protection boundaries which are applicable to personnel exposed to energised electrical conductors or circuit parts according to NFPA 70E are presented in Figure 3.1 and should be defined in the study for each location. The shock hazard, depending on the voltage level solely, has an impact on the personnel who are working very close to the energised conductors. On the other hand, the arc flash hazard, depending mainly on the arc current and the arc duration, can have a great impact at personnel who are working even remotely from the energised conductors. Thus, the personnel might need to work within the arc flash boundary in some cases. In these cases, the required arc flash protection equipment and garments should be used.

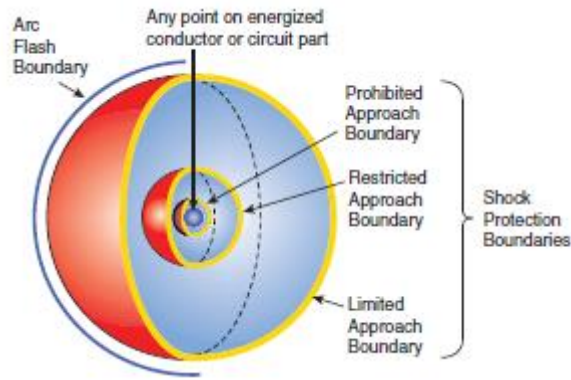


Figure 3.1 Arc flash protection boundary and shock protection boundaries [NFPA70E].

### 3.2.3.3 Arc-rated protective clothing and personal protective equipment selection

The appropriate clothing and equipment to be used when working within the arc flash boundary will be determined in the study. Appendix A presents detailed tables defining the corresponding clothing and equipment for each hazard/risk category at each location the hazard is assessed based on the NFPA 70E.

### 3.2.3.4 Arc flash warning labels displaying necessary arc flash information

Equipment labelling should be provided detailing the arc flash results and protection recommendations to ensure that the personnel should follow the safety procedures established. Two label examples are given in Figure 3.2. These labels are produced with the aid of a commercial software for power systems analysis.



	<b>DANGER</b>		<b>WARNING</b>
	<b>NO SAFE PPE EXISTS ENERGISED WORK PROHIBITED</b>		<b>ARC FLASH and SHOCK HAZARD</b>
15384 mm 383 cal/cm <sup>2</sup> Body Protection Head & Face Protection Hand and Foot Protection 690 VAC 1067 mm 305 mm 25 mm	Flash Hazard Boundary Flash Hazard at 457 mm  No FR Category Found  Do not work on live! Do not work on live! Shock Hazard when Cover is Removed Limited Approach Restricted Approach Prohibited Approach	1259 mm 6.3 cal/cm <sup>2</sup> Daily Wear FR Apparel (HRC2) = 8 Cal/cm <sup>2</sup> Minimum and Safety Shoes	Cotton Underwear + FR Shirt & Pants 4.0 - 8.0 cal/cm <sup>2</sup> Level 2 Glove Class 00 below 500V Head, Eye & Hearing Class Hardhat + Polycarbonate Face Shield + Safety Glasses + Ear Canal Inserts Shock Hazard when cover is removed 9.71 kA Bolted Fault Current
BUS-ID10-0.69kV			

Figure 3.2 Arc flash label examples [GSES15].

### 3.3 Mitigation techniques and risk management

The aim of Subchapter 3.3 is to introduce the philosophy and methodology of arc flash hazards and risk mitigation. The importance of mitigation measures in the framework of a complete and ongoing arc flash risk management is discussed. Furthermore, an overview of conventional and innovative mitigation methods is presented. Conventional control measures aim to sense the arcing fault and disconnect the supply as quickly as possible before it develops into a dangerous arc flash condition.

Neither detailed risk management process nor full review of the available mitigation methods is presented in this chapter. For further details, it is suggested to refer to additional sources available online and in the literature, for example [Das12], [WP17], [Hug16], [HSD+10], [HMS16], [RPV11], [Men15], [CLS16], [PS17], [HMH17].

#### 3.3.1 State-of-the-art mitigation methods

It is recommended that a mitigation study is performed after the arc flash hazard calculation study, when required, to decrease the dangerous incident energy levels before considering use of PPE as the last line of protection. The objective of the mitigation study is to produce recommendations on whatever could be done to reduce the energy dissipated in the case of an arc flash event. Selection of the appropriate and effective mitigation method for each installation is a complex process. Every power installation is different and requires its own unique solution.

Electrical risk reduction measures could be implemented to reduce hazard levels throughout the electrical system and the likelihood of occurrence of injury or damage. In the cases where further residual risk assessment is required arc-rated clothing and appropriate PPE should be selected for the personnel.

Mitigation methods could be divided into two categories according to their result. The mitigation methods that aim to:

- (i) reduce arc incident energy,
- (ii) reduce arc incident impact.

### **3.3.1.1 Reduction of arc incident energy**

Arc incident energy, which defines the intensity and severity of the arc flash phenomenon, is dependent on both, arcing current duration and its magnitude, which can vary widely. Potential solutions for reducing the arc incident energy include implementing protection schemes (zone selective interlocking) with proper settings of the protective devices to sense and rapidly clear any arcing fault. Fast detection and clearing of the fault is an effective way of reducing the arc incident energy. Thus, state of the art equipment, such as arc fault detection relays are used to provide even faster fault clearance than conventional relays [WP17], [Das12]. Protective devices with proper settings and good co-ordination can do much to ensure lower hazard levels. Another solution, albeit with some implementation difficulties, is to reduce arc fault current, which is dictated by the fundamental design of the power system.

Mitigation measures to reduce high incident energy levels are constantly evolving. For new installations, innovative equipment and design methods are constantly being developed and implemented. However, for legacy installations, options for the reduction of hazard levels, including replacement or addition of equipment, are usually limited.

### **3.3.1.2 Reduction of arc flash impact**

Potential solutions for reducing the impact of arc flash incidents include remote operation and the use of arc-resistant (personal protection) equipment which can, if used correctly, protect personnel from arc flash hazards. It should be noted that these solutions generally do not reduce the impact of the arc flash incident on the equipment/facility but provide protection for personnel.

### **3.3.1.3 Methods combination**

A different approach to mitigation is an introduction of an alternative current path (crowbar) to transfer and, subsequently, capture the arcing fault. Thus, this method reduces both the arc incident energy and the arc incident impact by providing a lower impedance path than the fault path, fast transfer and containment of the arc.

### 3.3.1.4 Other mitigation methods: Practical engineering approaches

In addition to the previously discussed mitigation practices, there are several methods derived from engineering practice that could be implemented for arc flash mitigation.

According to the literature [Das12], [PVL13], the following practices are sometimes adopted during an electric/power system maintenance:

- Temporary reduced settings in protection devices
- Operating with an open tie (when buses are connected via bus-tie breakers)

Reduced settings provide more sensitive and faster interruption of the arcing fault, but, usually, this cannot be implemented as a permanent solution because it could result in undesired tripping under normal operating conditions. Similarly, operating with open bus-tie breakers reduces the overall power plant reliability, and usually cannot be implemented as permanent solution.

During system design, consideration of the following is suggested:

- A single main circuit breaker for system shutdown
- Step-down transformers no larger than 125 kVA to reduce the available fault current
- Adjustable low voltage power circuit breakers instead of standard thermal magnetic circuit breakers to reduce fault clearing time
- Infrared windows to enable operator to perform IR scans without removing switchgear side panels, lessening the likelihood of arc flash events caused by accidental contact with live busbars

Although there are various available solutions, they may not always be feasible. For example, the case where the transformer's primary protection fuses already have the minimum recommended rating. In such cases, no change in protection settings can be implemented. Addition of secondary protection fuses, in the cases where no secondary protection is initially installed, could reduce the arc incident energy. However, it may not be feasible because this may require additional interconnecting cables that are costly and potentially difficult to install. Thus, remote operation might be best solution for such cases.

### 3.3.1.5 Predict and prevent faults

Sensitivity to low current faults and achieving rapid arc fault detection can provide an enhanced level of protection when an arc flash occurs. However, when trying to predict and



prevent faults, it is important to investigate the conditions that cause them. Knowledge of the conditions helps to anticipate and eliminate the occurrence of the incident. For example, one relevant technique is to monitor insulation integrity by detecting partial discharges which indicate one potential failure mode [LBR17], [HHJ+12], [LRB+11].

### **3.3.2 A comprehensive system to manage arc flash hazards**

Understanding the hazards to identify potential mitigation actions to prevent or minimise effects of an arc flash accident is critically important. A comprehensive management system of arc flash hazards includes hazard identification, detailed assessment, prevention and mitigation and provides operators with the following benefits:

- Understanding the main areas of risk to personnel operating and maintaining electrical equipment (hazard/risk category identification throughout the electrical system).
- Ability to plan, design and apply mitigation measures to reduce higher levels of incident energy.
- Application of hazard reduction measures to eliminate or reduce the need to implement cumbersome and unnecessary PPE with high levels of protection for frequent maintenance and switching activities.
- Visibility to display the levels of risk and required PPE through comprehensive safety labelling.
- Compliance with relevant legislation regarding electrical safety.

## **3.4 Arc flash hazard calculation studies results**

Data derived from arc flash studies conducted by GSE Systems<sup>2</sup> (former TAS Consultancy) [GSES15] for 97 facilities are analysed in Subchapter 3.4. Particularly, the incident energies of all buses both in high voltage (HV) (>1000 V) and low voltage (LV) (<1000V) systems are considered. The associated arc incident energy levels are determined based on calculations in accordance with the IEEE Std. 1584 allied to NFPA 70E Standard. The sites which were assessed for arc flash hazards covered a wide range of power generation plants

---

<sup>2</sup> GSE Systems is the industrial collaborator for the project.

(along which a wind power plant), manufacturing facilities, process plants, papermaking, minerals, oil and gas or petrochemical plants, ship installations, office and research facilities.

The data encompasses a large range of facility sizes, from a small site with 5 buses to a large site with 328 buses. The total number of the buses analysed is 8143, of which 7199 are LV buses and 944 are HV buses. The low levels of bus voltages are not always a good indicator for the incident energy and arc flash hazards expected [DSB09], as shown in Figure 3.3.

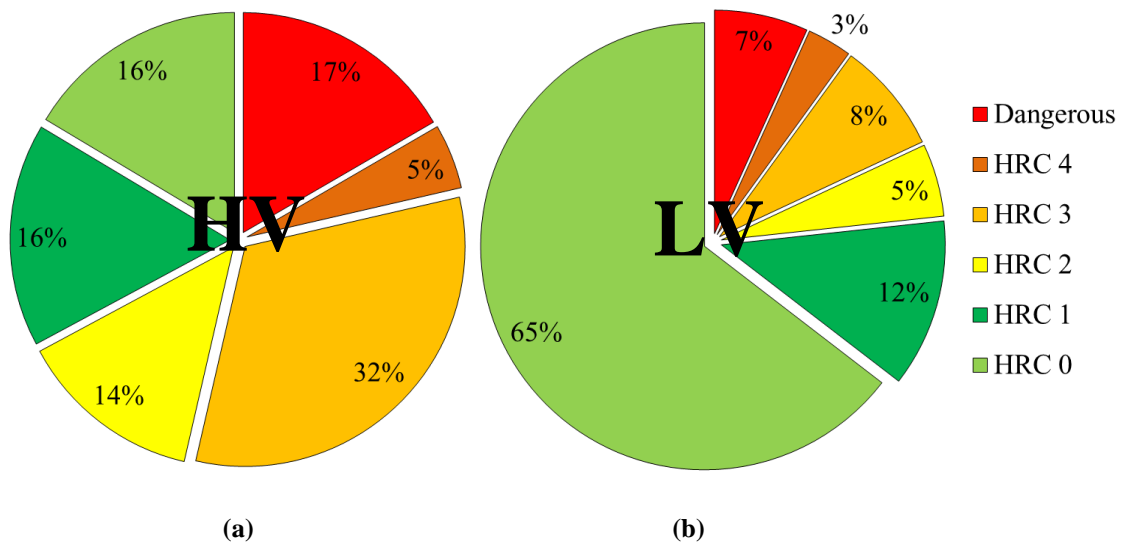


**Figure 3.3** Analysis of incident energies in a wide range of power generation plants (along which a wind power plant), manufacturing facilities, process plants, papermaking, minerals, oil and gas or petrochemical plants, ship installations, office and research facilities (97 sites); total number of buses 8143, of which (a) 944 are HV buses and (b) 7199 are LV buses. The HRC ranges are defined in Table 3.1.

Despite the potential perception that only HV buses present high levels of incident energy, LV buses can present dangerous hazard levels as well. Actually, most arc faults occur in LV switchgear, because electrical arc flash severity depends not only on the arc voltage but is also a function of the arcing fault current of the system and arc duration. LV systems can carry high currents; thus, they are more prone to arc flash events. Additional contributing factors to occurrence of arc faults in LV switchgear could be large motor overcurrent contributions, lower quality components installed in LV circuits, less stringent operating procedures, inappropriate protection settings and inadequate design before extending LV networks. Moreover, operators are working more often with LV (interactions with energised electrical equipment) and are generally more aware of the risks when working with HV. Live

working on exposed HV systems and equipment is very much less than work on live LV systems and equipment.

Figure 3.4 to Figure 3.6 shows a breakdown analysis of the results for the different types of facilities categorised in three wider types:

- **Type 1 facilities:** Power generation plants, including different types along with a wind power plant.
- **Type 2 facilities:** Manufacturing facilities, process plants, papermaking, minerals, oil and gas or petrochemical plants, ship installations.
- **Type 3 facilities:** Lighter manufacturing facilities, office and research facilities.

In power generation plants, the percentages of dangerous categories in HV systems are quite high. Thus, particular care should be taken at these facilities, Figure 3.4. 69% of the HV buses examined are categorised as dangerous. These results are strongly affected by the extremely high levels of arc flash energy calculated for the wind power plant site. This could be attributed to the fact that the clearing time of the arcing fault is approximately 2 seconds for all the buses of the distribution network considered in the particular wind farm. However, even without including the wind farm in the final results, the percentage of HV buses categorised as dangerous is still quite high ~50%.

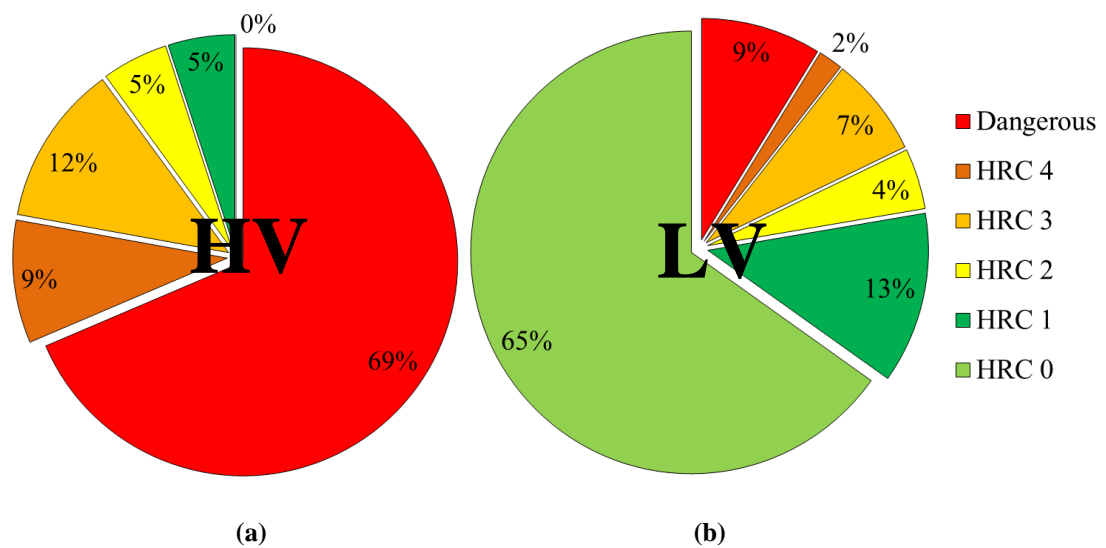


**Figure 3.4** Analysis of incident energies in Type 1 facilities - power generation plants; total number of buses 1762, of which (a) 140 HV buses and (b) 1622 LV buses.

In manufacturing facilities, process plants, papermaking, minerals, oil and gas or petrochemical plants, ship installations almost half of the HV buses, 47%, exhibit arc flash

hazard levels > 8 cal/cm<sup>2</sup> (HRC 3 and higher), Figure 3.5. For the LV buses, almost a quarter of them, 23%, exhibit arc flash hazard levels > 8 cal/cm<sup>2</sup>.

In lighter manufacturing facilities, office and research facilities, more than half of the HV buses, 55%, exhibit arc flash hazard levels > 8 cal/cm<sup>2</sup>, Figure 3.6. For the LV buses, 10% of them exhibit arc flash hazard levels > 8 cal/cm<sup>2</sup>.

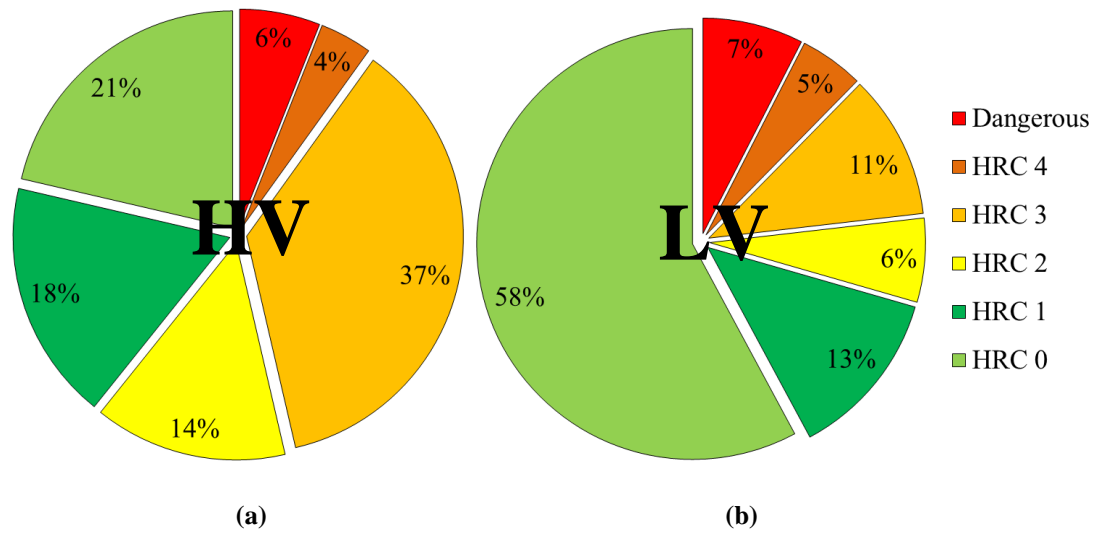


**Figure 3.5** Analysis of incident energies in Type 2 facilities - manufacturing facilities, process plants, papermaking, minerals, oil and gas or petrochemical plants, ship installations; total number of buses 4113, of which (a) 716 HV buses and (b) 3397 LV buses.

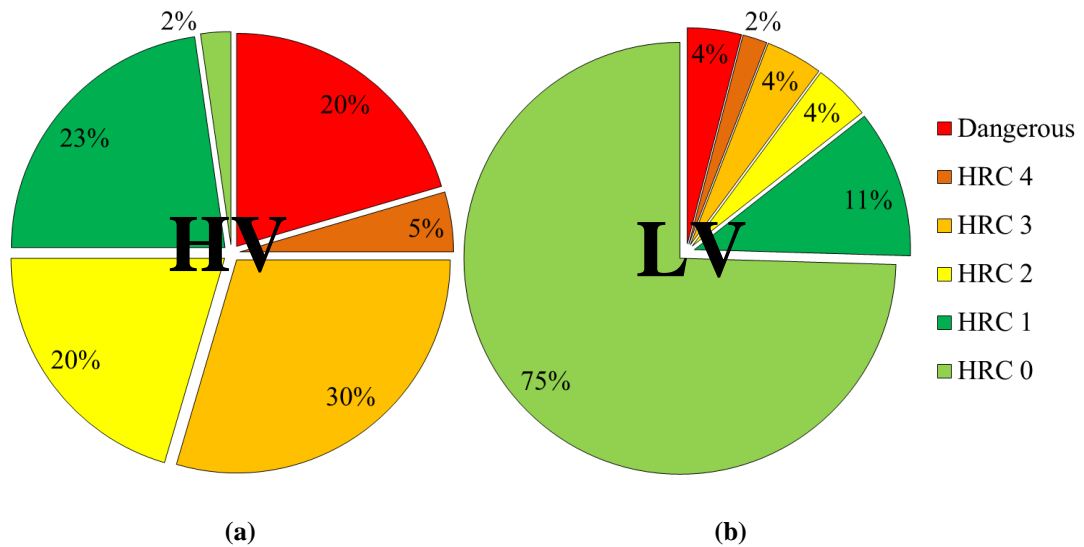


**Figure 3.6** Analysis of incident energies in Type 3 facilities - lighter manufacturing facilities, office and research facilities; total number of buses 2268, of which (a) 88 HV buses and (b) 2180 LV buses.

All incident energy levels can occur in any facility type. Moreover, all types of facilities can exhibit dangerous incident energy levels. Issues in existing facilities, such as (i) LV switchgear fed by large transformers, (ii) transformers protected only by a primary fuse that takes a long time to open during a secondary fault, (iii) circuit breakers trip units configured with settings higher than required for effective coordination, can result in increased incident energy levels [DSB09]. Observations related to safety around the site such as equipment located near walkways, lack of proper maintenance and switchgear risk assessment to confirm the protection relay settings, and poor equipment construction with access to live connections can be recorded during the site survey.

Factors that increase the likelihood of arc flash occurrence could be poor or no regular maintenance of the equipment, old equipment, poorly trained operators and no set standards to work and lack of awareness. Additionally, staff may still fail to respond to the message even after clear unambiguous labelling.

### **3.5 Arc flash hazard risk mitigation studies results**

Arc flash hazard calculation studies in Subchapter 3.4 showed potentially dangerous incident energy levels at several electrical installations of the sites analysed. Thus, it is crucial to design and apply mitigation measures to reduce further these levels of incident energy to protect staff from harm and reduce risk of damage to the facility in the case of an arc flash event. Additionally, application of hazard reduction measures would result in the reduction of required PPE levels to protect against the hazard, reducing the need to implement cumbersome PPE for frequent maintenance and switching activities.

Levels of incident energy that exceed  $40 \text{ cal/cm}^2$  are of the highest concern for mitigation. For these levels of energy, there is no PPE available that could adequately protect personnel. Incident energy levels of category 3 and 4 should also be reduced wherever possible. Although there is PPE available for these categories, it is heavy, cumbersome and uncomfortable for workers. Moreover, such levels of energy might result in additional hazards besides the thermal one, for example, intense blast pressure waves might throw workers across a room. The general trend in mitigation is to shift the number of buses exhibiting high incident energy levels to lower hazard risk categories.

Mitigation studies were carried out for 26 of the aforementioned sites. The data includes 1 power generation plant, 17 manufacturing facilities, and 8 offshore facilities (ship

installations). The range of facility sizes varies from a large site with 219 buses to a small site with 11 buses. The total number of the buses considered as part of the mitigation studies was 1923, of which 1846 were LV buses and 77 were HV buses. The mitigation methods proposed for each installation are summarised in Table 3.2. Selection of the appropriate and effective mitigation method for each installation is quite a complex procedure. Every installation is different and requires its own unique solution to ensure that risk is reduced as much as possible, within the limitations of the particular system and that risk reduction measures are cost effective and result in minimum operational impact.

In 8 of the installations, the proposed mitigation method was insertion of arc flash relays. In further 17 installations, reducing fuse ratings or change/reduction of protection settings in circuit breakers or replacing fuses with circuit breakers or a change of circuit breaker type were suggested. Remote operation was recommended for the final installation where no other mitigation method was feasible. A combination of mitigation methods can also be proposed to achieve better protection and safety, for example, reduction of fuse rating combined with remote operation. After mitigation, the incident energy levels show notable reductions.

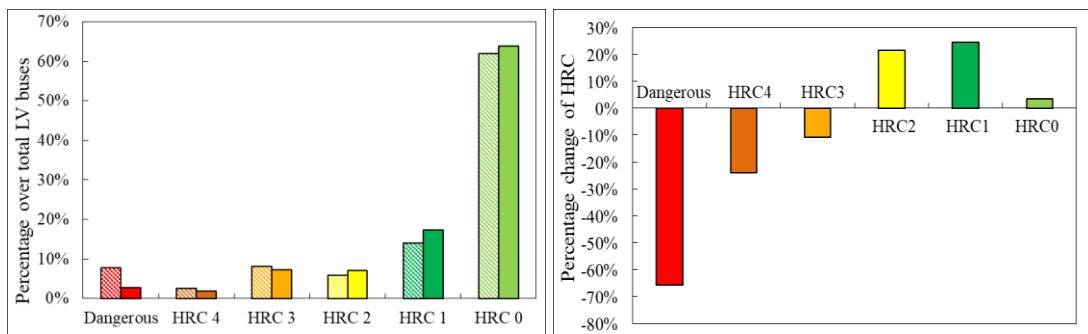
**Table 3.2** Proposed mitigation method for the 26 installations.

No. of installations	Proposed mitigation method
14	Reducing fuse ratings or change/reduction of protection settings (relays)
3	Replacing fuses with circuit breakers or change of circuit breaker type
8	Installation of arc flash relays
1	Remote operation

Figure 3.7(a) presents the pre- and post-mitigation data derived from 26 arc flash studies for ship installations, manufacturing facilities and a power generation plant for LV buses. Figure 3.7(b) presents the percentage changes in hazard/risk categories. The number of LV buses in HRCs 3, 4 and dangerous decreased significantly. The number of buses in the dangerous category reduced by 66.0%, while the number of HRC 0 buses increased by 3.3%.

After mitigation, 1181 out of 1846 LV buses exhibited category 0 incident energy levels. Furthermore, the LV buses in the dangerous category were 94 less, resulting in 49 LV buses remaining in the dangerous category. 121 fewer LV buses exhibited hazard levels exceeding 8 cal/cm<sup>2</sup>. Overall, a reduction of 36% in the total number of LV buses in HRCs 3, 4 and dangerous was observed.

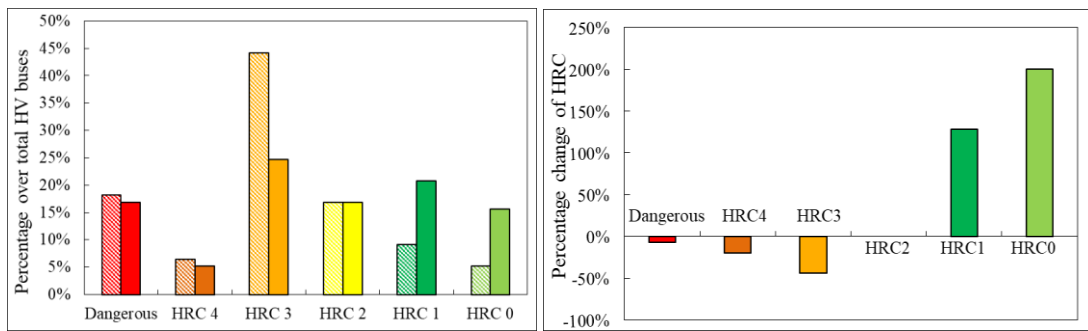
The number of HV buses in the dangerous category reduced by 7.1 %, while the number of HRC 0 buses increased by 200.0 %, Figure 3.8(a) and Figure 3.8(b). After mitigation, a reduction of 20.0% and 44.1 % in the number of HV buses in the category 3 and 4, respectively, was observed. Overall, 32.1% reduction in the total number of HV buses in dangerous, 3 and 4 category was observed.



(a)

(b)

**Figure 3.7** (a) Analysis of incident energies pre- and post-mitigation and (b) percentage change of incident energies post-mitigation in ship installations and manufacturing facilities and a power generation plant; 1846 LV buses.



(a)

(b)

**Figure 3.8** (a) Analysis of incident energies pre- and post-mitigation and (b) percentage change of incident energies post-mitigation in ship installations and manufacturing facilities and a power generation plant; 77 HV buses.

### 3.6 Conclusions

Data derived from arc flash studies conducted by GSE Systems (former TAS Consultancy) for 97 facilities have been analysed. Particularly, incident energies of all buses both in HV (>1000 V) and LV (<1000V) systems have been considered. The sites which were assessed for arc flash hazards covered a wide range of power generation plants (along which a wind power plant), manufacturing facilities, process plants, papermaking, minerals, oil and gas or petrochemical plants, ship installations, office and research facilities. The data encompasses a large range of facility sizes, from a small site with 5 buses to a large site with 328 buses. The total number of the buses analysed is 8143, of which 7199 are LV buses and 944 are HV buses. The following main conclusions have been derived:

- Both HV buses and LV buses can exhibit high levels of arc incident energy levels.
- All incident energy levels can occur in any facility type.
- All types of facility can exhibit dangerous incident energy levels.

It is recommended that a mitigation study is performed after the arc flash hazard analysis, when required, to decrease the dangerous incident energy levels before considering use of PPE. The objective of mitigation study is to make recommendations on whatever could be done to lower the energy dissipated in the case of an arc flash event.

Mitigation studies were carried out for 26 of the aforementioned sites. The data includes 1 power generation plant, 17 manufacturing facilities, and 8 offshore facilities (ship installations). The range of facility sizes varies from a large site with 219 buses to a small site with 11 buses. The total number of the buses considered as part of the mitigation studies was 1923, of which 1846 were LV buses and 77 were HV buses. The following main conclusions have been derived:

- Every installation is different and requires its own unique solution to ensure that risk is reduced as much as possible.
- In some cases, the hazard can be reduced without significant investment in equipment.
- The use of PPE is suggested as the last line of protection.

Analysis of the arc incident energies pre- and post-mitigation to reduce hazard levels shows that risk control measures can lead to significant reductions in potential harm and damage should an arc flash occur. However, the discussed mitigation methods alone do not prevent



arc initiation. Thus, an investigation into the initiation of electrical arcs within the context of a study into novel approaches to understand the hazard posed during the arcing fault onset is conducted in the present thesis and reported in the following chapters.

## Chapter 4

---

# Experimental set-up

Design of the experimental topology and selection of diagnostic devices is important for accurate acquisition of the electrical characteristics of the arc plasma channel discharge during its initiation phase. The experimental set-up should meet the basic design requirements presented in Subchapter 4.1.1. The experimental test system and the diagnostic equipment used for the development and characterisation of spark discharges is presented in subchapters 4.1 and 4.2. The preliminary tests conducted to validate the suitability of the developed set-up for investigation of the transient characteristics of arc discharges in their initial phase are also discussed in Subchapter 4.3.

## 4.1 Experimental design

### 4.1.1 Design requirements

The experimental set-up should be designed to meet the following four main criteria for acquiring accurately the arc plasma channel discharge waveforms:

- i. The test system should not distort the characteristics of the arc plasma discharge, or, at least, the characteristics of the arc plasma discharge should be distorted as little as possible by the experimental set-up.
- ii. The test system should withstand several discharges without any major destructions taking place in the system.
- iii. The test system should allow for variations in the circuit to examine arc plasma discharge onset under various electrical and topological initial conditions and parameters.
- iv. The test system should include at least one busbar to represent a topology similar to industrial configuration (busbar location is one of the most likely locations for a severe arc flash incident to occur).

For the scope of the present study, two similar experimental topologies have been designed and built and two sets of high voltage tests have been conducted. For the first set of tests, the original topology described in Subchapter 4.1.3 was used. During the first set of tests, spark discharges were generated in a self-breakdown air spark gap (SBSG). Then, the SBSG topology was slightly amended to be used for the second set of tests where discharges were initiated with a thin conducting wire, (wire-guided spark gap (WGSB)). Subchapter 4.1.4 describes in details the development of the second topology created and used in the study. Before detailing the characteristics of these two designs, the simplified block diagram of the general set-up is presented in Subchapter 4.1.2.

### 4.1.2 Simplified block diagram of the experimental set-up

The simplified block diagram of the experimental set-up is shown in Figure 4.1. A HV DC power supply is utilised to charge a capacitor through a current limiting resistor (not shown in the diagram). The main spark gap used to create and study the discharges is shown in the block diagram. This main spark gap is amended from a SBSG to a WGSB to allow initiation of spark discharges within the inter-electrode spark gap in a wide range of distances, from sub-mm gaps to a few cm gaps. A plasma closing switch (PCS) is utilised only in the case of the WGSB to allow stored energy to be delivered in the discharge. Current and voltage diagnostic devices are used to capture the electrical waveforms of short transient arc discharges which are described in detail in the present subchapter. Finally, the acquired waveforms were analysed with the aid of MATLAB/Simulink software.

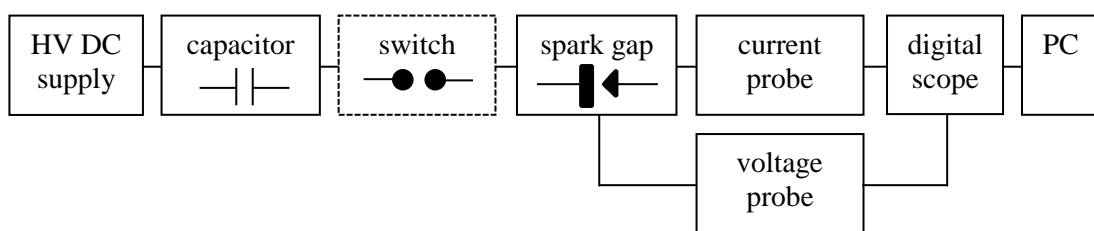


**Figure 4.1** Simplified block diagram of the experimental set-up.

### 4.1.3 SBSG topology

Subchapter 4.1.3 presents the components of the self-breakdown spark gap topology and the measurement circuitry. The design meets the main requirements, presented in

Subchapter 4.1.1, for acquiring accurately waveforms. Figure 4.2 shows the topology elements (with the corresponding numbering) of the capacitive energy storage circuit with the SBSG and the measurement circuitry.

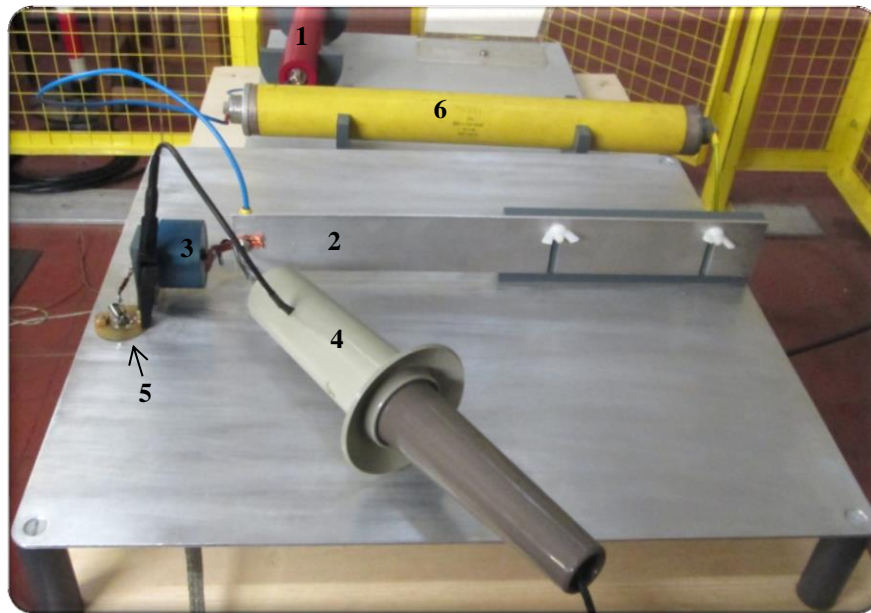


**Figure 4.2** The capacitive energy storage circuit with the self-breakdown spark gap and the measurement circuitry. 1, charging resistor; 2, busbar; 3, capacitor; 4, HV probe Tektronix P6015A; 5, voltage-dividing current shunt; 6 safety/discharge resistor, **195 M $\Omega$** .

### 1. Charging resistor

A charging resistor,  $R_{ch}$ , which was 25 M $\Omega$  in the present study, limits the current from the HV DC supply while charging the capacitor, thus it protects the HV DC supply. The time constant of the charging system varies from ~25 ms to ~135 ms for capacitor values from 1 nF to 5.4 nF. The estimated time for the system to be fully charged (~5 times the time constant) is approximately from ~125 ms to ~675 ms for the aforementioned capacitor values range.

### 2. Self-breakdown spark gap (SBSG)

The self-breakdown spark gap used to create and study short transient arc discharges, of the order of several hundreds of ns, consists of a horizontal aluminium busbar used as a high voltage electrode and a base plate with a protruding point brass electrode used as the earth electrode, Figure 4.3. The aluminium busbar has similar dimensions (50 mm width, 40 cm

length and 3 mm thickness) as the busbar used in the industrial topologies. Busbars dimensions used in HV ( $> 1000$  V) switchgear or in LV ( $< 1000$ V) power distribution boards utilised in industrial installations can vary widely based in the operational current of the system. The cross-sectional size of the busbar is designed to be able to carry the rated current and to withstand the peak current expected under faulty conditions. In the experiments conducted in the present work, the voltage levels used are in the HV range. The currents measured are peak current expected under faulty conditions. The cross-sectional size of the busbar used in the experiments is capable to withstand the expected peak current. The protruding electrode is used to create the strongly non-uniform field to induce ionisation of the air and breakdown. This allows keeping the spark initiation voltage manageably low. The spark gap length is adjustable by varying the height of the earth electrode using a screw thread. Polyvinyl chloride (PVC) insulation was used to support the high voltage electrode. The discharge initiation is achieved by applying the voltage across the electrodes of the spark gap which exceeds the breakdown voltage of the gap. The gap distances studied in the present work are sub-mm gaps. Such small gaps can be found in practical industrial installations only under faulty conditions. An example of such faulty topology can be found in the case when the joint of a busbar is not firmly screwed, and this creates a small gap in the joint locally. A mechanical failure may also result in the development of such small gaps.

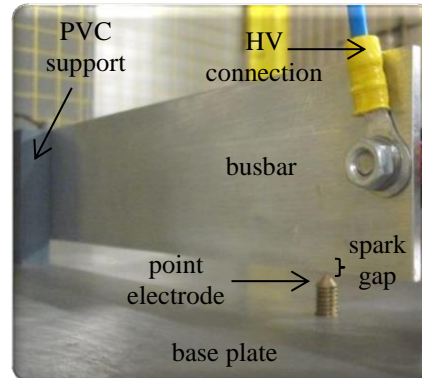


**Figure 4.3** The SBSG and the base plate with the protruding point brass electrode.

### 3. Capacitor

A high voltage ceramic capacitor,  $C$ , is used to store the energy in the system and deliver it to the discharge when required. Four different capacitor values are examined, 1.0 nF (4 kV, Vishay Ltd), 1.9 nF (30 kV, Morgan Electro Ceramics Ltd), 2.7 nF (30 kV, Morgan Electro Ceramics Ltd), and 5.4 nF (2 x 2.7 nF, 30 kV Morgan Electro Ceramics Ltd).

#### 4. HV probe

A 20-kV direct current, 40 kV peak impulse, Tektronix P6015A HV (1000:1) probe is used to measure the voltage waveform of arc discharges. High voltage transients, similar to the arc discharge under study, can be measured using a compensated voltage divider (resistive and capacitive (RC) divider) [Jon88]. The HV probe used in the present work is designed as a compensated voltage divider composed of capacitor in parallel with resistors to provide the required frequency response. Also, series damping resistors are connected in series with the RC parallel combination to achieve mitigation of any circuit resonances.

#### 5. Voltage-dividing current shunt

A voltage-dividing current shunt was custom-built for current sensing in the SBSG topology, Figure 4.4. There was a necessity for developing measuring equipment to fit within miniature dimensions of the SBSG topology which simultaneously should withstand the high voltage levels. For example, it was found that it is difficult to place a Rogowskii coil in the experimental set-up for current measurement due to its relatively large dimensions compared to the loop including the sub-mm spark gap. The current shunt method was chosen over other options for the SBSG because of its very fast rise time response and its measuring accuracy. Moreover, the shunt can be easily calibrated [Tho70]. Another important characteristic of the custom-built design is that allows developing a current shunt with very small dimensions that can be easily inserted in the developed test circuit. Since the shunt is directly located in the electrical circuit under investigation, efforts have been made to optimise its design to minimise additional inductance inserted in the circuit.

The first resistive divider was developed using an RG-58/U coaxial cable soldered on the terminals of the current sensing resistor  $0.01 \Omega$  (0.5 W) which was in series with a limiting resistor  $1 \Omega$  (35 W). This design created a loop with the current sensing resistor and the coaxial cable and induced voltage due to magnetic flux in the area. Thus, an incorrect current value was measured. Therefore, there was a need for eliminating this electromagnetic coupling of the divider through a new design. The new design of the divider was tested and finally adopted in the measurements conducted in the SBSG topology.

The new voltage-dividing current shunt comprises a limiting resistor  $1 \Omega$  (35 W) and the current sensing resistor  $0.025 \Omega$  (4 W). The current sensing resistor has a symmetrical distribution of four parallel-connected chip resistors of  $0.1 \Omega$  (1 W) each to minimise inaccuracy in the measurements due to electromagnetic induction. A thin brass sheet was

used as the earth contact for the resistors. An RG 402 semi-rigid coaxial cable was used with its copper sheath soldered through the brass sheet. The semi-rigid cable was nominally 1 m in length and terminated in a soldered-on SMA connector, which was adapted to a normal flexible RG-58/U coaxial cable connected to the oscilloscope. Due to the high levels of current that might occur (particularly if the  $1\ \Omega$  resistor should fail), there is a need for further attenuation of the signal reaching the oscilloscope to protect it. Thus, two 20 dB, 50-ohm attenuators (40 dB total) were inserted at the input of the channel of the oscilloscope.

To mitigate the effect of any parasitic capacitive coupling through the  $1\ \Omega$  resistor that may arise due to the high rate of change of voltages and currents in the discharge, 1 nF and 22 nF capacitors were connected in parallel with  $0.025\ \Omega$  and  $1\ \Omega$  resistors to provide the same capacitive division ratio, creating a compensated resistive divider. The capacitor values were validated with the aid of the circuit model development in PSpice software.

The calibration of the voltage-dividing current shunt performed is now described. Initially, the shunt was connected to a DC supply and 1 A current was flowing through the shunt. The input voltage across the  $1\ \Omega$  and  $0.025\ \Omega$  resistors was measured. The output voltage across the  $0.025\ \Omega$  resistor was measured. The division ratio of the output voltage over the input voltage was calculated approximately 1/41.

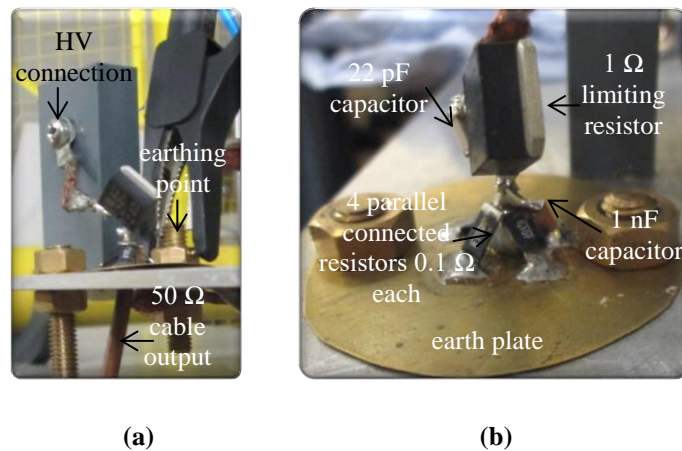


**Figure 4.4** (a) The voltage-dividing current shunt with its high voltage and grounding connections, (b) Details of the construction of the voltage-dividing current shunt.

#### 6. Discharging resistor

For safety reasons, a discharging resistor,  $R_{sf}$ ,  $195\ \text{M}\Omega$  is connected in parallel with the capacitor in order to remove any residual charges from the system when the power supply is

switched off. The discharging/safety system has a time constant from  $\sim 0.2$  s to  $\sim 1$  s for capacitor values from 1 nF to 5.4 nF. The estimated time for the system to be fully discharged from residual charges is from  $\sim 1$  s to  $\sim 5.3$  s for capacitor values from 1 nF to 5.4 nF.

#### 4.1.3.1 SBSG equivalent circuit

The equivalent circuit of the capacitive energy storage circuit with the SBSG and the measurement circuitry is given in Figure 4.5. The spark gap was tested in atmospheric air at room temperature and the gaps examined were sub-mm gaps, from 0.1 mm to 1 mm, applied voltage levels were from 1 kV to 5 kV. Such lengths of gap, as mentioned earlier, are not commonly found in practical electrical equipment since design engineers ensure the required distance between busbars in the switchboards (typical distances in high voltage switchgear are between 10 to 100 mm for 1 to 5 kV ratings).

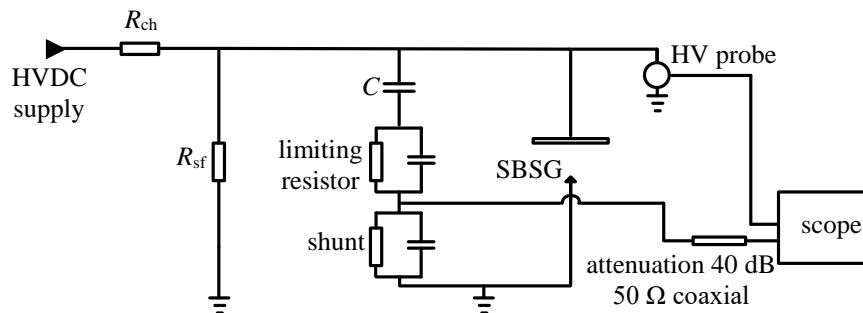


**Figure 4.5** Equivalent circuit of the capacitive energy storage circuit with the spark gap and the measurement circuitry.

#### 4.1.4 WGSG topology

Subchapter 4.1.4 presents the components of the wire-guided spark gap topology and the measurement circuitry. The design meets the main requirements, presented in Subchapter 4.1.1, for acquiring accurately waveforms. Figure 4.6 shows the topology elements (with the corresponding numbering) of the capacitive energy storage circuit with the WGSG and the measurement circuitry.



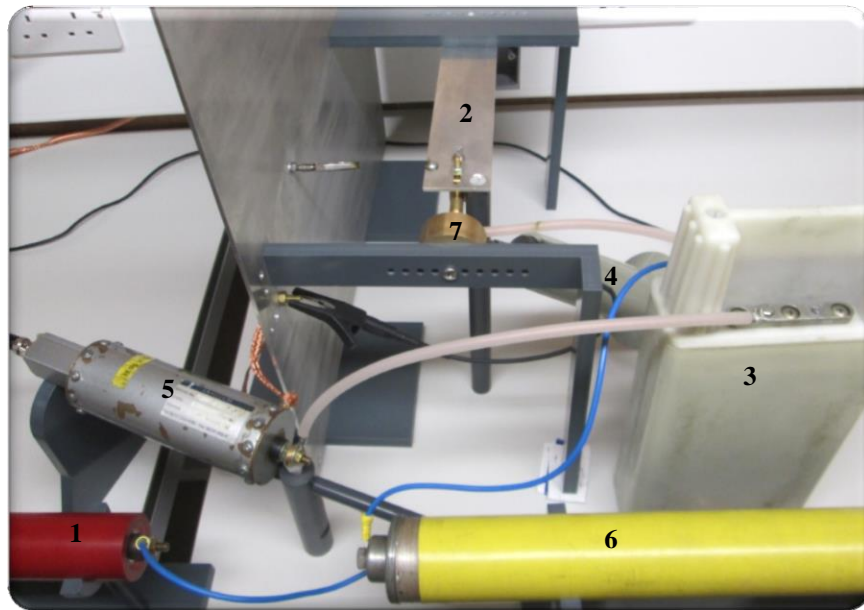


**Figure 4.6** The capacitive energy storage circuit with the wire-guided spark gap and the measurement circuitry. 1, charging resistor; 2, busbar; 3, capacitor; 4, HV probe; 5, current shunt; 6, safety/discharge resistor,  $195 \text{ M}\Omega$ ; 7, plasma closing switch.

### 1. Charging resistor

A charging resistor,  $25 \text{ M}\Omega$ , limits the charging current from the HV DC supply while charging the capacitor and protects the supply. The time constant of the charging system is calculated  $\sim 2 \text{ s}$  for capacitor value of  $80 \text{ nF}$ . The estimated time for the system to be fully charged ( $\sim 5$  times the time constant) can be approximately calculated  $10 \text{ s}$  for the aforementioned capacitor value.

### 2. Wire-guided spark gap (WGSG)

The busbar gap used in the SBSG discharges has been amended to study short transient arc discharges which last several  $\mu\text{s}$  in the present WGSG topology. The discharges being initiated with thin conductive wires (99.9 % copper,  $0.05 \text{ mm}$  diameter) placed between the busbar and the grounded plate (a wire-guided spark gap, WGSG). The protruding point electrode at the grounded plate was replaced by an electrode with a crocodile clip at the edge to support the one end of the wire. A clearance hole was drilled in the busbar and a thread was inserted to support the other end of the wire. The discharge initiation is achieved

through the fast Joule evaporation of the 50- $\mu\text{m}$  diameter thin Cu wire placed between the electrodes.

Figure 4.7 presents the amended spark gap. A plasma closing switch (PCS) is required to be inserted in the circuit between the wire-guided spark gap and the capacitor. The PCS is discussed later within this subchapter.

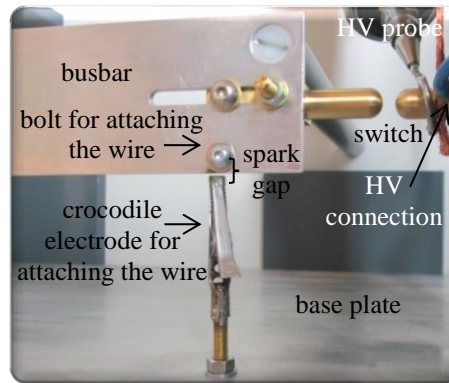


**Figure 4.7** Wire-guided spark gap and the base plate with the crocodile where the wire can be attached.

### 3. Capacitor

An 80 nF capacitor (Maxwell Ltd) is used to store the energy in the system and deliver it to the discharge when required. The capacitor withstands voltages up to 100 kV.

### 4. HV probe

The breakdown voltages were measured using either a North Star PVM-5 HV probe (1000:1, 100-kV peak pulse) or the Tektronix P6015A HV probe (1000:1, 40-kV peak pulse) used also for the SBSG topology. The nominal bandwidth of these probes is 80 and 75 MHz.

### 5. Tubular current shunt

A Samtech DE(CP)-01 tubular current shunt with a sensitivity of 13.96 V/kA and nominal resistance of 15 m $\Omega$  was used to measure the transient current. This tubular shunt with low inductive design was chosen over other options because of its fast response and its measuring accuracy, since it is considered to react as a pure ohmic resistor that has no self-inductance. The use of the shunt requires interruption of the circuit conductors. The shunt needs to be electrically-inserted into the loop in series with the WGSG. Efforts have been

made to optimise the circuit design to provide minimum inductance. The two 20 dB, 50-ohm attenuators (40 dB total) were inserted at the input of the channel of the oscilloscope for extra protection.

#### *6. Discharging resistor*

For safety reasons a discharging resistor 195 M $\Omega$  is connected in parallel with the capacitor in order to remove any residual charges from the system when the power supply is switched off. The discharging time constant for an 80 nF capacitor is  $\sim 15.6$  s. The estimated time for the system to be fully discharged from residual charges is calculated  $\sim 78$  s. A discharge stick is used for extra protection after each repetition of the testing to ensure that the system is fully discharged before replacing the copper wire for the next test.

#### *7. Plasma closing switch (PCS)*

A plasma closing switch is inserted in series with the capacitor and serves to deposit the required energy for the short transient arc discharge across the WGSG. The inter-electrode gap of the PCS (4 mm) was selected to limit the breakdown voltage to  $<20$  kV and the energy available in the discharge to  $<10$  J. The design of the switch is a simple two electrode self-breakdown design to avoid any further complexity in the circuit.

#### **4.1.4.1 WGSG equivalent circuit**

The equivalent circuit of the capacitive energy storage circuit with the WGSG and the measurement circuitry is given in Figure 4.8. The wire-guided discharge allowed the inter-electrode gap to vary between 1 to 8 cm for applied voltages below 20 kV. The gaps examined are in the same range of typical gap distances of the industrial high voltage equipment, between 1 to 15 cm for 1 to 15 kV ratings. The tests were conducted under normal laboratory conditions, an average temperature of 23  $^{\circ}\text{C}$  and an average of relative humidity of air 37 %.

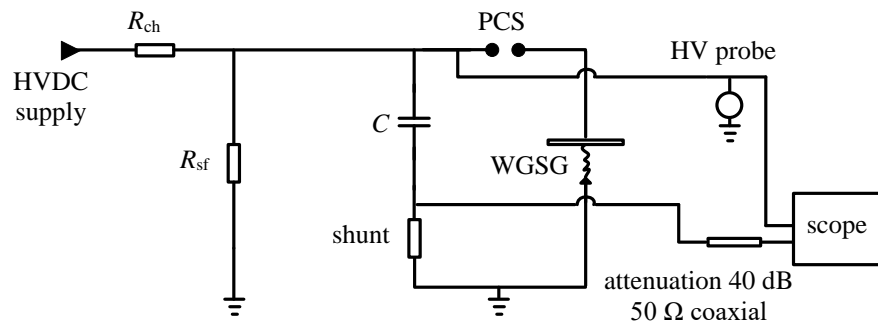


**Figure 4.8.** Equivalent circuit of the capacitive energy storage circuit with the wire-guided spark gap and the measurement circuitry.

## 4.2 Diagnostic and monitoring techniques

The measurable arc characteristics can be generally divided into three categories: electrical, aerodynamic and radiative [Jon88] which include the following parameters:

- i. Electrical parameters: current and voltage, voltage distribution and current density
- ii. Aerodynamic parameters: pressure, flow velocity, arc core boundary, flow and thermal boundary, total enthalpy
- iii. Optical parameters: optical emission spectra, light scatter

The focus of the present study is on the measurement of arc electrical parameters, transient voltage and current waveforms.

### 4.2.1 Electrical parameters measuring techniques

High voltage probes and current shunts, as mentioned in the previous subchapter, were used to capture voltage and current waveforms of the arc plasma discharge. Limitations of each method should be considered, and procedures should be established to achieve accurate measurements of the arc characteristics, behaviour and processes taking place during the discharge.

Arc electrical characteristics acquisition can be quite challenging, since it involves high current and high voltage measurements. Moreover, the event of an arc plasma discharge initiates very fast, involving high  $dV/dt$  and  $dI/dt$ , and lasts limited time within which the measurement should take place. Different events that should be measured can take place within few ns. Thus, a proper measuring system with the adequate time response, less than the time scales within which the arc discharge develops, should be utilised.

Moreover, for measurement accuracy, the design of diagnostic devices should meet the additional requirements described below:

- i. The current sensing element's impedance (resistance and inductance) should be smaller than the current supply circuit's impedance (at least two orders of magnitude smaller).
- ii. Resonant oscillations should be avoided trying to keep stray capacitances as small as possible.
- iii. The signal to noise ratio should be acceptable for recording purposes.
- iv. The current measurement circuit should stay unaffected by the electromagnetic stray fields derived from the main circuit. Additionally, the circuit should be capable to withstand the electromagnetic forces developed during the maximum arc peak currents.

#### **4.2.1.1 Current measurements**

A widely used approach to current measurements is the use of the current shunt. The current shunt was chosen over other current sensing options because of its fast response time and its measuring accuracy. Since the use of the shunt requires interruption of the circuit conductors, efforts have been made to optimise the circuit design to insert minimum inductance in the loop. The custom-built shunt needs to be electrically-inserted into the loop in series with the SBSG and the tubular shunt in series with the WGSG. The optimum accuracy is achieved when the shunt behaves as a pure ohmic resistor with zero (or very low) self-inductance. Generally acceptable resistance and rise time values are of the order of tens of m $\Omega$  and less than 30 ns, respectively [Jon88], [CJS75].

#### **4.2.1.2 Voltage Measurements**

The arc voltage can be measured with high voltage probes. They provide accurate results and they withstand high levels of voltage without breakage. Either a North Star PVM-5 HV probe (1000:1, 100-kV peak pulse) or a Tektronix P6015A HV probe (1000:1, 40-kV peak pulse) is inserted in parallel with the WGSG to measure high voltage. Furthermore, a Tektronix P6015A HV probe (1000:1, 40-kV peak pulse) is inserted in parallel with the SBSG. The nominal bandwidth of these probes is approximately 75 to 80 MHz.

## 4.2.2 Errors and uncertainty

Errors and uncertainties undermine the measurement accuracy and appear due to the following factors [Bel99]:

- i. Measuring instrument condition (bias, ageing etc)
- ii. Item being measured (e.g. not stable item to be measured)
- iii. Measurement process difficulties
- iv. Calibration uncertainties
- v. Operator skill or reaction time
- vi. Sampling issues (the measurements should be representative of the processes measured)
- vii. Environment (temperature, pressure, humidity etc)

These and other sources of uncertainties contribute to the overall accuracy of the measurements. The most critical ones for the measurements presented in the thesis are the sampling rate and the bandwidth which are discussed further in the following subchapter.

### 4.2.2.1 Measurement circuitry rise time and sampling rate

Measuring short duration transient events (ns to  $\mu$ s duration), like short duration transient arc discharge, poses many challenges with most important the capability of the measuring system to capture adequately the fast-changing phenomena. This capability is governed by the rise time/bandwidth of the equipment as well as the sampling rate of the oscilloscope used for capturing the waveforms.

The bandwidth,  $BW$ , defines the lower and the highest cut-off frequency at which the measured signal attenuates 3 dB (the captured signal is 70 % of the original one). The rise time,  $\tau_r$ , can be calculated using Equation (4.1).

$$\tau_r = \frac{0.35}{BW} \quad (4.1)$$

As a rule of thumb, the rise time of the measuring equipment should be 3 to 5 times higher than the rise time of the signal to be measured. The equipment used in the tests and the rise time/bandwidth characteristics are summarised in Table 4.1. The bandwidth values have been provided by the manufacturers, except from the shunts, which bandwidth values have been estimated analytically. The smallest bandwidth value (75 MHz) with the highest

response time ( $\sim 5$  ns) is reported for the Tektronix high voltage probe. Hence, acquisition of arc characteristics related to higher frequencies is limited by the smallest bandwidth value of the equipment.

**Table 4.1** Test equipment rise time and bandwidth

No	Equipment	Bandwidth (MHz)	Time rise (ns)
1	Tektronix oscilloscope (sampling rate 2 GS/s)	200	1.75
2	Lecroy oscilloscope (sampling rate 10 GS/s)	1000	0.35
3	Tektronix high voltage probe	75	4.7
4	North Star high voltage probe	80	4.4
5	Custom-built current shunt	100	3.5
6	Samtech tubular current shunt	97.2	3.6
7	Flexible coaxial cable RG 58	4000	0.088
8	Semi-rigid coaxial cable RG 402	20000	0.018
9	Attenuators 20 dB	3000	0.117

According to the Nyquist sampling theorem, the sampling rate should be higher than the double of the signal bandwidth. The bandwidth of the signal to be measured is limited by the instrument bandwidth (for Tektronix Probe  $BW = 75$  MHz). The sampling rate 2 GS/s and 10 GS/s of the oscilloscopes satisfy the Nyquist criterion.

### 4.3 Preliminary tests and simulations

A series of preliminary tests and simulations have been performed to:

- Verify the propagation delay of the cables used to transmit the signals to the receiver (oscilloscope).
- Define the value of the input impedance of the scope to achieve impedance matching with the source impedance to minimise signal reflections.
- Determine whether the probes location within the electrical circuit has an effect on the measured quantities.

### 4.3.1 Tests

#### 4.3.1.1 Propagation delay of the cables

Since the voltage and current waveforms of the electrical arc discharge need to be acquired simultaneously, it is important to determine that the propagation delay of the cables (of the HV probe and the current shunt) that transmit the signals to the receiver does not shift the waveforms relative to each other. Matching the propagation delay of the cables is achieved by amending the cable length of the current shunt.

An avalanche pulse generator (built within the High Voltage group, Electronic and Electrical Engineering Department) have been utilised to define the propagation delay of the cables. The typical equivalent circuit of the avalanche pulse generator is shown in Figure 4.9. The configuration of the circuit consists of a bipolar junction transistor (BJT), resistors,  $R_1$  to  $R_7$ , capacitors,  $C_1$  and  $C_2$ , input voltage,  $V_{in}$ , trigger source,  $V_{trig}$ , common collector voltage,  $V_{cc}$ , and output voltage,  $V_{out}$ . Figure 4.10 shows the avalanche pulse waveform with rise time (from 10 % to 90 %) of 1 to 2 ns and pulse duration (time interval between the 50 % points) of  $\sim 100$  ns.

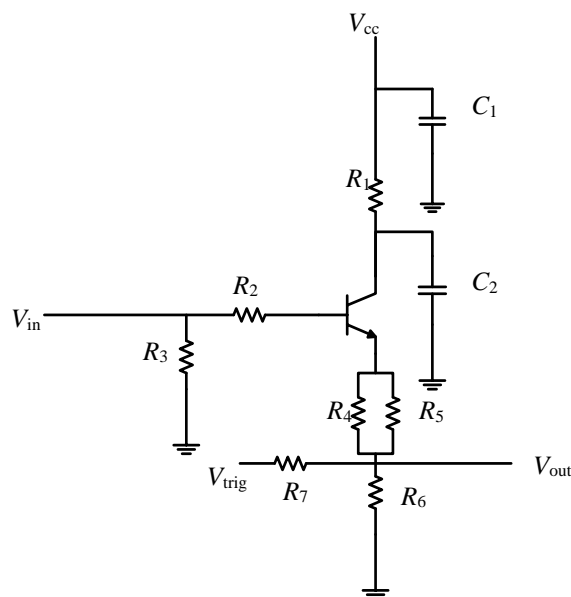


**Figure 4.9** Typical equivalent circuit of the avalanche pulse generator.



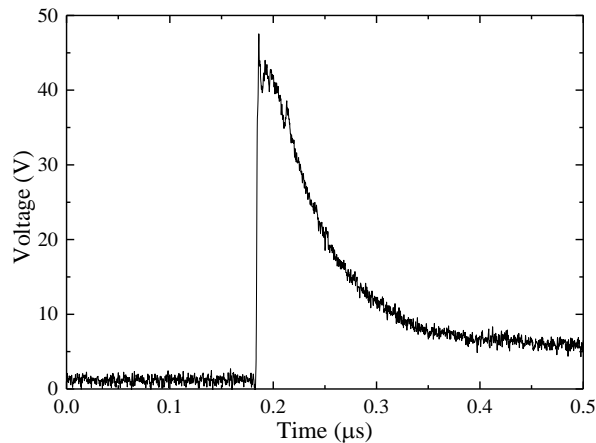


**Figure 4.10.** Typical avalanche pulse waveform.

The avalanche pulse generator was inserted in series with the spark gap in the SBSG topology as shown in the photograph of the set-up in Figure 4.11. Two DC voltage sources of 30 V each, connected in series, supplied the required voltage input to generate the avalanche pulse.

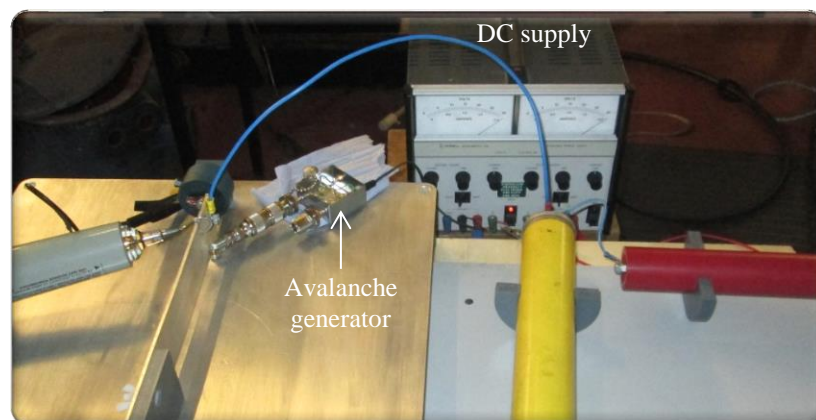


**Figure 4.11** The set-up used to determine the time delay of the cables.

Figure 4.12 shows the acquired waveforms pre- and post-amendment in the current shunt cable length for the SBSG topology. The waveform obtained with the HV probe is given with the dashed line and is considered the reference waveform (since no alteration can be made in its cable). The blue solid line shows the original waveform obtained with the current shunt (through a semi-rigid coaxial cable RG-402 and a RG-58 coaxial cable of total length  $\sim 3$  m). Subsequent amendment in the length of the current shunt cable resulted in shifting the waveform relative to the reference waveform, as measured and shown in Figure 4.12 with a

black solid line. The latter waveform is time-aligned with the reference waveform. The time delay ( $\sim 500$  ps) inserted in the system by the two 20 dB, 50-ohm attenuators (40 dB total) was considered in the calculations.

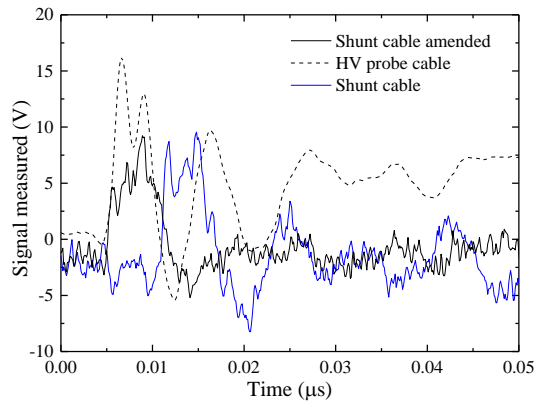


**Figure 4.12** Time delay test results for the SBSG topology; the reference waveform acquired with the HV probe is given with the dashed line, the aligned and non-aligned waveforms with respect to the reference acquired with the current shunt are presented with black and blue solid lines, respectively.

## 4.3.2 PSpice simulations

### 4.3.2.1 Scope input impedance

Propagation delay of the cables is important when acquiring simultaneously waveforms. A further and equally important consideration is to define the value of the input impedance of the scope to achieve impedance matching with the source impedance to minimise signal reflections. Using PSpice software, a lumped circuit model was built to represent the part of the circuit located between the voltage-dividing current shunt and the oscilloscope. Figure 4.13 shows the PSpice model with the current shunt, the coaxial cable, 50-ohm attenuators (40 dB total), the 50-ohm external impedance, the impedance of the channel of the oscilloscope ( $1\text{ M}\Omega$  resistance and typically  $15\text{ pF}$  capacitance). An AC test signal with 200 V amplitude and 10 MHz frequency was sent through the current shunt and received by the oscilloscope.

There are oscilloscopes which provide an option to select the input impedance of the channel (typically  $1\text{ M}\Omega$  or  $50\ \Omega$ ), and there is no need of use of the external impedance.

For simplification, the RG 402 semi-rigid coaxial cable was neglected from the model, and the normal flexible RG-58/U coaxial cable was modelled as an ideal cable with no losses.

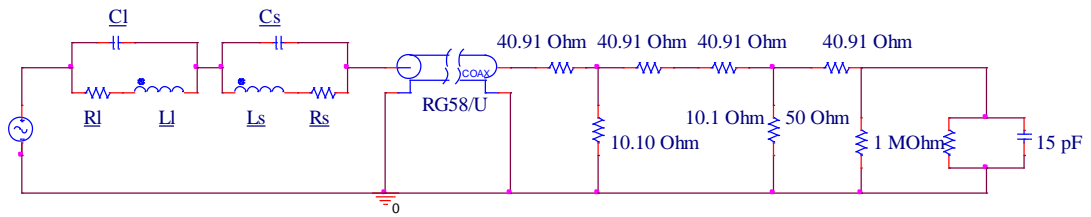


**Figure 4.13** PSpice model of the voltage-dividing current shunt, coaxial cable, 40 dB attenuators, 50  $\Omega$  external impedance and impedance of the channel of the scope.

The custom-made voltage-dividing current shunt, which is electrically inserted in the circuit, does not distort the original signal. Before and after the coaxial cable, waveforms are identical since the coaxial cable is modelled as ideal with no losses, Figure 4.14. The signal received in the scope is also shown in Figure 4.14. The voltage registered by the scope is  $\sim 100$  times lower than the voltage generated by the source since there is 40 dB attenuation inserted in the channel input. No further distortion in the original waveform is introduced since impedance matching was achieved.

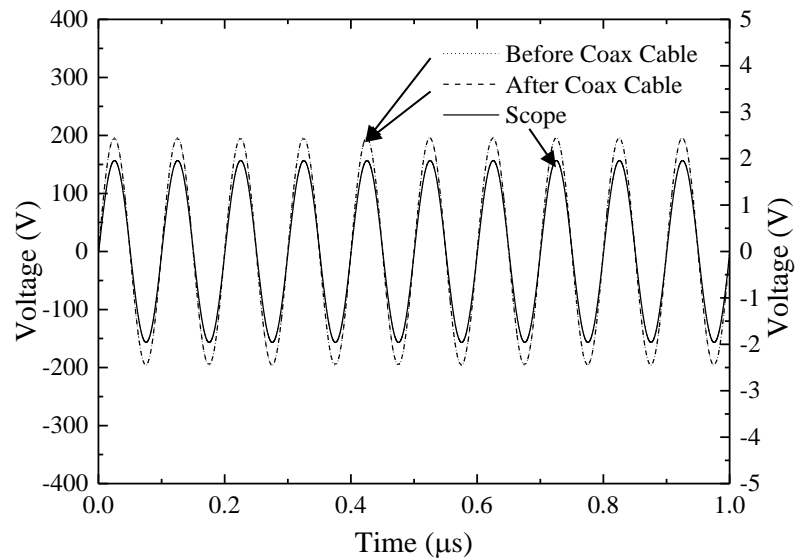


**Figure 4.14** Scope waveform and waveforms at locations before and after the coaxial cable that show impedance matching was achieved (right-hand axis corresponds to the scope waveform). Waveforms before and after the coaxial cable coincide.

### 4.3.2.2 Probe location

Probes should be inserted in the proper location within the circuit to allow for accurate acquisition of the current and voltage waveforms. The HV probe has been placed in parallel with the spark gap in both SBSG and WGSG topology. The current shunt, the voltage-dividing and the tubular shunt, required to be electrically inserted in the circuit loop. Figure 4.15 shows the WGSG topology where two probe locations relative to the earthing point are modelled. The acquired waveforms are shown in Figure 4.16. The waveforms show the voltage drop across the shunt. The location of the shunt relative to the earthing point does not distort the acquired waveforms.

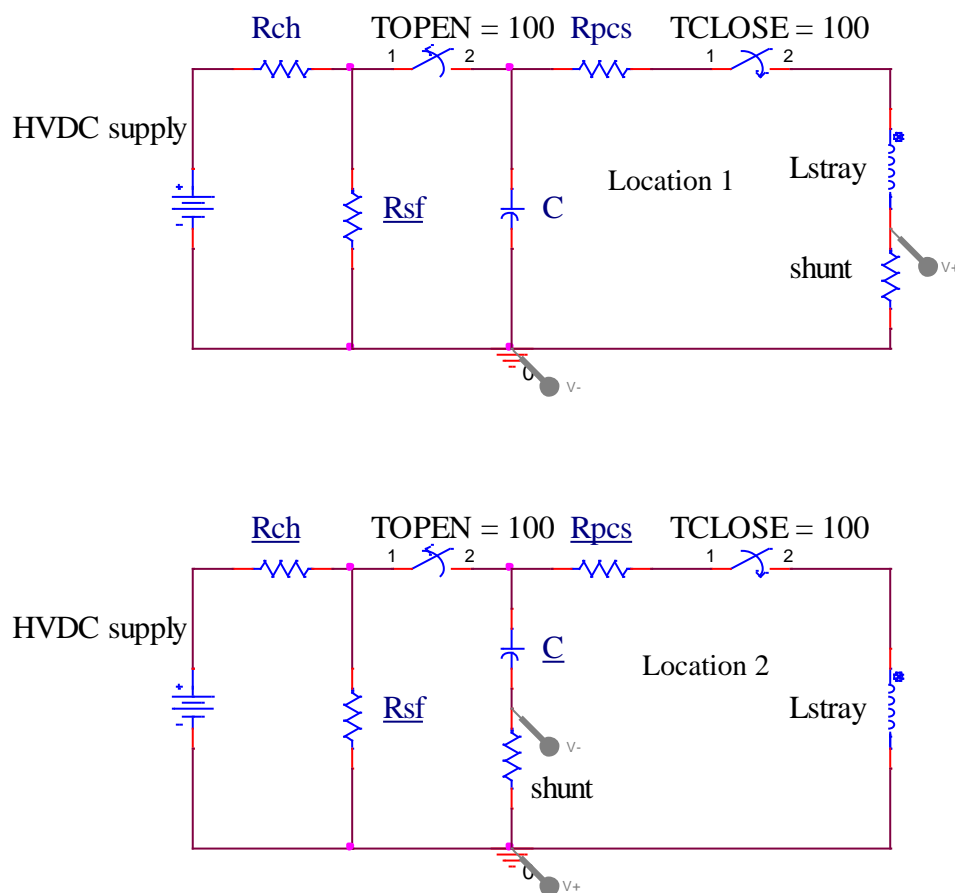


**Figure 4.15** Probe location relative to the earthing point.

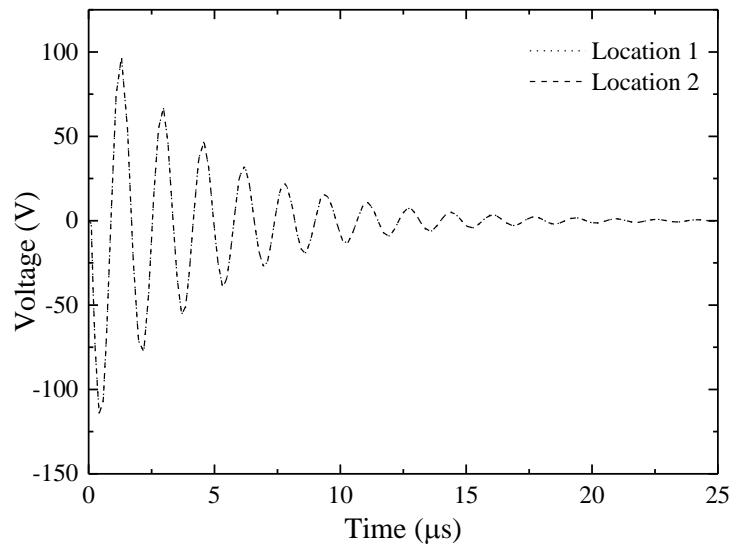


**Figure 4.16** Waveforms acquired with the current shunt located in two different locations within the circuit loop relative to the earthing point. Waveforms of location 1 and location 2 coincide.

## 4.4 Conclusions

The focus of the present study is on investigation of the transient characteristics of electric arcs. Thus, it is important to measure accurately their electrical parameters, voltage across the arc and current through the arc. Proper design of experimental set-up and selection of measuring circuitry is important for accurate acquisition of the electrical characteristics of the arc plasma channel discharge during its initiation phase.

For the scope of the present study, two experimental set-ups with similar topologies have been designed and built and two sets of experimental tests have been conducted. During the first set of tests, spark discharges were created in a self-breakdown spark gap (SBSG), as described in Subchapter 4.1.3. Then, the topology was slightly amended to be used for the second set of tests where discharges were created in a wire-guided spark gap (WGSG), as described in Subchapter 4.1.4. The experimental set-up has been designed and built to meet basic requirements (such as to withstand several discharges without any major destructions taking place) presented in Subchapter 4.1.1.

The developed experimental set-up includes two major novel elements:

- The busbar to point electrode gap topology. The inclusion of a busbar in the experimental topology allows the representation of a topology like an industrial one,

where the busbar location is one of the most likely locations for a severe arc flash incident to occur.

- The voltage-dividing current shunt custom-built to be utilised for the current sensing in the SBSG topology. There was a necessity for developing measuring equipment to fit within the small dimensions of the SBSG topology which simultaneously should withstand the high levels of voltage.

Errors and uncertainties undermine the measurement accuracy and the most critical sources of errors and uncertainties for the measurements presented in the thesis, which are the sampling rate and the bandwidth, have been discussed further in the Subchapter 4.2.2.1.

Finally, a series of preliminary tests and simulations have been performed to validate the suitability of the set-up for subsequent testing, more specifically:

- Verification of the propagation delay of the cables used to transmit the signals to the receiver (oscilloscope).
- Definition of the value of the input impedance of the scope to achieve impedance matching with the source impedance to minimise signal reflections.
- Determination whether the probes location within the electrical circuit influences the measured quantities.

To conclude, the experimental set-up developed is suitable for capturing voltage and current waveforms during the arc initiation. The acquired waveforms will be analysed with the aid of MATLAB/Simulink software in Chapter 5.

## Chapter 5

---

# Arc discharge electrical characteristics

Electrical characteristics of the arc discharge are investigated in Chapter 5. The investigation is focused on the initiation phase of the discharge. During the arc discharge onset, its electrical characteristics are independent of the power supply voltage waveform (AC, DC or impulsive). Moreover, the physical processes during the discharge initiation govern, to a certain degree, the evolution of the phenomenon. Tests were conducted using the SBSG and the WGSg topologies. The arc plasma channel characteristics were obtained from the acquired experimental waveforms and further analysis was performed to obtain the electrical energy deposited at the initial stage of the discharge. These findings are subsequently used in Chapter 6 and Chapter 7 where the energy partition model and prediction of the arc-circuit interaction using the black-box model approach are presented.

## 5.1 Waveforms acquisition

### 5.1.1 Procedure

Current and voltage sensing techniques used to capture the electrical characteristics of the arc discharge have been discussed in Subchapter 4.2.1. The following procedure was established for acquiring the waveforms:

- Capacitor is charged through the charging resistor
- For the SBSG topology: Voltage across the capacitor rises until breakdown occurs in the system spark gap
- For the WGSg topology: After the PCS closure, the capacitor is discharged through the arc plasma channel formed by the exploding wire

- Waveforms are captured using the current shunt and high voltage probe.

Thereafter, the analysis is conducted to extract the accurate arc plasma channel voltage and current with the aid of lumped element circuit theory.

### 5.1.2 Lumped element model (LEM)

An electrical circuit can be modelled following the lumped element circuit theory. This representation simplifies the behaviour of spatially distributed electrical systems into a topology consisting of lumped elements. LEM approach was followed for both the SBSG and the WGSg topology.

- **Cables** and **(copper) braids** are represented with an inductive element in series with a resistive element.
- The **capacitor** is represented with a capacitive element in parallel with a resistive element, and this parallel combination is in series with a combination of stray inductive and resistive elements.
- The **voltage-dividing current shunt** (used in the SBSG topology) is represented with a resistive element in series with an inductive element and their combination in parallel with a capacitive element. One such combination represents the current limiting resistance and one the current sensing resistor.
- The **tubular current shunt** (used in the WGSg topology) is represented with a resistive element since it is considered as non-inductive.
- The **busbar electrode** is represented with an inductive element in series with a resistive element.
- The **ground electrode** is represented with an inductive element in series with a resistive element.

The arc plasma discharge has non-linear characteristics which have been studied by several researchers. There are several models which can be used to describe the arc plasma channel behaviour (arc resistance, power dissipated in the arc, current and voltage waveforms) as a part of a circuit [Bro55]. These models vary between transient and constant models, taking into account the temporal development of the electrical characteristics or not, respectively. Moreover, there are models that describe the arc plasma channel discharge based on a microscale analysis, defining all the physical processes taking place during the phenomenon.



On the other hand, there are models that describe the arc plasma channel discharge on a macroscale basis, considering the arc plasma channel discharge as a black-box with input and output parameters only of interest.

For the scope of the lumped element representation, the arc plasma channel is considered as a time-independent passive circuit element with linear characteristics.

- The **arc plasma channel** is modelled as a combination of resistive and inductive elements in series and a stray capacitive element in parallel. An ideal plasma closing switch represents the discharge initiation. It is assumed that the dominant part is the resistive one, thus, its inductive and capacitive nature is neglected in the subsequent calculations.
- The **plasma closing switch** (used in the WSG topology) is modelled as a combination of resistive and inductive elements in series and a stray capacitive element in parallel. An ideal plasma closing switch represents the discharge initiation. It is assumed that the dominant component of its impedance is the resistive one, thus, its inductive and capacitive nature of the switch impedance is neglected in the subsequent calculations.

Detailed lumped element models for the SBSG and WSG topologies are given in Subchapter 5.1.2.1 and Subchapter 5.1.2.2, respectively.

### 5.1.2.1 LEM - SBSG topology

Figure 5.1 presents the LEM for the SBSG topology which consists of:

- **Capacitor:** capacitive,  $C_{ca}$ , resistive,  $R_{ca}$  and  $R_{cb}$ , and inductive,  $L_{ca}$ , elements.
- **(Copper) braids:** resistive,  $R_{b1}$ ,  $R_{b2}$  and  $R_{b3}$ , and inductive,  $L_{b1}$ ,  $L_{b2}$  and  $L_{b3}$  elements, corresponding to three braids, respectively.
- **Busbar:** resistive,  $R_b$ , and inductive,  $L_b$  elements.
- **Arc plasma channel:** resistive,  $R_{arc}$ , inductive,  $L_{arc}$ , and capacitive,  $C_{arc}$ , elements. An ideal plasma closing switch,  $T_{arc}$ , represents the discharge initiation.
- **Electrode:** resistive,  $R_e$ , and inductive,  $L_e$  elements.
- **Voltage-dividing current shunt:** resistive,  $R_l$ ,  $R_{clb}$ ,  $R_{cla}$ ,  $R_s$ ,  $R_{csb}$ , and  $R_{csa}$ , inductive,  $L_l$ ,  $L_{cla}$ ,  $L_s$  and  $L_{csa}$ , and capacitive,  $C_l$  and  $C_s$ , elements, corresponding to current limiting resistance and the current sensing resistor, respectively.

Since the arc discharge is a transient phenomenon, the circuit inductance plays a significant role in the transient process. Efforts have been made to keep the circuit loop inductance at a minimum value. Thus, during the design phase, the dimensions of the elements comprising the circuit were kept as small as possible. Mainly, efforts were focused on keeping the cables and (copper) braids as short as possible.

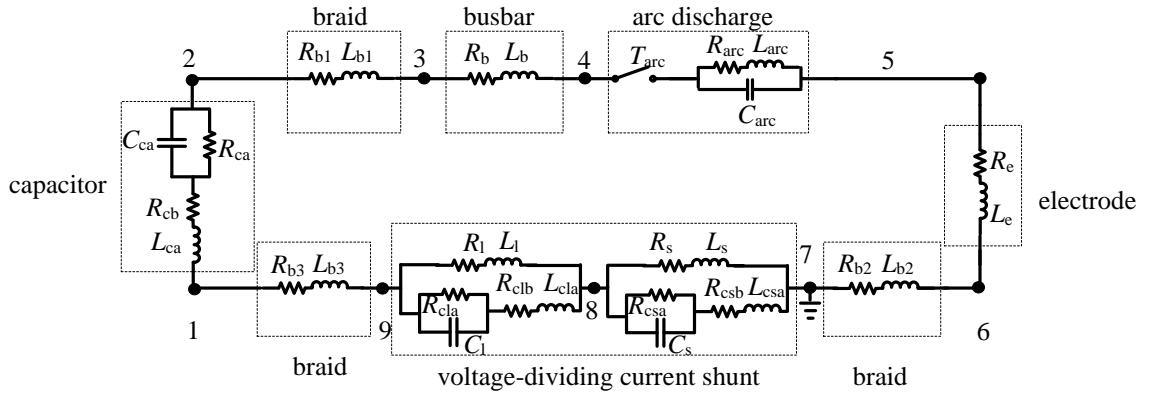


Figure 5.1 LEM for the SBSG topology.

Table 5.1 presents approximate lengths of each component utilised in the SBSG circuit.

Table 5.1 Approximate lengths of the circuit components for the SBSG topology.

Node to node	Element description	Length (cm)
1 to 2	Capacitor	6
2 to 3	Copper braid connecting capacitor with busbar	2
3 to 4	Busbar	3.5
4 to 5	Arc plasma channel	0.01 to 0.1
5 to 6	Point electrode	1
6 to 7	Copper braid connecting electrode with earth	10
7 to 8	Current sensing resistor	1.5
8 to 9	Current limiting resistor	0.5
9 to 1	Copper braid connecting limiting resistor with capacitor	3

**Total : 27.6 cm**

The total length of the circuit loop was measured and found to be ~280 mm. The total inductance of the circuit loop was calculated using the empirical value of the inductance per unit length in a circuit [VPR05], this inductance is ~1 nH/mm. The total loop inductance was also measured with the aid of the ESI Video Bridge 2160 and found to be ~280 nH. Another method of calculation of the circuit inductance is based on formulas given by F. G. Grover [Gro04] and this analysis is presented in Subchapter 5.1.2.3. Using these equations, the calculated inductance value was found to be ~120 nH.

### 5.1.2.2 LEM - WGSG topology

Figure 5.2 presents the LEM for the WGSG topology which consists of:

- **Capacitor:** capacitive,  $C_{ca}$ , resistive,  $R_{ca}$  and  $R_{cb}$ , and inductive,  $L_{ca}$ , elements.
- **Cables and (copper) braid:** resistive,  $R_{c1}$ ,  $R_{c2}$  and  $R_{b1}$ , and inductive,  $L_{c1}$ ,  $L_{c2}$  and  $L_{b1}$  elements, corresponding to two cables and one braid, respectively.
- **Busbar:** resistive,  $R_b$ , and inductive,  $L_b$  elements.
- **Arc plasma channel:** resistive,  $R_{arc}$ , inductive,  $L_{arc}$ , and capacitive,  $C_{arc}$ , elements. An ideal plasma closing switch,  $T_{arc}$ , represents the discharge initiation.
- **Electrode:** resistive,  $R_e$ , and inductive,  $L_e$  elements.
- **Tubular current shunt:** resistive,  $R_s$ , element.
- **Plasma closing switch:** resistive,  $R_{pcs}$ , inductive,  $L_{pcs}$ , and capacitive,  $C_{pcs}$ , elements. An ideal plasma closing switch,  $T_{pcs}$ , represents the discharge initiation.

Table 5.2 presents approximate lengths of each component of the WGSG topology. The total length of the loop was measured and found to be ~110 cm. The calculated inductance of the loop is 1100 nH or 1.1  $\mu$ H, following the empirical rule of ~1 nH per mm. Using the formulas from [Gro04], the calculated inductance value found to be ~710 nH.

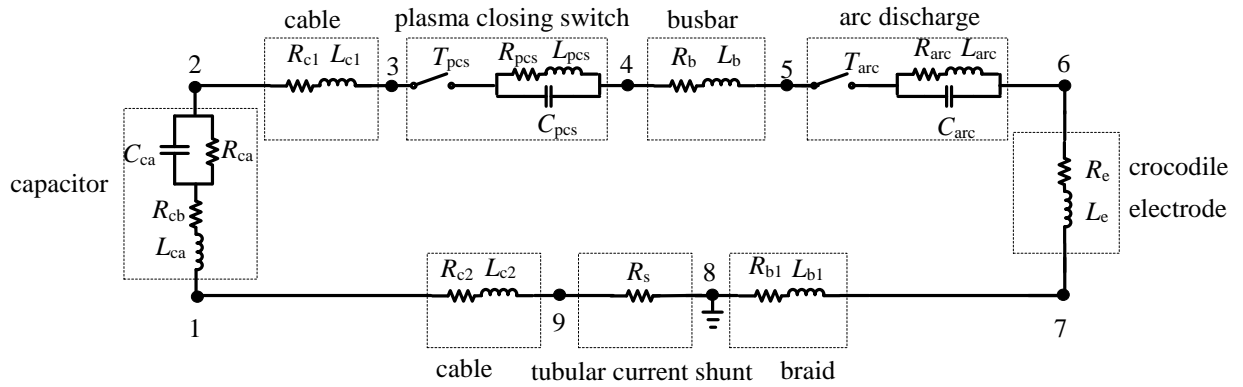


**Figure 5.2** LEM for the WGS topology

**Table 5.2** Approximate circuit components lengths for the WGS topology.

Nodes to node	Element description	Length (cm)
1 to 2	Capacitor	4
2 to 3	Cable connecting capacitor with switch	20
3 to 4	Plasma closing switch	3
4 to 5	Busbar	4
5 to 6	Arc plasma channel	1 to 8
6 to 7	Crocodile electrode	5
7 to 8	Copper braid connecting electrode with earth	20
8 to 9	Tubular current shunt	16
9 to 1	Cable connecting shunt with capacitor	30

**Total : 110 cm**

### 5.1.2.3 Inductance, resistance and capacitance calculations

#### *Inductance calculations*

Maxwell's equations can be used to calculate the inductance of an element. However, simplifications can be made and closed form of equations can be produced for calculating of inductance values. Both, self-inductance and mutual inductance calculations are important when analysing transient electrical behaviour of circuits. Formulas from [Gro04] can be used to calculate the self-inductance of the electrical circuit elements, Equation (5.1) and

Equation (5.2). The inductance value in Equation (5.1) and Equation (5.2) depends on the geometrical characteristics of the conducting circuit elements. Also, the mutual inductances of the circuit elements were calculated using formulas from [Gro04]. However, they were neglected in the subsequent calculations since their values were very small as compared with the self-inductance values.

○ *Inductance of an individual wire with rectangular cross section*

$$L = 0.002l_w[\log_e \frac{2l_w}{d_1+d_2} + \frac{1}{2} - \log_e e] \quad (5.1)$$

○ *Inductance of individual wire with circular cross section*

$$L = 0.002l_w[\log_e \frac{2l_w}{r_w} - \frac{3}{4}] \quad (5.2)$$

where:

$L$  : inductance [ $\mu\text{H}$ ]

$l_w$  : length of the wire [cm]

$d_1, d_2$  : edge lengths of the rectangular cross section [cm]

$r_w$  : wire cross section radius [cm]

$\log_e e$  : constant value obtained from Table 5.3 for the given value of  $d_1/d_2$  [ $\mu\text{H}/\text{cm}$ ]

**Table 5.3**  $\log_e e$  values for each of the ratio values of the sides  $d_1$  and  $d_2$  of the cross section [Gro04].

$d_1/d_2$ or $d_2/d_1$	$\log_e e$ [ $\mu\text{H}/\text{cm}$ ]	$d_1/d_2$ or $d_2/d_1$	$\log_e e$ [ $\mu\text{H}/\text{cm}$ ]
0	0.00211	0.25	0.00181
0.025	0.00203	0.30	0.00179
0.05	0.00197	0.35	0.00178
0.10	0.00192	0.40	0.00177
0.15	0.00187	0.45	0.00177
0.20	0.00184		

### *Resistance calculations*

Equation (5.3) can be used to calculate the (stray) resistance of a circuit element. The resistance value in the formula depends on the resistivity value and the geometrical characteristics (length and cross-sectional area) of the element. When calculating resistance values, especially in electronic circuits, the temperature dependence of the resistivity of conductor should be also considered, as it can often result in a change in the resistance value. However, for the purposes of the present study, it is assumed that the impact of the temperature in the resistance is negligible.

#### ○ *Resistance of wire with rectangular or circular cross section*

$$R = \frac{l_w}{\sigma A} \quad (5.3)$$

where:

$R$  : resistance [ $\Omega$ ]

$\sigma$  : electrical conductivity [ $1/\Omega/m$ ]

$l_w$  : length [m]

$A$  : cross sectional area [ $m^2$ ]

### *Capacitance calculations*

Capacitance was not calculated in this study since the values of the capacitors utilised in the experiments were taken from their manufacturers' datasheet. Stray capacitance should also be considered, especially in the case of high frequencies, since its value might affect the electrical behaviour of the circuits. However, it is difficult to estimate the stray capacitances in the experimental geometry. Given the size of the energy storage capacitors used in the study, it is reasonable to ignore the stray capacitances.

## **5.2 Resistive and inductive voltage drops: Separation methodology**

As was mentioned in Subchapter 4.2.1, identifying electrical characteristics of the arc plasma discharge can be quite challenging, since it involves high current and high voltage

measurements. The event of an arc discharge initiates and evolves very fast, where high  $dV/dt$  (up to  $\sim 10^{12}$  V/s) and  $dI/dt$  (up to  $\sim 10^7$  A/s) are expected. These high rates of voltage and current change over the time can distort the acquired waveforms. Thus, a measuring system with the suitable response time/bandwidth and sampling rate should be utilised for the measurements.

The high rate of current change ( $dI/dt$ ) may result in significant inductive voltage drop across the stray inductances in the experimental topology. Thus, it is crucial to separate the resistive and inductive components in the obtained experimental voltage waveforms in order to extract the accurate resistive and power characteristics of the arc.

The voltage,  $V_m$ , measured across the circuit element with an inductive and resistive nature, shown in Figure 5.3, is the summation of its resistive,  $V_L$ , and inductive,  $V_R$ , voltage drops, Equation (5.4). Based on this fundamental circuit theory, the procedure was developed and followed for extracting the arc voltage and current which are going to be presented analytically in Subchapter 5.3.

$$V_m = V_L + V_R \quad (5.4)$$

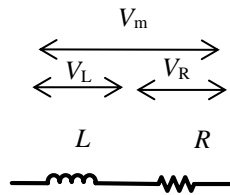


**Figure 5.3** A typical circuit element with resistive and inductive nature.

### 5.3 Arc voltage and current

An HV probe, either a Tektronix P6015A HV probe (1000:1, 40 kV peak pulse) or a North PVM-5 HV probe (1000:1, 100 kV peak pulse), and the digitising oscilloscope Tektronix TDS 2024 with bandwidth of 200 MHz and sampling rate of 2Gs/s (or Lecroy digitising oscilloscope) were used to acquire the voltage waveforms from which the resistive voltage drop across the arc was extracted following an appropriate resistive and inductive voltage dividing methodology.

In the SBSG topology, a voltage-dividing current shunt and digitising oscilloscope Tektronix TDS 2024 with bandwidth of 200 MHz and sampling rate of 2Gs/s were used for the acquisition of the voltage across the shunt required to extract the arc current waveforms

following an appropriate resistive and inductive voltage dividing methodology. In the WGSB topology, a Samtech DE(CP)-01 tubular current shunt (13.96 V/kA) was utilised to acquire the arc current waveforms. Since the tubular shunt is considered as low-inductive element of the circuit, the acquired waveforms were used as the arc waveforms without any further analysis.

### 5.3.1 Arc voltage

#### 5.3.1.1 Arc voltage - SBSG topology

For the SBSG topology, the inductive voltage drop across the stray inductances in the busbar, copper braids and point electrode was taken into consideration. Figure 5.4(a) shows the photo with the location of the HV probe across the spark gap, and Figure 5.4(b) shows its corresponding lumped element representation. Typical acquired voltage waveforms are given in Figure 5.5 for the case of a 0.5 mm gap length and 1.9 nF capacitor. The voltage waveform acquired with the HV probe is given with dashed black line and the voltage waveform acquired with the current shunt is given with the solid black line.

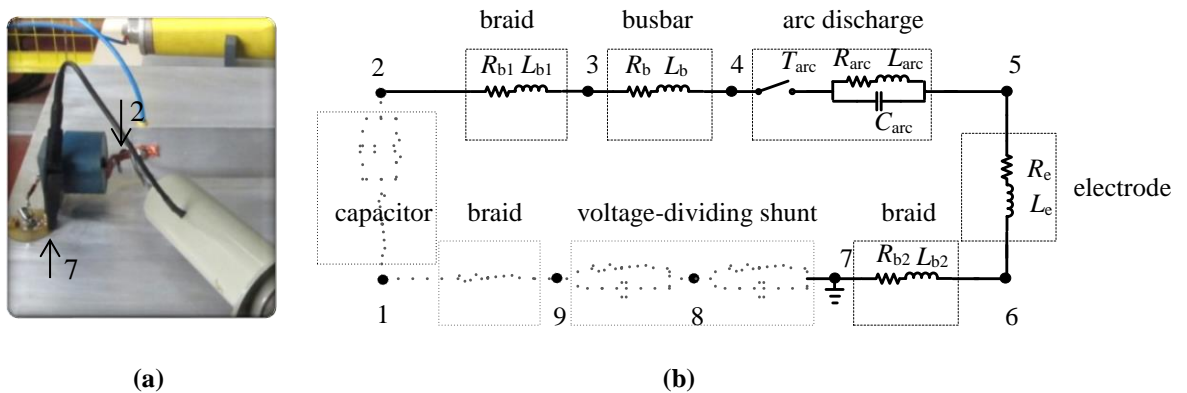


**Figure 5.4** (a) Location of the HV probe across the spark gap and (b) the corresponding lumped element representation of the spark gap; 2 and 7 in (a) corresponds to points 2 and 7 indicated in (b).



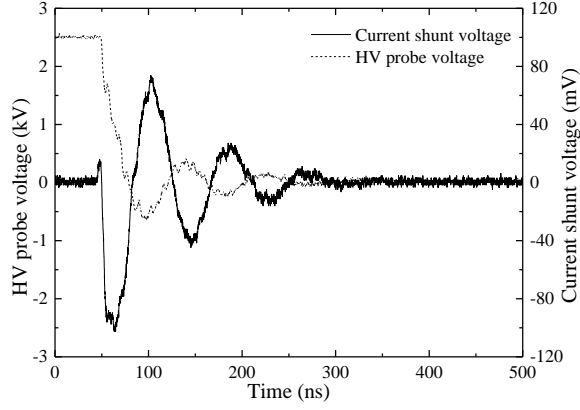


**Figure 5.5** Voltage waveforms for 0.5 mm spark gap length and 1.9 nF capacitor acquired using a current shunt and a HV probe. The voltage of the shunt should be multiplied by the factor of 91.2 to take into account the attenuators added to the scope channel. The arc current is calculated as the solution of the ODE describing the circuit as presented in Subchapter 5.3.1.2.

Equation (5.5) defines the stray inductance,  $L_{\text{stray}}$ , and Equation (5.6) the stray resistance of the spark gap. Their values were calculated using equations (5.1) to (5.3). The value of the stray resistance,  $R_{\text{stray}}$ , was calculated 0.3 m $\Omega$ , thus, it can be neglected in the subsequent calculations.

$$L_{\text{stray}} = L_{b1} + L_b + L_e + L_{b2} \approx 100 \text{ nH} \quad (5.5)$$

$$R_{\text{stray}} = R_{b1} + R_b + R_e + R_{b2} \approx 0.3 \text{ m}\Omega \text{ (can be neglected)} \quad (5.6)$$

The arc plasma channel is considered to be purely resistive channel (this assumption was discussed initially in Subchapter 5.1.2). Thus, the inductive part of the impedance of the arc plasma channel is negligible,  $L_{\text{arc}} \sim 0$  nH, the capacitive part of the impedance of the arc plasma channel is also negligible,  $C_{\text{arc}} \sim 0$  nF and the capacitive leakage current is  $I_{\text{carc}} \sim 0$  A. Kirchhoff's voltage law, as presented in Equation (5.7), is used to extract the arc plasma channel voltage. Figure 5.6 shows the measured (dashed line) and the extracted (solid line) voltage waveforms.

$$V_{\text{arc}}(t) = V_{\text{probe}}(t) - L_{\text{stray}} \frac{dI_{\text{arc}}(t)}{dt} \quad (5.7)$$

where:

$V_{\text{arc}}(t)$  : arc plasma channel voltage [V]

$V_{\text{probe}}(t)$  : experimental acquired data from the HV probe [V]

$I_{\text{arc}}(t)$  : arc plasma channel current [A]

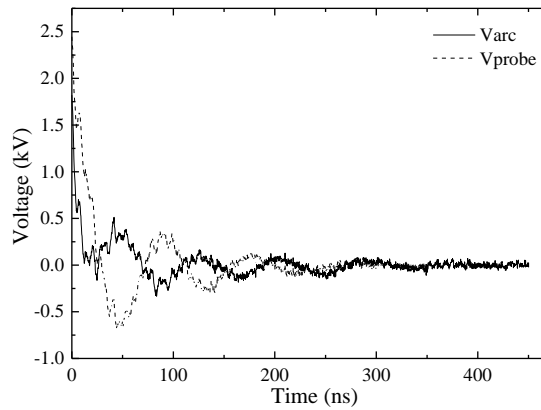


**Figure 5.6** The measured voltage waveform (dashed line) and the extracted arc plasma channel voltage waveform (solid line) for 0.5 mm spark gap and 1.9 nF capacitor.

The calculated arc voltage presents a phase shift and a different magnitude compared to the acquired voltage waveform. This is the result of the separation of the inductive and resistive voltage parts of the acquired waveforms.

### 5.3.1.2 Arc voltage - WBSG topology

For the WBSG topology, the inductive voltage drop across the stray inductances in the busbar, copper braid and the crocodile electrode was taken into consideration. Figure 5.7(a) shows the photo with the location of the HV probe across the spark gap and the PCS and Figure 5.7(b) shows its corresponding lumped element representation.

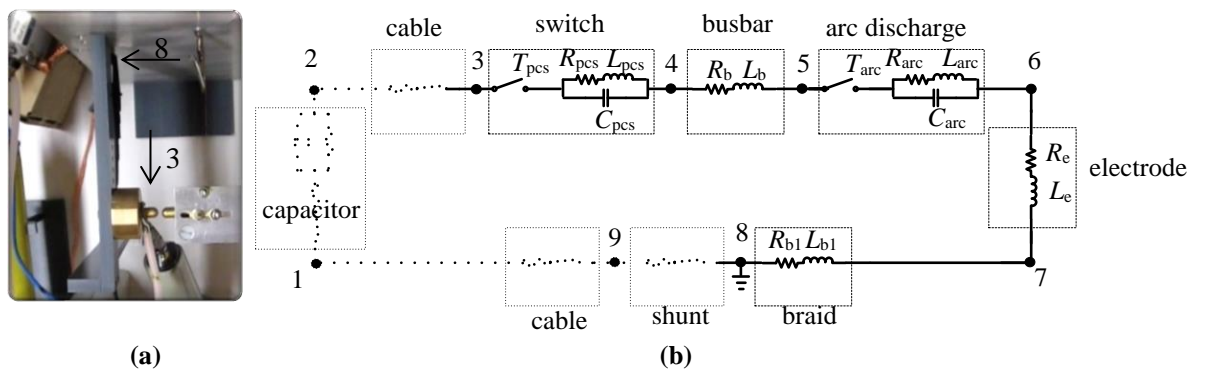


**Figure 5.7** (a) Location of the HV probe across the spark gap and (b) the corresponding lumped element representation of the spark gap; 3 and 8 in (a) corresponds to points 3 and 8 indicated in (b).

Typical voltage waveforms for a 3 cm spark gap length and 80 nF capacitor are given in Figure 5.8. The voltage waveform acquired with the HV probe is given with dashed black line and the voltage waveform acquired with the current shunt is given with the solid black line. Analysis of the waveforms reveals several stages of the wire-guided breakdown process. During the first  $\sim 0.5 \mu\text{s}$ , the PCS closes and causes the rapid collapse of the voltage and increase in the current through the copper wire. At  $\sim 0.5 \mu\text{s}$ , the wire evaporates, resulting in interruption of the initial conducting path. The WSGS opens, leading to the collapse of the current and a sharp increase in the voltage across the WSGS. The initial conducting path is interrupted for  $\sim 1.5 \mu\text{s}$  (this is the time interval during which the WSGS remains open and a stabilised voltage is established across the gap's terminals, and varies stochastically between sparks), after which breakdown of the gap takes place, and the current starts to oscillate in the circuit. After breakdown, the current waveform is described by an exponentially-damped sinusoidal function.

The rapid collapse of the voltage and increase in the current, when the PCS closes, happens at the same time showing a good alignment in their waveforms. However, during the WSGS breakdown, a time delay between the current increase and the voltage collapse is observed. This can be attributed to the small capacitance of the WSGS. Thus, once the voltage starts to collapse, a very small change on the current is observed. The current starts to increase with a noticeable time delay compared to the voltage collapse.

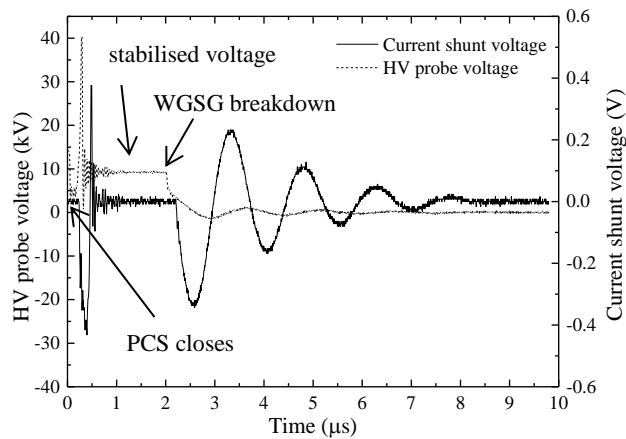


**Figure 5.8** Current and voltage acquired waveforms for a 3 cm gap length and 80 nF capacitor. The arc current waveform is obtained directly from the tubular current shunt utilising its division ratio 13.96 V/kA and using the 91.2 multiplication factor to account for the attenuators inserted in the scope channel.

Equation (5.8) presents the stray inductance, and Equation (5.9) and Equation (5.10) present the stray resistance and the total resistance of the loop,  $R_{\text{total}}$ , which includes the stray resistance and the resistance of the PCS. Equations (5.1) to (5.3) were used to calculate the stray inductance of the loop. The value of the total resistance was found to be  $\sim 0.3 \Omega$ , and its analytical calculation is presented in Appendix B.

$$L_{\text{stray}} = L_b + L_e + L_{b1} \approx 230 \text{ nH} \quad (5.8)$$

$$R_{\text{stray}} = R_b + R_e + R_{b1} \approx 0 \Omega \quad (5.9)$$

$$R_{\text{total}} = R_{\text{pcs}} + R_{\text{stray}} \approx 0.3 \Omega \quad (5.10)$$

Kirchhoff's voltage law, as presented in Equation (5.11) and Equation (5.12), was used to extract the arc plasma channel voltage. Figure 5.9 shows the measured (dashed line) and the extracted (solid line) voltage waveforms.

$$V_{\text{arc}}(t) = V_{\text{probe}}(t) - V_{\text{pcs}}(t) \quad (5.11)$$

$$V_{\text{arc}}(t) = V_{\text{probe}}(t) - V_{\text{spark}} - L_{\text{stray}} \frac{dI_{\text{arc}}(t)}{dt} \quad (5.12)$$

where:

$V_{\text{pcs}}(t)$  : voltage across the spark discharge in PCS and across the stray resistance of the remaining circuit [V]

$V_{\text{spark}}$  : spark discharge voltage of the PCS [V]

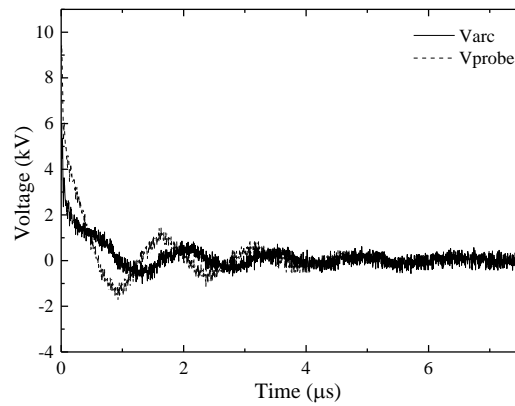


**Figure 5.9** The measured voltage waveform (dashed line) and the extracted arc plasma channel voltage waveform (solid line) for 3 cm spark gap and 80 nF capacitor.

The extracted arc voltage presents a phase shift and a different magnitude in comparison with the acquired voltage waveform. This is the result of the separation of the inductive and resistive voltage parts of the acquired waveforms.

## 5.3.2 Arc current

### 5.3.2.1 Arc current - SBSG topology

The voltage waveform acquired with the voltage-dividing current shunt, typical curve given in Figure 5.5 with black solid line, is used to extract the arc plasma channel current. Figure 5.10 shows the current sensing resistor (with the stray inductance) across which the voltage across the current shunt,  $V_s$ , is measured. The leakage current through the compensating capacitor can be neglected since it is a very small proportion of the total arc plasma channel current. For instance, for the case of 0.5 mm spark gap and 1.9 nF, the capacitive current of the current shunt,  $I_{Cs}$ , was calculated  $\sim 0.7$  A ( $\sim 0.4\%$  of the arc current).

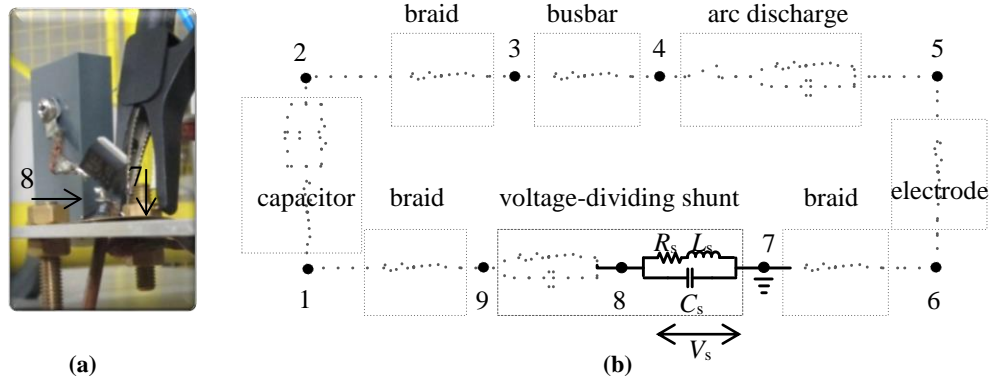


**Figure 5.10** (a) Location of the current sensing resistor with the compensating capacitor in parallel and (b) the corresponding lumped element representation; 7 and 8 in (a) corresponds to points 7 and 8 indicated in (b).

Following the methodology described in Chapter 5.2, Equation (5.13) is formed and used to obtain the arc current waveform. The current sensing resistor has a resistance value,  $R_s = 25 \text{ m}\Omega$  and a low inductance value,  $L_s = 0.7 \text{ nH}$ . An exponentially damped equation is fitted in the measured voltage values and the first order differential equation formed, Equation (5.14), is solved obtaining the arc current waveform,  $I_{\text{arc}}$ , with the aid of MATLAB. Appendix C presents an example of obtaining the arc current waveform for the case of  $1.9 \text{ nF}$  and  $0.5 \text{ mm}$  spark gap length. The same procedure was followed for all spark gap distances.

$$V_s(t) = V_{R_s}(t) + V_{L_s}(t) \quad (5.13)$$

$$V_s(t) \approx V_0 \sin(\omega t) e^{-\zeta t} = R_s I_{\text{arc}}(t) + L_s \frac{dI_{\text{arc}}}{dt} \quad (5.14)$$

where:

$V_s(t)$  : shunt voltage [V]

$V_{R_s}(t)$  : resistive part of shunt voltage [V]

$V_{L_s}(t)$  : inductive part of shunt voltage [V]

$V_0$  : voltage constant [V]

$\zeta$  : damping constant [rad/s]

$\omega$  : angular velocity of damped oscillations [rad/s]

### 5.3.2.2 Arc current - WGSF topology

For the WGSF topology, the arc current waveform is obtained directly from the tubular current shunt utilising its division ratio 13.96 V/kA. Thus, Equation (5.15) was used to calculate the arc current,  $I_{\text{arc}}$ , in A for the wire-guided discharges. The value 91.2 was used to take into account the attenuators inserted in the measuring circuitry to protect the oscilloscope.

$$I_{\text{arc}}(t) = 91.2 \cdot V_s(t) \cdot 1000/13.96 \quad (5.15)$$

It is the particular design of the tubular shunt that allows the direct current acquisition. There are several current shunt designs, for example flat strip, squirrel cage etc. The coaxial/tubular current shunt design presented in Figure 5.11(a) is ideal for transient measurements as it provides minimum inductance and hence high level of accuracy in measurements of current since it is considered as a purely resistive shunt.

The simplified diagram in Figure 5.11(b) shows a general shunt measuring circuit with emphasis given to the magnetic coupling between the main electrical circuit and the measuring circuit. To measure current waveform,  $I_{\text{arc}}(t)$ , with the shunt, the voltage drop between the open terminals,  $\psi$  and  $o$ , should be acquired using Equation (5.16). When the inductive terms of the voltage are as small as possible or ideally cancel each other (when  $M_{\psi o} \approx L_{\psi o}$ ),  $V_{\psi o}$  approximates  $I_{\text{arc}}(t) R_{\psi o}$ .

$$V_{\psi o} = I_{\text{arc}} R_{\psi o} + L_{\psi o} \frac{dI_{\text{arc}}}{dt} - M_{\psi o} \frac{dI_{\text{arc}}}{dt} \quad (5.16)$$

where:

$R_{\psi o}$  : resistance [ $\Omega$ ]

$L_{\psi o}$  : self-inductance of the main electrical circuit [H]

$M_{\psi o}$  : mutual inductance of the measuring circuit [H]

The same principle of operation is followed for a tubular current shunt. The tubular shunt is built with two cylinders, one inside the other. The outer cylinder is earthed to block any external field penetrations to the inside resistive cylinder. The voltage across  $\psi o$

approximates  $I_{\text{arc}}(t)R_{\Psi O}$ , since the induced voltage in  $\Psi'O'$  is approximately equal to the inductive voltage in the  $\Psi O$  (when  $M_{\Psi'O'} \approx L_{\Psi O}$ ).

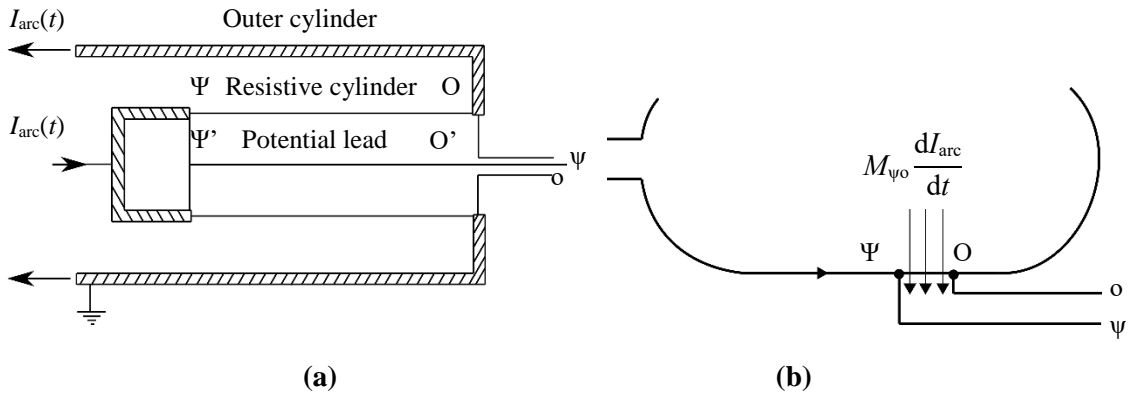


**Figure 5.11** (a) Schematic cross-section of a coaxial current shunt [Jon88] (b) Magnetic coupling in a shunt measuring circuit.

## 5.4 Methodology to determine the arc discharge resistance

William Greason developed a technique to measure the resistance of a spark discharge between two spherical electrodes using the measured discharge currents for underdamped and forced overdamped cases [Gre99]. In his analysis, the resistance of the spark is considered as a constant. Thus, the discharge circuit can be represented as a series RLC system.

For both the SBSG and WGSg topologies, considering the arc resistance as a time-independent passive circuit element, the circuit can be represented by an RLC circuit with underdamped response. Following the technique described in [Gre99], the equivalent constant resistance,  $R_{\text{eqarc}}$ , has been obtained using the experimental current waveforms for each topology. The term “equivalent constant resistance” refers to the effective resistance of the circuit or element under consideration.

After breakdown (either in the SBSG or in the WGSg topology), the current waveform,  $I_{\text{arc}}(t)$ , is described by an exponentially-damped sinusoidal function, equations (5.17) to (5.20):

$$I_{\text{arc}}(t) = I_0 e^{-\zeta t} \sin(\omega t) \quad (5.17)$$

$$I_0 = V_{\text{br}} C \left( \frac{\zeta^2}{\omega} + \omega \right) \quad (5.18)$$



$$\zeta = \frac{R_d}{2L_d} \quad (5.19)$$

$$\omega = \sqrt{\frac{1}{L_d C} - \zeta^2} \quad (5.20)$$

where:

$I_0$  : current constant [A]

$V_{br}$  : breakdown voltage [V]

$L_d$  : discharging circuit inductance [H]

$R_d$  : discharging circuit resistance [ $\Omega$ ]

Figure 5.12(a) and (b) show the current waveforms, for the SBSG and the WGSG topologies respectively, with highlighted points used in the calculations. An average value of the period of oscillations is obtained using 3 individual oscillation periods for the underdamped current, Equation (5.20). The first two peaks of the current waveform,  $I_{arc1}$  and  $I_{arc2}$ , the time they appear,  $t_1$  and  $t_2$ , are defined and used in Equation (5.17),

$$I_{arc1}(t_1) = I_0 e^{-\zeta t_1} \sin(\omega t_1), I_{arc2}(t_2) = I_0 e^{-\zeta t_2} \sin(\omega t_2),$$

along with the angular velocity of the damped oscillations,  $\omega$ . The constant circuit resistance of the loop is derived by dividing  $I_{arc1}(t_1)$  over  $I_{arc2}(t_2)$ , Equation (5.22). The arc resistance is extracted from the constant circuit resistance of the circuit loop by subtracting the stray resistance of the remaining circuit loop, Equation (5.23). This residual loop resistance is different for the SBSG and the WGSG topologies and defined as 1.025  $\Omega$  and 0.3  $\Omega$ , respectively. Table 5.4 presents the results for the two cases described above using equations (5.21) to (5.23).

$$T_{per} = \frac{\sum_{i=1}^3 T_{peri}}{3} \quad (5.21)$$

$$R_d = 2L \frac{\ln(I_1(t_1)/I_2(t_2))}{t_2 - t_1} \quad (5.22)$$

$$R_{eqarc} = R_d - R_{res} \quad (5.23)$$

where:

$T_{peri}$  :  $i$ -th period [s]

$T_{\text{per}}$  : average period [s]

$f$  : frequency [Hz]

$R_{\text{res}}$  : resistance of the residual circuit loop excluding the arc resistance [ $\Omega$ ]

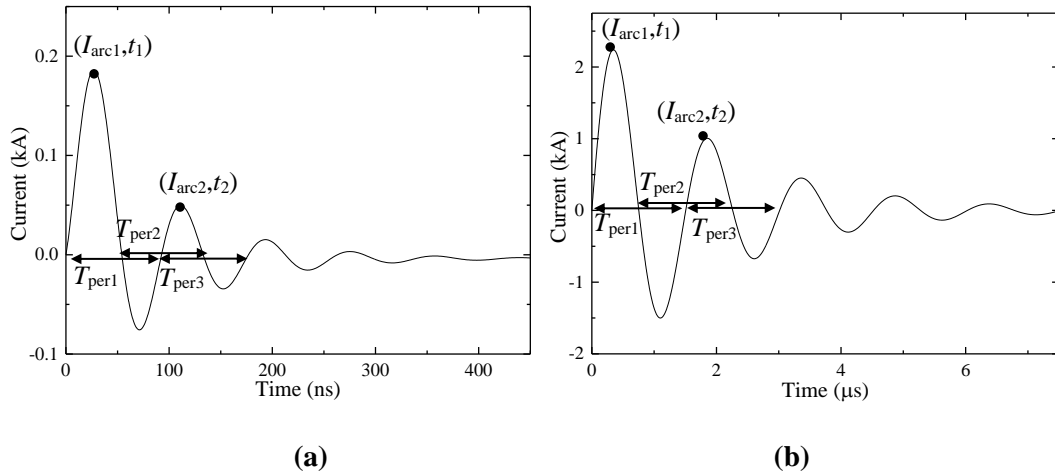


**Figure 5.12** Current waveforms used to calculate the equivalent constant resistance (a) for a SBSG with 0.5 mm spark gap and 1.9 nF capacitor and (b) for a WGSB with a 3 cm spark gap and 80 nF capacitor (waveforms used for illustration purposes only).

**Table 5.4** Equivalent constant resistance results for a single spark measurement across the SBSG and the WGSB.

Variable	SBSG	WGSB
$C$ [nF]	1.9	80
$I_{\text{arc1}}$ [kA]	0.186	2.247
$I_{\text{arc2}}$ [kA]	0.050	1.095
$t_1$ [ $\mu\text{s}$ ]	0.027	0.384
$t_2$ [ $\mu\text{s}$ ]	0.111	1.852
$T_{\text{per}}$ [ $\mu\text{s}$ ]	0.085	1.489
$R_d$ [ $\Omega$ ]	3.033	0.687
$R_{\text{eqarc}}$ [ $\Omega$ ]	<b>2.008</b>	<b>0.385</b>

## 5.5 Experimental results

The results obtained in the present chapter refer to the arc electrical characteristics created in both sub-mm spark gaps and longer spark gaps (several cm) in HV experiments with an oscillatory (AC) current character. In particular, the voltage and current waveforms have been recorded and analysed. Other parameters of interest, such as electric field strength and variation of the field in the area around the arc, could potentially be investigated in future work [Gre99] and [Jon88]. Subchapter 5.5.1 presents the results obtained using the SBSG topology for sub-mm spark gap lengths. Subchapter 5.5.2 presents the results obtained using the WGSG topology for longer spark gap lengths of the order of several cm.

### 5.5.1 SBSG topology

The best fit approach was applied to the obtained experimental data. The linear least squares regression method has been used to summarise the experimental data points. The defined equations are simple mathematical expressions which can be used to predict unobserved values within the limits of the experimental conditions. Furthermore, the models allow establishment of relationships between the variables of interest and identification of mechanisms which underpin the processes taking place.

#### 5.5.1.1 Breakdown voltage

The breakdown voltages for 10 inter-electrode gap lengths and for 4 different capacitor values were acquired (5 individual measurements for each spark gap and each capacitance were conducted). As was expected, since the spark gap is a self-breakdown spark gap, the breakdown voltage should have a strong dependency on the gap length,  $d$ , as observed in Figure 5.13. It has also been verified that the breakdown voltage is independent of the capacitor value. A linear least squares fitting procedure in Origin Pro 9 graphing software was used to fit analytical straight line to all the experimental data points simultaneously. The fitting line obtained is shown as solid line in Figure 5.13, the function is given in Equation (5.24). The 95% prediction intervals are also shown in Figure 5.13. The dashed lines represent the upper and lower 95% prediction intervals.

$$V_{\text{br}}(d) = 1.00 + 3.30d \quad (5.24)$$

where  $V_{br}(d)$  in kV and  $d$  in mm.

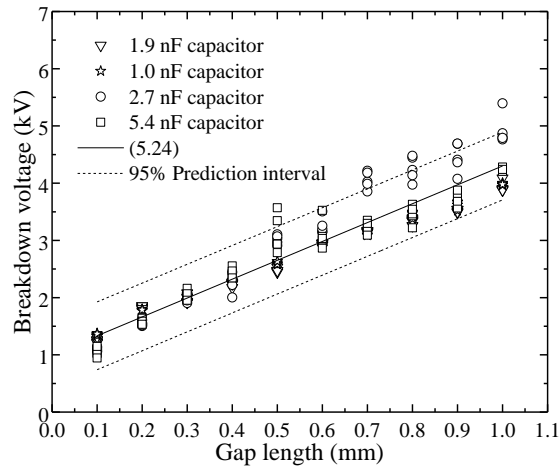


**Figure 5.13** Breakdown voltages for 10 inter-electrode gap lengths and 4 different capacitor values. 5 sparks for each gap length are shown. The solid line gives the best analytical fitting for all data using Equation (5.24). The dashed lines represent the bottom and top 95% prediction intervals.

### 5.5.1.2 Arc current

Following the methodology described in Subchapter 5.3.2.1 the accurate arc current waveforms were obtained and the maximum value of the current in each waveform was measured. Figure 5.14(a) to Figure 5.14(d) presents the experimental data acquired. Equations (5.25) to (5.28) give the analytical fitting curves to experimental data points for each capacitor. The 95% prediction intervals are also shown in Figure 5.14(a) to Figure 5.14(d). The dashed lines represent the bottom and top 95% prediction intervals.

$$\text{for } 5.4 \text{ nF capacitor : } I_{arc}(d) = 136.79 + 333.30d \quad (5.25)$$

$$\text{for } 2.7 \text{ nF capacitor : } I_{arc}(d) = 65.64 + 334.54d \quad (5.26)$$

$$\text{for } 1.9 \text{ nF capacitor : } I_{arc}(d) = 88.47 + 201.28d \quad (5.27)$$

$$\text{for } 1.0 \text{ nF capacitor : } I_{arc}(d) = 49.48 + 112.59d \quad (5.28)$$

where  $I_{arc}(d)$  in A and  $d$  in mm.

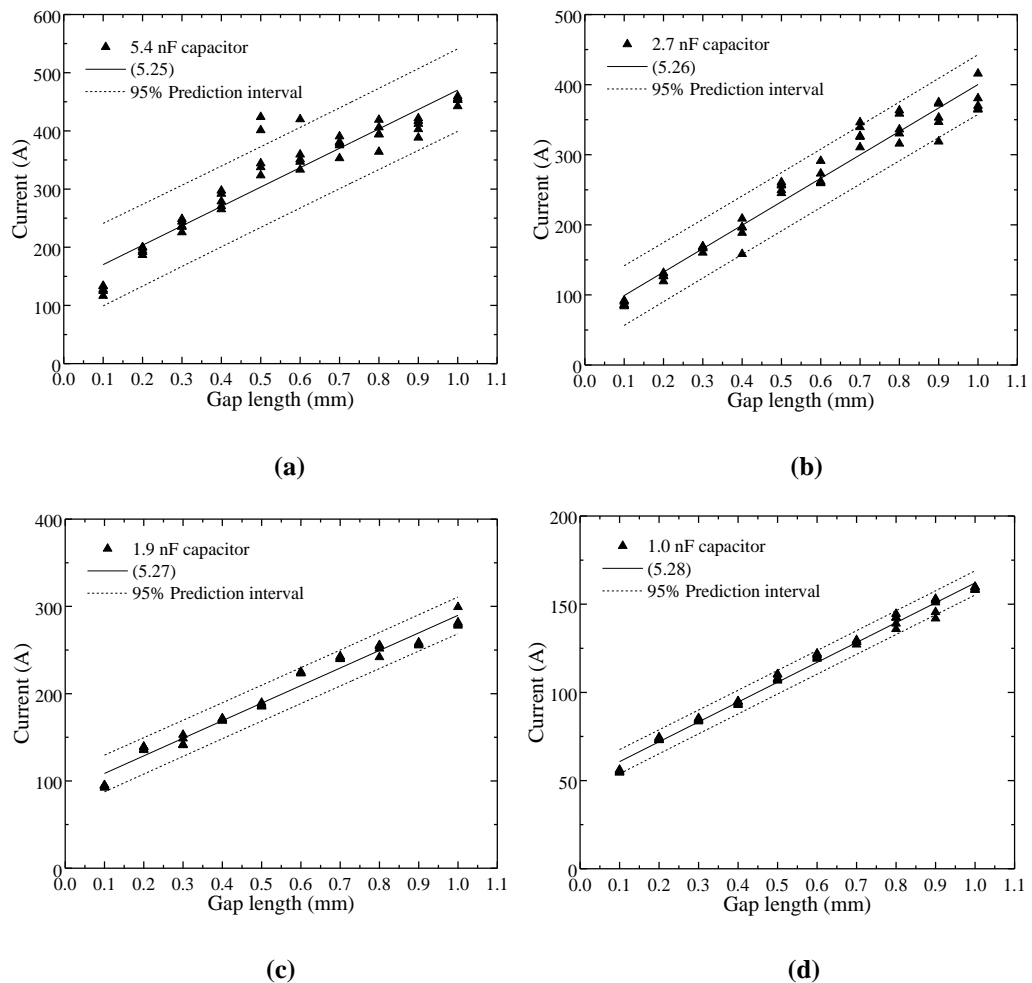


**Figure 5.14** Arc current for (a) 5.4 nF, (b) 2.7 nF, (c) 1.9 nF and (d) 1.0 nF capacitor. 5 sparks for each gap length and each capacitor value are shown. The solid lines give the best analytical fitting using equations (5.25) to (5.28). The dashed lines represent the bottom and top 95% prediction intervals.

### 5.5.1.3 Arc resistance

The equivalent constant resistance of the circuit,  $R_d$ , consists of two components: the constant resistance of the arc discharge in the spark gap,  $R_{eqarc}$ , and the stray resistance of the remaining circuit,  $R_{res}$ :  $R_d = R_{eqarc} + R_{res}$ .  $R_d$  was calculated following the methodology described in Subchapter 5.4 for 10 inter-electrode spark gap lengths (0.1 to 1.0 mm). The  $R_{eqarc}$  was subsequently calculated extracting the  $R_{res}$  from  $R_d$ . Table 5.5 summarises the results obtained from the analysis.

**Table 5.5** Equivalent constant arc resistance for 4 capacitor sizes and 10 inter-electrode gap lengths.

Inter-electrode gap length (mm)	Equivalent constant arc resistance ( $\Omega$ )			
	1.0 nF	1.9 nF	2.7 nF	5.4 nF
0.1	4.45	2.08	2.30	1.15
0.2	4.12	2.03	1.80	0.97
0.3	4.05	2.09	1.62	0.95
0.4	4.00	2.00	1.62	0.94
0.5	3.99	2.05	1.34	0.87
0.6	4.02	1.96	1.44	0.98
0.7	3.98	2.05	1.28	1.06
0.8	4.06	2.22	1.34	1.18
0.9	4.17	2.20	1.42	1.34
1.0	4.11	2.57	1.54	1.60

A strong dependency of the arc resistance on the capacitance can be observed. The higher the capacitance is, the more energy is available in the discharge, and the lower the arc resistance value will be. The variation in the gap length also affects the resistance value. The resistance starts with a higher value for smaller gaps, then decreases for medium gaps and, finally, as the gap becomes larger, the resistance increases again.

#### 5.5.1.4 Arc energy

The available energy to be deposited in the discharge is controlled by the stored energy in the capacitor of the circuit ( $E_{\text{stored}} = 1/2CV^2$ ). Part of the stored energy is converted into losses in the circuit, and the rest is available for the discharge. Table 5.6 presents an estimation of the stored energy in the capacitor for each inter-electrode gap. The breakdown voltages shown in the second column of the table have been calculated using Equation (5.24).

**Table 5.6** Stored energy in the capacitor available for arc plasma channel discharge.

Inter-electrode gap length (mm)	Breakdown voltage (kV)	Stored energy in the capacitor (mJ)			
		1.0 nF	1.9 nF	2.7 nF	5.4 nF
0.1	1.33	0.88	1.68	2.39	4.78
0.2	1.66	1.38	2.62	3.72	7.44
0.3	1.99	1.98	3.76	5.35	10.69
0.4	2.32	2.69	5.11	7.27	14.53
0.5	2.65	3.51	6.67	9.48	18.96
0.6	2.98	4.44	8.44	11.99	23.98
0.7	3.31	5.48	10.41	14.79	29.58
0.8	3.64	6.62	12.59	17.89	35.77
0.9	3.97	7.88	14.97	21.28	42.55
1.0	4.3	9.25	17.57	24.96	49.92

The equivalent constant resistance of the arc discharge,  $R_{\text{eqarc}}$ , was calculated for each spark gap length and each capacitor value, and used for the arc energy calculations. The arc current waveforms,  $I_{\text{arc}}(t)$ , for each spark gap length and each capacitor value were obtained experimentally and used for the arc energy calculations. Thus, the arc energy was calculated as an integral of the form:  $\int_0^t I_{\text{arc}}(t)^2 R_{\text{eqarc}} dt$ . The calculated arc energy is shown in Figure 5.15 and the analytical expressions for each fitting line are given in equations (5.29) to (5.32). The fitting lines obtained are shown as solid lines in Figure 5.15(a) to Figure 5.15(d). The 95% prediction intervals are also shown in Figure 5.15(a) to Figure 5.15(d). The dashed lines represent the bottom and top 95% prediction intervals.

$$\text{for 5.4 nF capacitor : } E_{\text{arc}}(d) = -1.64 + 16.24d \quad (5.29)$$

$$\text{for 2.7 nF capacitor : } E_{\text{arc}}(d) = -0.88 + 9.13d \quad (5.30)$$

$$\text{for 1.9 nF capacitor : } E_{\text{arc}}(d) = -0.27 + 5.70d \quad (5.31)$$

$$\text{for 1.0 nF capacitor : } E_{\text{arc}}(d) = -0.05 + 2.71d \quad (5.32)$$

where  $E_{\text{arc}}(d)$  in mJ and  $d$  in mm.

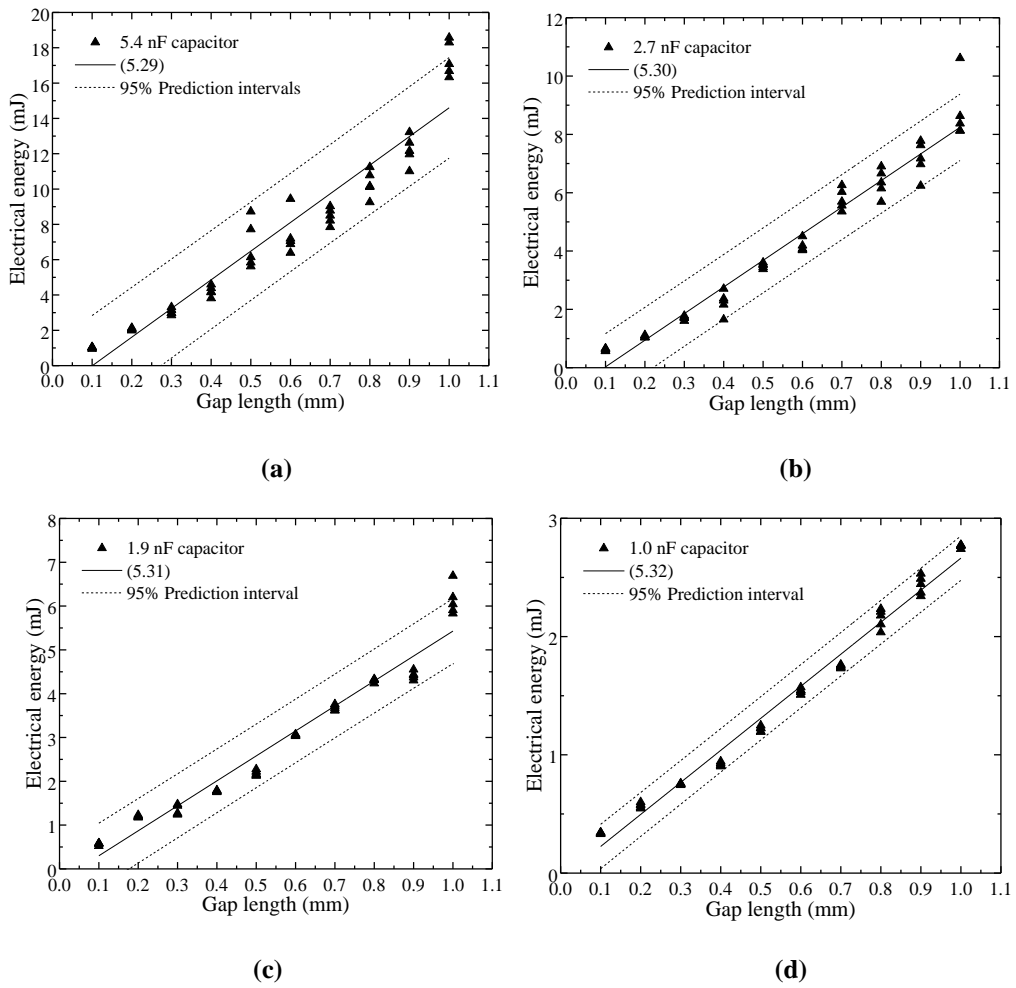


**Figure 5.15** Arc electrical energy for (a) 5.4 nF, (b) 2.7 nF, (c) 1.9 nF and (d) 1.0 nF capacitor.

5 sparks for each gap length and each capacitor value are shown. The solid lines give the best analytical fitting using Equation (5.29) – Equation (5.32). The dashed lines represent the bottom and top 95% prediction intervals.

## 5.5.2 WGS topology

### 5.5.2.1 Stabilised voltage

The stabilised voltages,  $V_{\text{st}}(d)$ , for 8 inter-electrode gap lengths and for the 80 nF capacitor value were acquired for each inter-electrode spark gap length. The longer the wire-guided spark gap length is, the longer time duration for the stabilised voltage has been observed. A linear least squares fitting procedure in Origin Pro 9 graphing software was used to fit analytical straight line to all the experimental data points simultaneously. The fitting line



obtained is shown as solid line in Figure 5.16, the function is given in Equation (5.33). The 95% prediction intervals are also shown in Figure 5.16. The dashed lines represent the bottom and top 95% prediction intervals.

$$V_{st}(d) = 12.32 - 0.05d \quad (5.33)$$

where  $V_{st}(d)$  in kV and  $d$  in mm.

The red point on the graph depicts the PCS breakdown voltage with a 0 cm WGSG, and it is excluded from the fitting procedure.

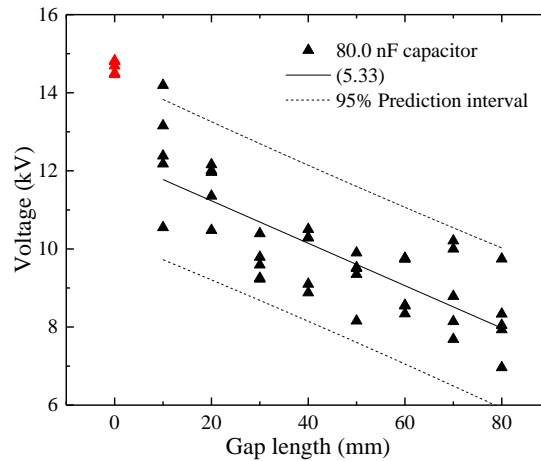


**Figure 5.16** Stabilised voltages for 8 inter-electrode gap lengths and 80 nF capacitor value. 5 sparks for each gap length are shown. The solid line gives the best analytical fitting using Equation (5.33).

The dashed lines represent the bottom and top 95% prediction intervals.

### 5.5.2.2 Arc current

Following the methodology described in Subchapter 5.3.2.2, the accurate arc current waveforms were obtained and the maximum value for the current in these waveforms were defined. Figure 5.17 presents the obtained experimental data and the fitting line shown as solid line, the function is given in Equation (5.34). The 95% prediction intervals are also shown in Figure 5.17. The dashed line represents the bottom and top 95% prediction intervals.

$$I_{arc}(d) = 2.93 - 0.02d \quad (5.34)$$

where  $I_{arc}(d)$  in kA and  $d$  in mm.

The red point on the graph depicts the PCS breakdown voltage with a 0 cm WGSG, and it is excluded from the fitting procedure.

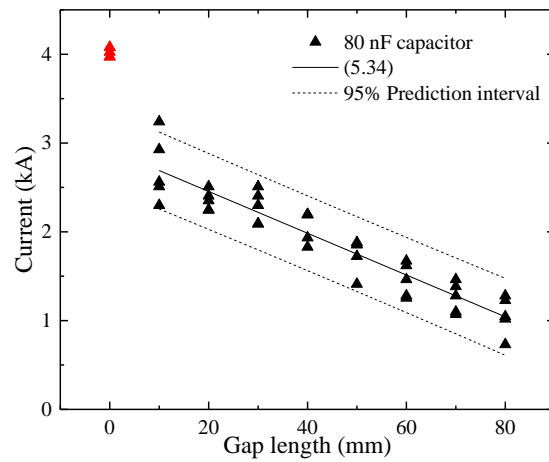


**Figure 5.17** Arc current for 8 inter-electrode gap lengths and for 80 nF capacitor. 5 sparks for each gap length are shown. The solid line gives the best analytical fitting using Equation (5.34). The dashed lines represent the bottom and top 95% prediction intervals.

### 5.5.2.3 Arc resistance

Table 5.7 summarises the results obtained from the analysis.

**Table 5.7** Equivalent constant arc resistance for the 80 nF capacitor and 8 inter-electrode gap lengths.

Inter-electrode gap length (cm)	Equivalent constant arc resistance ( $\Omega$ )
	80 nF
1	0.18
2	0.35
3	0.39
4	0.56
5	1.02
6	1.77
7	2.46
8	4.65

The equivalent constant discharging circuit resistance,  $R_d$ , is the total resistance of the circuit which includes both the PCS and the WGSG. Therefore,  $R_d$  is the sum of two equivalent constant resistances: the equivalent resistance of the circuit including the PCS,  $R_{pcs}$ , and the equivalent resistance of the wire-guided discharge alone,  $R_{eqarc}$ :  $R_d = R_{pcs} + R_{eqarc}$ .  $R_d$  was calculated following the methodology described in Subchapter 5.4 for each wire length from 1 cm to 8 cm.

#### 5.5.2.4 Arc energy

The available energy to be deposited in the discharge is controlled by the stored energy in the capacitor of the circuit ( $E_{stored} = 1/2CV^2 = 8$  J). A part of the stored energy is lost in the circuit (these losses are considered to be negligible in the present model), another part of the stored energy is dissipated in the PCS ( $\sim 6$  J). The rest of the stored 8J is available in the wire-guided arc discharge. This loss factor is mainly considered for determining the energy levels expected in the wire-guided arc discharge in the subsequent analysis. Table 5.8 presents a calculation of the dissipated energy in the wire-guided arc discharge for each inter-electrode gap length. The arc discharge initiation in the WGSG was achieved through the fast Joule evaporation of a copper wire, following closure of the PCS. The breakdown voltages shown in the second column of Table 5.8 (calculated using Equation (5.33)) correspond to the stabilised voltage during the evaporation of the copper wire.

**Table 5.8** Dissipated energy in the wire-guided arc plasma channel discharge.

Inter-electrode gap length (cm)	Stabilised voltage (kV)	Energy available in discharge (J)
		80 nF
1	11.82	1.12
2	11.32	1.27
3	10.82	1.42
4	10.32	1.57
5	9.82	1.72
6	9.32	1.87
7	8.82	2.02
8	8.32	2.17

The calculated arc energy is shown in Figure 5.18. The fitting line obtained is shown as solid line in Figure 5.18, the function is given in Equation (5.35). The 95% prediction intervals are also shown in Figure 5.18. The dashed lines represent the bottom and top 95% prediction intervals.

$$\text{for } 80 \text{ nF capacitor : } E_{\text{arc}}(d) = 0.97 + 0.015d \quad (5.35)$$

where  $E_{\text{arc}}(d)$  in J and  $d$  in mm.

The red point on the graph depicts the PCS electrical energy with a 0 cm WGSG, and it is excluded from the fitting procedure.

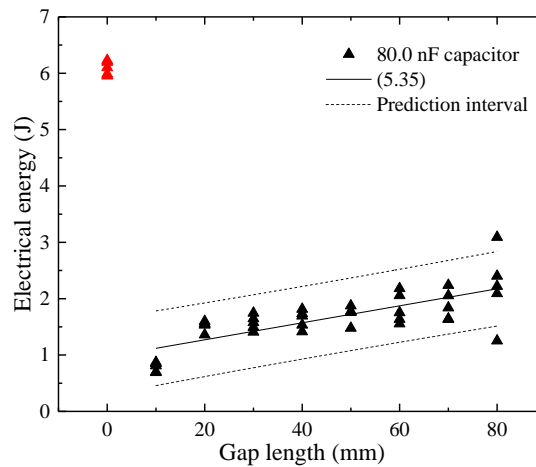


**Figure 5.18** Arc electrical energy for 8 inter-electrode gap lengths and 80 nF capacitor. 5 sparks for each gap length are shown. The solid line gives the best analytical fitting using Equation (5.35). The dashed lines represent the bottom and top 95% prediction intervals.

## 5.6 Transient arc resistance

The analysis so far was conducted assuming that the equivalent constant arc resistance represents adequately the relationship between the voltage and the current of the arc discharge. However, the arc discharge is a transient phenomenon and the transient arc resistance should be defined. In the Subchapter 5.6, the transient resistance of the 0.5 mm gap length and 1.9 nF capacitor for the SBSG and the 3 cm gap length and 80 nF capacitor for the WGSG is calculated and compared to the equivalent constant resistance.

The transient impedance of the arc (which is considered to be purely resistive) is defined for the 1<sup>st</sup> half cycle of the current oscillation. During this period, most of the energy is

dissipated in the arc. The temporal development of the transient resistance was acquired by dividing the arc voltage,  $V_{\text{arc}}(t)$  by the current,  $I_{\text{arc}}(t)$ , Equation (5.36).

$$R_{\text{trarc}}(t) = \frac{V_{\text{arc}}(t)}{I_{\text{arc}}(t)} \quad (5.36)$$

Several researchers have published their models describing arc transient resistance. Most of them suggest that the arc resistance is proportional to a function of spark length and inversely proportional to a function of spark current [Toe06], [EDK89], [Bra58], [RW44], [BVL75], [PPP74], [DMS+68], [AKK+88], [Maa85]. The transient resistance is expected to have a high value at the very beginning of the transient process when the current is small, then, the resistance decreases with the current increase and start to increase with the current decrease during the transient current oscillation. This is a typical arc resistance behaviour, which was also observed in the present work.

Figure 5.19(a) shows the transient resistance calculated for the 1<sup>st</sup> half cycle of the current waveform. Also, the equivalent constant resistance is presented to compare it with the transient resistance. Their comparison shows that the transient and the equivalent constant resistance have values of the same order of magnitude around the maximum current. The equivalent constant resistance seems to fit well enough the transient resistance when it reaches its minimum value and stays almost constant during 30 ns, in the case of 0.5 mm gap length. Similar behaviour is observed in the case of the 3 cm gap length and 80 nF capacitor, Figure 5.19(b). The equivalent constant resistance seems to fit well enough the transient resistance when it reaches its minimum value and stays almost constant during 0.6  $\mu\text{s}$ . It should be noted that for the case of the SBSG topology, the noise interference in the acquired waveforms is an important contributing factor and the extended mathematical analysis followed resulted in slightly distorted final waveforms.

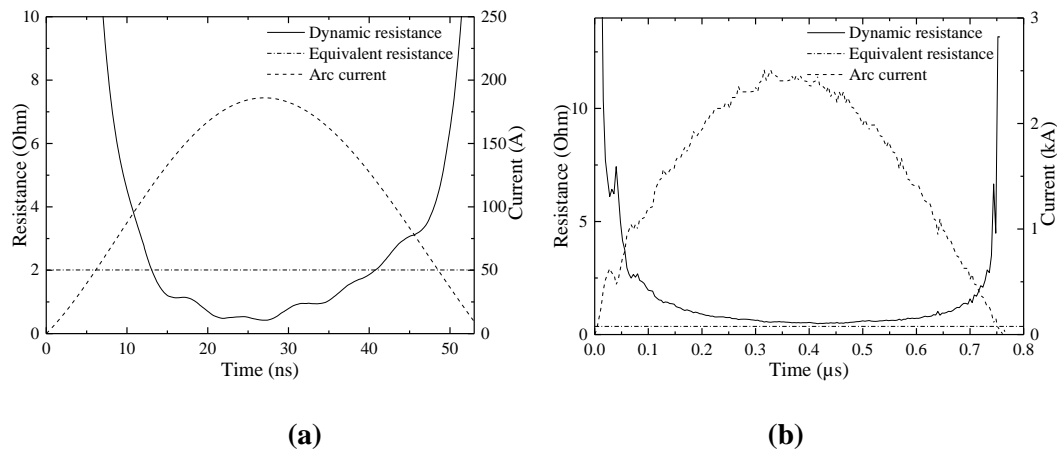


**Figure 5.19** Transient resistance for **(a)** a 0.5 mm gap length and 1.9 nF capacitor, SBSG topology and **(b)** a 3 cm gap length and 80 nF capacitor, WGSG topology.

For further verification, the dissipated energy during the 1<sup>st</sup> half cycle was calculated using the transient resistance and was compared to the energy calculated using the equivalent constant resistance. Figure 5.20 presents representative results for both cases and Table 5.9 tabulates the energy values at the end of the 1<sup>st</sup> half cycle. It can be observed that the calculated energy values for the WGSG are of the same order of magnitude. For the SBSG, the accuracy of this method is not enough to provide solid evaluation of such small values of energy. Despite the discrepancy in the transient and constant energy (for the SBSG), it can be confirmed that the dissipated energy is much smaller than the energy dissipated in the WGSG topology. For different individual arc discharges, there are also additional slight discrepancies in the results since the phenomenon is stochastic (for both the SBSG and the WGSG topologies).

To conclude, the analysis of the dynamic resistance of the spark discharge poses significant challenges which are related to the very fast evolving processes taking place within very short time scale. These processes are also difficult to be monitored due to limitations of the diagnostic devices.

**Table 5.9** Dissipated energy in the wire-guided arc discharge.

	Energy (mJ)	Energy (J)
	SBSG (1.9 nF)	WGSG (80 nF)
Transient	11.12	1.59
Constant	1.72	1.24

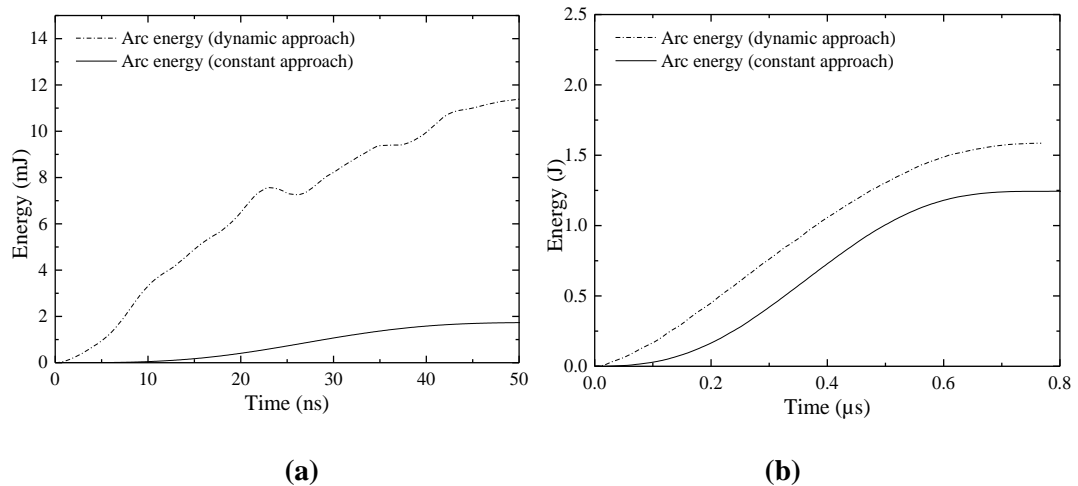


**Figure 5.20** Dynamic energy for (a) a 0.5 mm gap length and 1.9 nF capacitor, SBSG topology and (b) a 3 cm gap length and 80 nF capacitor, WGSG topology.

## 5.7 Conclusions

The results obtained in the present chapter presents the electrical characteristics of transient arcs created in both sub-mm spark gaps and longer (several cm) spark gaps. The transient process in these gaps has an oscillatory (AC) character. The investigation has been focused on the initiation phase of the discharge through analysis of the obtained voltage and current waveforms.

The accurate arc plasma channel voltage and current has been obtained with the aid of lumped element circuit theory. Lumped element models (LEM) have been developed for both the SBSG and the WGSG topologies. This representation simplifies the behaviour of spatially distributed electrical systems into a topology consisting of lumped elements and allows further analysis to be performed.

In the conducted analysis, the resistive and inductive components in the obtained experimental waveforms have been separated and accurate resistive and power characteristics of the arc have been obtained. For both the SBSG and WGSG topologies, considering the arc resistance as a time-independent passive circuit element, the circuit can be represented by an RLC circuit with underdamped response. Following the technique described by Greason in [Gre99], the equivalent constant resistance,  $R_{\text{eqarc}}$ , has been obtained using the experimental current waveforms for each topology. The term “equivalent constant resistance” refers to the effective resistance of the circuit or element under consideration.

Based on the equivalent constant resistance the electrical energy available in the discharge has been calculated.

A strong dependency of the arc resistance on the capacitance of the energy storage capacitor used in the discharge circuit have been observed. The higher the capacitance, the more energy is available in the discharge, and the lower the arc resistance value. The variation in the gap length also affects the resistance value. The resistance starts with a higher value for smaller gaps, then decreases for medium gaps and, finally, as the gap becomes larger, the resistance increases again.

Furthermore, a comparison between the energy calculation based on the transient and the equivalent constant arc resistance has been performed. Analysis of the transient resistance poses many challenges which are related to the very fast evolving processes taking place within very short time scales. These processes are also difficult to be monitored due to equipment limitations. More accurate results have been extracted for the case of the WGSG discharges. The equivalent constant resistance seems to fit well enough the transient resistance when it reaches its minimum. Moreover, it has been observed that the calculated transient and constant energy values for the WGSG are of the same order of magnitude.

To conclude, Chapter 5 presents three major novel elements:

- The accurate acquisition of electrical characteristics during arc initiation in a busbar to point electrode spark gap topology during two ways of initiation (free discharges (SBSG) and wire-guided discharges (WGSG)).
- Data post-processing techniques which have been developed and implemented in MATLAB to extract arc voltage and current waveforms for calculating the electrical arc energy available in the discharge.
- The comparison between energy calculations during arc initiation based on transient and equivalent constant arc resistance parameters.

An analytical model, developed on the basis of hydrodynamic theory, is presented in Chapter 6. Using the developed model, the electrical energy deposited into the arc plasma channel calculated in the present chapter will be analysed in the energy components associated with thermal, acoustic-kinetic and light emission processes during arc initiation.



## Chapter 6

---

# Energy partition during arc initiation

Chapter 6 focuses on the energy partition during the initiation phase of the arc fault. An analytical model, developed on the basis of hydrodynamic theory, is presented. This model allows the energy components associated with thermal, acoustic-kinetic and light emission processes during arc initiation to be obtained. Subchapter 6.1 introduces thermodynamics and fluid dynamics basic principles that constitute the basis of the formation of the analytical expressions of the energy partition model. Subchapters 6.2 and 6.3 present the development of the analytical model and discuss the results obtained. Finally, Subchapter 6.4 outlines the conclusions derived from the results analysis.

### **6.1 Thermodynamics and fluid dynamics principles and their application in the energy partition model development**

Three fundamental concepts of physics, the conservation of energy, mass and momentum, are utilised for the energy partition model development. Conservation of mass and conservation of momentum are the basic equations that describe the macroscopic fluid flow. In the energy partition model, the arc plasma channel is considered as a fluid which interacts with the atmospheric air, and it is treated as a continuum.

In addition to the fluid dynamics principles, the interrelated thermodynamics principles utilisation is necessary for the development of the analytical model. Conservation of energy is the basic equation that describes the heat and thermodynamic processes in a well-defined thermodynamic system. The arc plasma channel is considered as a closed thermodynamic system in the present analysis. Subchapters 6.1.1, 6.1.2 and 6.1.3 introduce the three conservation equations that constitute the basis of the energy partition model presented in

Subchapter 6.2. Additionally, Subchapter 6.2 discusses the limitations and assumptions of the approach presented in the study.

### 6.1.1 Conservation of energy

The conservation of energy equation, in the context of thermodynamics, states that the energy is conserved in a closed thermodynamic system and only transforms from one form to another. Equation (6.1) presents the First Law of Thermodynamics (conservation of energy) which states that the total energy added to a closed thermodynamic system due to heating processes should be equal to the change in the internal energy of the system and the energy lost by the system due to the mechanical work done by the system on its surrounding environment:

$$\delta Q = \delta U + \delta W \quad (6.1)$$

where:

$\delta Q$  : energy added to the system due to heating processes [J]

$\delta U$  : change in the internal energy of the system [J]

$\delta W$  : energy lost by the system due to mechanical work done by the system on its surrounding environment [J]

The arc plasma channel is considered as a closed thermodynamic system which can exchange energy in the form of heat and/or mechanical work with its surrounding atmospheric air but there is no exchange of matter. Thus, the conservation of energy equation can be used to describe the bulk energy partition during the initial phase of the electrical discharge.

### 6.1.2 Conservation of mass

The conservation of mass equation (equation of continuity) states that the mass is conserved inside a well-defined volume. Thus, the rate of decrease of mass in the volume within the fluid equals the mass flux out of this volume, Equation (6.2):

$$-\frac{d}{dt} \int_{\Omega} \rho d\Omega = \int_S \rho \mathbf{v} \cdot \hat{\mathbf{n}} dS \quad (6.2)$$

where:

$\rho$  : density [kg/m<sup>3</sup>]

$\Omega$  : mass volume [m<sup>3</sup>]

$\mathbf{v}$  : velocity vector [m/s]

$S$  : surface [m<sup>2</sup>]

$t$  : time [s]

$\hat{\mathbf{n}}$  : is the unit vector normal to the surface.

The right-hand side of Equation (6.2) can be converted to a volume integral using divergence theorem, as shown in Equation (6.3):

$$\int_S \rho \mathbf{v} \cdot \hat{\mathbf{n}} dS = \int_{\Omega} \nabla \cdot (\rho \mathbf{v}) d\Omega \quad (6.3)$$

Combining Equation (6.2) and Equation (6.3) results in the well-known continuity equation that states that the mass is conserved everywhere in the system under consideration, Equation (6.4):

$$\frac{\partial \rho}{\partial t} + \nabla \cdot (\rho \mathbf{v}) = 0 \quad (6.4)$$

### 6.1.3 Conservation of momentum

The second important equation used in fluid dynamics is the conservation of momentum equation that states that the rate of change of momentum should be equal to the total force exerted on the fluid (Newton's second law), Equation (6.5). In the present analysis, an infinitesimally small cubic volume of fluid with volume  $d\Omega$  is considered. The total force exerted on the fluid consists of the external forces that act on the fluid body and the internal forces that act on the molecules of the fluid. Gravity is considered in the present model as the only external force exerted on the fluid body, 1<sup>st</sup> term of the right-hand side of Equation (6.5). The internal molecular forces due to interactions between the elements of the fluid are considered to act on an infinitesimally thin surface layer. In 3D space, a normal and

two shear stresses (mutual normal) are exerted on each surface plane of an element, 18 stresses components in total. Due to equilibrium each of the stresses of a plane are balanced by equal and opposite in direction stress acting on opposite planes. Therefore, only half of the cubic element's stress components are taken into account to describe its state and form the 3x3 stress tensor  $\mathbf{\Pi}$ . The stress tensor is used to define the force,  $\mathbf{f} = \mathbf{\Pi} \cdot \hat{\mathbf{n}}$ , exerted per unit area on a surface element  $dS$ .

$$\frac{d}{dt} \int_{\Omega} d\Omega \rho \mathbf{v} = \int_{\Omega} d\Omega \rho \mathbf{g} + \int_S \mathbf{f} dS \quad (6.5)$$

where:

$\mathbf{g}$  : gravitational acceleration vector [ $\text{m/s}^2$ ]

The 2<sup>nd</sup> term of the right-hand side of Equation (6.5) can be converted to a volume integral using divergence theorem, Equation (6.6):

$$\int_{\Omega} d\Omega \rho \mathbf{g} + \int_S \mathbf{f} dS = \int_{\Omega} d\Omega (\rho \mathbf{g} + \nabla \cdot \mathbf{\Pi}) \quad (6.6)$$

Combining Equation (6.5) and Equation (6.6) results in the well-known Cauchy equation that states that the momentum is conserved everywhere in the system under consideration, Equation (6.7):

$$\rho \frac{d\mathbf{v}}{dt} = \rho \mathbf{g} + \nabla \cdot \mathbf{\Pi} \quad (6.7)$$

#### *Constitutive relations*

The stresses acting on each element of the fluid are a combination of pressure,  $P$ , and viscous friction, equations (6.8) to (6.10). The components of these stresses in 3D Cartesian coordinates can be represented as:

$$\Pi_{xx} = -P + \lambda \nabla \cdot \mathbf{v} + 2\mu \frac{\partial u}{\partial x}, \quad \Pi_{xy} = \mu \left( \frac{\partial u}{\partial y} + \frac{\partial v}{\partial x} \right) \quad (6.8)$$

$$\Pi_{yy} = -P + \lambda \nabla \cdot \mathbf{v} + 2\mu \frac{\partial v}{\partial y}, \quad \Pi_{yz} = \mu \left( \frac{\partial v}{\partial z} + \frac{\partial w}{\partial y} \right) \quad (6.9)$$

$$\Pi_{zz} = -P + \lambda \nabla \cdot \mathbf{v} + 2\mu \frac{\partial w}{\partial z}, \quad \Pi_{xz} = \mu \left( \frac{\partial u}{\partial z} + \frac{\partial w}{\partial x} \right) \quad (6.10)$$

where:

$\mu$  and  $\lambda$  : the coefficients of dynamic and bulk viscosity respectively [Pa·s]

$u$ ,  $v$  and  $w$  : velocity component parallel to axis  $x$ ,  $y$  and  $z$  respectively [m/s]

These expressions assume that the relationship between stress and velocity gradients is linear (which is valid for Newtonian fluids).

### 6.1.4 Model assumptions

For the development of the energy partition model, a number of assumptions were made, mainly for simplification reasons. These assumptions are listed and described below:

- *Ideal gas*

The real gas (atmospheric air) is idealised as an ideal gas. Thus, the ideal gas law is valid for the description of the behaviour of the gas.

- *Incompressible flow – Incompressible Navier-Stokes equations*

For incompressible flow  $\nabla \cdot \mathbf{v} = 0$  and the conservation of momentum equation is simplified.

- *No external body forces*

The external body forces that act on the material as a whole are considered zero. In Equation (6.7), gravity was the only external force considered which, according to the present assumption, is defined as zero.

- *No bulk and dynamic viscosity of the fluid – Perfect fluid*

The bulk and dynamic viscosity of the fluid,  $\lambda$  and  $\mu$ , are considered zero. This simplifies further Equation (6.8) to Equation (6.10).

- *Model development in spherical coordinates*

The arc plasma channel column initiates as a cylinder. Depending on the length of the spark gap, the arc plasma channel transforms into a sphere quite fast. For short, sub-mm spark gap lengths, it can be assumed that the spark plasma channel transforms into sphere almost instantaneously. For longer spark gaps, the model can be developed in spherical coordinates, too. The arc plasma channel discharge created in a longer spark gap length initiates as a cylinder and, when the radius of the arc plasma channel becomes larger than the half of the length of the cylinder ( $r_{\text{cyl}} \gtrsim h_{\text{cyl}}/2$ ), it is assumed that it converts into a sphere. However, the model will be developed only in spherical coordinates. This can be achieved if for the initial stage

of the discharge the cylindrical volume of the discharge is converted in the corresponding spherical volume. Then, the radius of the volume can be defined and used in the simulations, even from the beginning of the discharge. Since, in the present study, the initial arc plasma channel radius and the corresponding cylindrical volume is very small, the relevant spherical ones can be used instead.

Taking into account these assumptions, the analytical model that predicts the evolution of the arc plasma radius and subsequently the energy partition and the pressure developed in the arc plasma channel column can be developed. Subchapter 6.2 presents the gradual energy model development in spherical coordinates.

## **6.2 Energy partition model development in spherical coordinates**

Subchapter 6.1 introduced the basic principles of thermodynamics and fluid dynamics to set the necessary brief theoretical background for developing the analytical expressions of the energy partition model. Thus, on the basis of hydrodynamic theory, estimation of the energy partition into thermal energy, mechanical work (acoustic-kinetic) and light emission can be achieved.

In several studies, the dynamics of arc plasma expansion in gases have been investigated [Dra51], [Bra58], [Mar60], [TBI+07]. A well-established, previously-developed theory describes the arc channel expansion based on the concepts of hydrodynamics (fluid dynamics) and considers the plasma channel as a piston that pushes the surrounding medium, establishing a shock-wave [Dra51], [Bra58]. Several publications discuss the dynamics of the arc plasma expansion, with emphasis given to the pressure and velocity fields produced in liquids, [TMG+08], [TFG+06], [BPV09], [RCR+96], [KGV11], [HG04]. Since the electrical discharge involves complex electronic and hydrodynamic processes, the development of the discharge can be described with the help of certain parameters: plasma channel resistance and its radius, plasma temperature, pressure in the channel and energy dissipation.

For the development of this model, a number of assumptions were made, which have been described in Subchapter 6.1.4. Atmospheric air was considered as a Newtonian fluid (non-viscous, thermally non-conducting, ideal gas) that expands only in the radial direction,

[TBI+07]. The non-disturbed gas density,  $\rho_0$ , was considered constant at  $1.2 \text{ kg/m}^3$ , and the atmospheric pressure,  $P_0$ , was considered constant at  $101 \text{ kPa}$ . The plasma channel resistance was assumed to remain constant during the phenomenon development. Although a range of temperatures for the arc plasma channel in non-thermal plasmas is referred in several publications [TTT+06], [BNG+02], [Fri08], the plasma channel temperature is considered to be constant,  $\sim 7,000 \text{ K}$ , in the present model, representing an average plasma temperature in spark discharge. This temperature value is confirmed through analysis of optical emission spectra of plasma channels formed within similar spark gap lengths and for similar energy levels [McG17].

The model has been developed using Braginskii's hydrodynamic energy balance equation [Bra58], which states that the electrical energy deposited in the plasma discharge by Joule heating is converted into the internal energy of the plasma and mechanical work done by the expanding plasma. Light emission has also been taken into account in the present model. The plasma channel is considered as a blackbody radiator with emissivity factor  $\sim 0.1$  [RCR+96], and its thermal radiation is described by the Stefan-Boltzmann law. The energy losses due to heat (thermal) conduction are assumed negligible during this initial stage of the arc formation.

The energy balance equation which constitutes the basis of the model is given by Equation (6.11). This equation links the pressure in the plasma channel and its volume with the electrical energy delivered to the plasma. On the left-hand side of Equation (6.11), there are three terms which represent the internal energy (kinetic and ionisation energy) stored in the gas, the mechanical work done by the expanding arc plasma channel, and the energy associated with light emission from the arc. These three energy components are balanced by the electrical energy deposited into the arc plasma channel, which is given by the term in the right-hand side of Equation (6.11) and calculated in Chapter 5.

$$\frac{P(t_d)\Omega(t_d)}{c_{pv} - 1} + \int_0^{\Omega(t_d)} P(t)d\Omega + \int_0^{t_d} 4\pi r(t)^2 \zeta \eta T^4 dt = \int_0^{t_d} I_{\text{arc}}(t)^2 R_{\text{eqarc}} dt \quad (6.11)$$

where:

$P(t)$  : temporal pressure in the plasma channel [Pa]

$\Omega(t)$  : temporal volume of the plasma channel [ $\text{m}^3$ ]

$c_{pv}$  : heat capacity ratio/ratio of specific heats (1.4 for dry air at  $20 \text{ }^\circ\text{C}$ )

$t_d$  : duration of the electrical discharge [s]

- $r(t)$  : temporal plasma column/electrical discharge radius [m]  
 $\xi$  : plasma channel emissivity factor,  $\sim 0.1$   
 $\eta$  : Stefan-Boltzmann constant,  $5.67 \cdot 10^{-8}$  [W/m<sup>2</sup>K<sup>4</sup>]  
 $T$  : plasma channel temperature,  $\sim 7,000$  [K]  
 $I_{\text{arc}}(t)$  : temporal electrical arc discharge current [A]  
 $R_{\text{eqarc}}$  : resistance of the electrical discharge [ $\Omega$ ]

As mentioned in Subchapter 6.1.4, it was decided that the model will be developed in the spherical coordinates system. The assumption that the discharge plasma in air rapidly transforms into a spherically-expanding hot gas “ball”, regardless the spark gap length, was made for the present analysis. Thus, the equivalent spherical topology can be used. This assumption was discussed and confirmed in [Lee96].

The arc plasma channel temporal volume in spherical coordinates,  $\Omega_{\text{sph}}(t)$ , is given by Equation (6.12). The time derivative of the volume of the arc plasma,  $d\Omega_{\text{sph}}(t)/dt$ , Equation (6.13), is also required and calculated to be substituted into Equation (6.11).

#### *Arc plasma channel volume*

$$\Omega_{\text{sph}}(t) = \frac{4}{3} \pi r^3(t) \quad (6.12)$$

$$\frac{d\Omega_{\text{sph}}(t)}{dt} = 4\pi r^2(t) \frac{dr(t)}{dt} \quad (6.13)$$

#### *Arc plasma channel pressure*

The analytical expression for  $P(t)$  is derived to be substituted into Equation (6.11), and it is defined as a function of the electrical arc plasma channel radius, Equation (6.17). The conservation of momentum equation for incompressible, perfect fluid (Navier-Stokes) in spherical coordinates ( $r$ ,  $\varphi$  and  $\theta$ ), Equation (6.14), is being used to derive the arc plasma channel pressure equation. It is assumed that the fluid expands only in the direction of  $r$ -axis and the expansion in the  $\varphi$  and  $\theta$  direction is neglected.



$$\begin{aligned}
& \rho_0 \left( \frac{\partial v_r}{\partial t} + v_r \frac{\partial v_r}{\partial r} + \frac{v_\theta}{r} \frac{\partial v_r}{\partial \theta} + \frac{v_\varphi}{r \sin \theta} \frac{\partial v_r}{\partial \varphi} - \frac{v_\theta^2 + v_\varphi^2}{r} \right) = \\
& -\frac{\partial P}{\partial r} + \mu \left( \frac{\partial}{\partial r} \left( \frac{1}{r^2} \frac{\partial}{\partial r} (r^2 v_r) \right) \right) + \frac{1}{r^2 \sin \theta} \frac{\partial}{\partial \theta} \left( \sin \theta \frac{\partial v_r}{\partial \theta} \right) + \\
& \frac{1}{r^2 \sin^2 \theta} \frac{\partial^2 v_r}{\partial \varphi^2} - \frac{2}{r^2 \sin \theta} \frac{\partial}{\partial \theta} (v_\theta \sin \theta) - \frac{2}{r^2 \sin \theta} \frac{\partial v_\varphi}{\partial \varphi} + \rho_0 g_r
\end{aligned} \tag{6.14}$$

where:

$v_r$  : fluid velocity in  $r$ -axis direction [m/s]

$v_\theta$  : fluid velocity in  $\theta$ -axis direction [m/s]

$v_\varphi$  : fluid velocity in  $\varphi$ -axis direction [m/s]

$g_r$  : gravitational acceleration component in  $r$ -axis direction [m/s]

Taking into account the assumptions presented in Subchapter 6.1.4, Equation (6.14) can be simplified and re-written as Equation (6.15).

$$\rho_0 \left( \frac{\partial v_r}{\partial t} + v_r \frac{\partial v_r}{\partial r} \right) = -\frac{\partial P}{\partial r} \tag{6.15}$$

Expressing Equation (6.15) in an integral form, Equation (6.16) is acquired:

$$\begin{aligned}
& \int_{P(t)}^{P_0} \partial P = -\rho_0 \left( \int_0^{r(t)} \frac{\partial v_r}{\partial t} \partial r + \int_0^{v_r(t)} v_r \partial v_r \right) = \\
& -\rho_0 \left( \int_0^{r(t)} \frac{\partial}{\partial t} \left( \frac{\partial r}{\partial t} \right) \partial r + \frac{v_r^2}{2} \right) = -\rho_0 \left( \frac{\partial^2}{\partial t^2} \int_0^{r(t)} r \partial r + \frac{v_r^2}{2} \right) \\
& = \rho_0 \left( \frac{\partial}{\partial t} \left( \frac{\partial}{\partial t} \left( \frac{r^2}{2} \right) \right) + \frac{v_r^2}{2} \right) = -\rho_0 \left( \frac{\partial}{\partial t} \left( r \frac{\partial r}{\partial t} \right) + \frac{v_r^2}{2} \right) \\
& = -\rho_0 \left( \left( r \frac{\partial}{\partial t} \left( \frac{\partial r}{\partial t} \right) \right) + \frac{\partial r}{\partial t} \frac{\partial r}{\partial t} + \frac{v_r^2}{2} \right) = -\rho_0 \left( r \frac{\partial^2 r}{\partial t^2} + \frac{3v_r^2}{2} \right)
\end{aligned} \tag{6.16}$$

$$P_0 - P(t) = -\rho_0 \left( r \frac{\partial^2 r}{\partial t^2} + \frac{3v_r^2}{2} \right) \text{ or } P(t) = P_0 + \rho_0 \left( r \frac{\partial^2 r}{\partial t^2} + \frac{3v_r^2}{2} \right) \quad (6.17)$$

### *Arc plasma channel radius*

By substituting Equations (6.12), (6.13) and (6.17) in Equation (6.11), a combined differential and integral equation is formed which presents the arc channel radius, this expression is given by Equation (6.18) and Equation (6.19). The radius of the arc plasma channel is  $r(t)$ ,  $dr(t)/dt$  and  $d^2r(t)/dt^2$  are the first and second order derivative of the radius respectively. The analytical model has been built and solved using MATLAB/Simulink software with solver ode45 (Dormand-Prince). Since the electrical power associated with the arc channel is measured experimentally, the arc channel radius can be expressed in terms of power during the energy deposition phase of the discharge [NR71].

$$\begin{aligned} & \frac{\left[ P_0 + \rho_0 \left( r \frac{d^2 r}{dt} + \frac{3}{2} \left( \frac{dr}{dt} \right)^2 \right) \right] \frac{4}{3} \pi r^3}{c_{pv} - 1} \\ & + \int_0^V \left[ P_0 + \rho_0 \left( r \frac{d^2 r}{dt} + \frac{3}{2} \left( \frac{dr}{dt} \right)^2 \right) \right] 4\pi r^2 \frac{dr}{dt} dt \\ & + \int_0^t 4\pi r^2 \zeta \eta T^4 dt = \int_0^t I_{arc}(t)^2 R_{eqarc} dt \end{aligned} \quad (6.18)$$

$$\begin{aligned} \frac{d^2 r}{dt^2} &= \frac{3(c_{pv} - 1)}{4\pi\rho_0 r^4} \left( \int_0^t I_{arc}(t)^2 R_{eqarc} dt - \int_0^t 4\pi r^2 \zeta \eta T^4 dt \right) \\ & - \frac{3c_{pv}}{2r} \left( \frac{dr}{dt} \right)^2 - \frac{P_0 c_{pv}}{\rho_0 r} \end{aligned} \quad (6.19)$$

The temporal development of the arc plasma channel radius can be predicted by integrating Equation (6.19) twice. Initial conditions are required for the solution, thus  $r(0)$  and  $dr(0)/dt$  should be defined, as presented in Subchapter 6.2.1. The initial conditions can be obtained using the conservation of mass equation. Once the radius of expansion is determined, the arc plasma radius velocity and its acceleration are also defined. Finally, the arc plasma channel pressure is obtained.

### 6.2.1 Initial conditions

The initial conditions,  $r(0)$  and  $dr(0)/dt$ , are determined and used in the solution of the integral-differential equation (6.19). The equation of mass conservation, Equation (6.4), can be re-written in spherical coordinates, Equation (6.20). This equation is used to define the initial conditions:

$$\begin{aligned} \rho_0 \left( \frac{\partial v_r}{\partial r} + \frac{1}{r} \frac{\partial v_\theta}{\partial \theta} + \frac{2v_r}{r} + \frac{1}{r \sin \theta} \frac{\partial v_\phi}{\partial \phi} + \frac{v_\theta \cot \theta}{r} \right) + \frac{\partial \rho_0}{\partial t} \\ + v_r \frac{\partial \rho_0}{\partial r} + \frac{v_\theta}{r} \frac{\partial \rho_0}{\partial \theta} + \frac{v_\phi}{r \sin \theta} \frac{\partial \rho_0}{\partial \phi} = 0 \end{aligned} \quad (6.20)$$

Taking into account the assumptions made in Subchapter 6.1.4 and assuming again that the expansion takes place only in r-axis (the  $v_\theta$  and  $v_\phi$  and their derivatives are equal to 0) and all derivatives of  $\rho_0$  are equal to 0, the equation of radial velocity of expansion of plasma channel can be defined, Equation (6.21):

$$\frac{\partial v_r}{\partial r} + \frac{2v_r}{r} = 0 \quad (6.21)$$

Equation (6.21) re-written in integral form provides a normalised equation for the initial conditions. The relation between the arc plasma radius and the arc plasma velocity is given in Equation (6.22).

$$\begin{aligned} \frac{\partial v_r}{v_r} + \frac{2\partial r}{r} = 0 \\ \int_{v_0}^{v_{r1}} \frac{\partial v_r}{v_r} + \int_{r_0}^{r_1} \frac{2\partial r}{r} = \ln v_r \Big|_{v_0}^{v_{r1}} + 2 \ln r \Big|_{r_0}^{r_1} = \ln \left( \frac{r_1}{r_0} \right)^2 + \ln \left( \frac{v_{r1}}{v_0} \right) = 0 \\ \ln \left( \frac{r_1}{r_0} \right)^{-2} = \ln \left( \frac{v_{r1}}{v_0} \right) \\ \left( \frac{r_1}{r_0} \right)^{-2} = \frac{v_{r1}}{v_0} \\ v_{r1} = v_0 \left( \frac{r_1}{r_0} \right)^2 \end{aligned} \quad (6.22)$$

where:

$r_0$  : initial arc plasma channel radius (is considered 0  $\mu\text{m}$ ) [m]

$r_1$  : arc plasma channel radius at the moment of interest – the time that the simulation starts (is considered  $1 \mu\text{m}$ ) [m]

$v_0$  : initial velocity of the arc plasma channel radius (considered unknown) [m/s]

$v_{r1}$  : velocity of the arc plasma channel radius at the moment of interest [m/s]

The initial value of the arc plasma radius used in simulations is  $1 \mu\text{m}$ , since computational limitations do not allow for using a zero value. Thus, using Equation (6.22), the velocity of the arc plasma channel radius at the moment of interest can be calculated as  $0 \text{ m/s}$ . This velocity value was used in the simulations as the initial value. Due to the computational limitations a small non-zero value of  $10^{-6} \text{ m/s}$  was used as the initial velocity of expansion of the arc channel.

For the case of the WSGS topology, a few different initial velocity values were tested. It was found that the solution to Equation (6.22) is not sensitive to variations in the initial velocity of expansion as the plasma arc channel evolves quickly and its dynamics is governed by energy deposition into the plasma. The range examined is from  $0$  to  $50 \text{ km/s}$ , Figure 6.1. The velocity quickly stabilises at the value of  $\sim 4 \text{ km/s}$  (accurate value is  $3.7 \text{ km/s}$ ) and then gradually starts to drop.

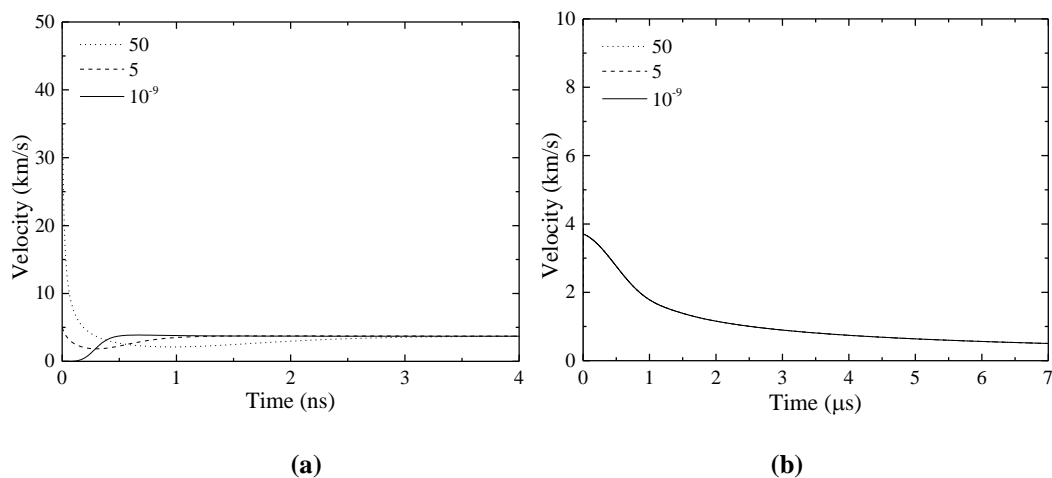


**Figure 6.1** Initial velocity values comparison for the case of the WSGS topology and for  $80 \text{ nF}$  and  $3 \text{ cm}$  inter-electrode spark gap length. **(a)** The temporal development of the velocity during the first  $4 \text{ ns}$  of the discharge (all waveforms coincide after  $3 \text{ ns}$ ), **(b)** The temporal development of the velocity during the whole duration of the discharge (all waveforms coincide).

### 6.3 Simulations results

Subchapter 6.3 presents the results of the energy partition simulations for the SBSG and WGSg topologies. Typical results of analytical analysis for 1.9 nF capacitor and 0.5 mm spark gap for the SBSG topology are presented in Subchapter 6.3.1. The analytical results for 80 nF capacitor and 3 cm spark gap for the WGSg topology are given in Subchapter 6.3.2. 5 individual simulations for each different inter-electrode spark gap length were run. All the results obtained have been consistent with the results presented in the present chapter.

A mathematical approach was used to develop the analytical model which describes the mechanisms involved in complex physical processes taking place during the discharge. The solution of the second order integral-differential equation, Equation (6.19), was used to calculate the energy components associated with the electrical discharge. Specifically, the three energy components, internal energy, mechanical work and light emission, are represented in the model as equations (6.23), (6.24) and (6.25), respectively:

*Internal energy*

$$E_{\text{internal}}(t) = \frac{4\pi r(t)^3 P(t)}{3 c_{pv} - 1} \quad (6.23)$$

*Mechanical work*

$$E_{\text{work}}(t) = \int_0^t 4\pi r(t)^2 \frac{dr}{dt} P(t) dt \quad (6.24)$$

*Light emission*

$$E_{\text{light}}(t) = \int_0^t 4\pi r(t)^2 \zeta \eta T^4 dt \quad (6.25)$$

The electric energy deposited in the discharge in the form of Joule heating is represented in the model as Equation (6.26). This representation allows modelling of the energy deposition into the discharge by knowing the basic characteristics of the arc discharge: arc current (fitting parameters of the sinusoidal damped current waveform,  $I_0$ ,  $\omega$ , and  $\zeta$ ) and the equivalent constant plasma resistance,  $R_{\text{eqarc}}$  (following the constant approach analysis presented in Subchapter 5.4).

*Electric arc energy*

$$E_{\text{arc}}(t) = \int_0^t R_{\text{eqarc}} (I_0 e^{-\zeta t} \sin \omega t)^2 dt \quad (6.26)$$

### 6.3.1 Energy partition in SBSG topology

Figure 6.2 presents typical waveforms obtained for the radius, velocity and internal pressure of the arc plasma channel for a 0.5 mm wire-guided discharge and 1.9 nF capacitor in the SBSG topology (no wire that shorts the spark gap). According to literature, during the phenomenon development, internal pressure builds up to several GPa in the plasma column of the electrical discharge [TMG+08]. Moreover, expansion velocities of the phenomenon can reach 100 m/s – 1000 m/s in water [TMG+08]. Smaller ranges of internal pressure were recorded in the case of the sub-mm SBSG lengths in air. Similar ranges of velocities (even larger) were recorded in the case of the expansion of the electrical discharge in the air. The transient electrical discharge radiates intense acoustic pressure pulses which propagate into the surrounding liquid medium at the local speed of sound, in this case speed of sound in air. The local speed of sound depends on the temperature. In the present model the temperature is considered constant, thus, the speed of sound is considered constant. At the end of the energy deposition phase, the value of the arc plasma channel radius is of the order of less than 1 mm. Velocities of expansion of the arc of a few km/s were obtained. Even at the end of the energy deposition stage, the velocity of the arc plasma channel is above the speed of sound. Moreover, the internal pressure developed within the arc plasma channel can reach extremely high values, of the order of several tens of MPa, especially in the very early stages. During the evolution of the phenomenon, the internal pressure of the plasma channel decreases rapidly until it becomes equal to the normal atmospheric pressure when the expansion of the plasma channel ceases. Table 6.1 summarises the input parameters used in the analytical model developed for the thesis in this subchapter.

**Table 6.1** Model input parameters used in the simulations for the analytical model developed for the thesis. The case examined is 1.9 nF capacitor and 0.5 mm inter-electrode spark gap length.

Model input parameters	Thesis analytical model
$c_{pv}$	1.4
$\rho_0$	1.204 kg/m <sup>3</sup>
$P_0$	101,325 Pa
$r(0)$	10 <sup>-6</sup> m
$dr(0)/dt$	10 <sup>-6</sup> m/s
$R_{eqarc}$	2.01 $\Omega$
$\omega$	63,343,971.4 rad/s
$\zeta$	16,929,287.5 rad/s
$I_0$	258.2 A
$\eta$	5.67·10 <sup>-8</sup> W/m <sup>2</sup> K <sup>4</sup>
$\xi$	0.1
$T$	7,000 K

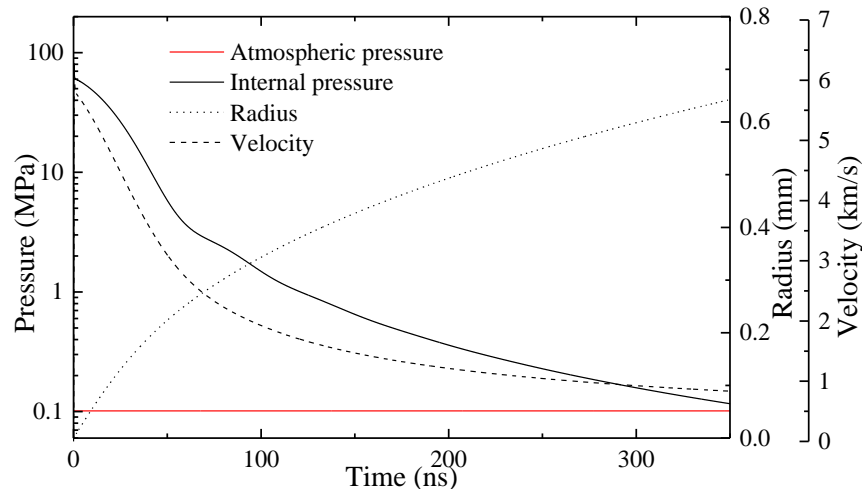


**Figure 6.2** Temporal development of arc plasma channel radius,  $r(t)$ , channel expansion velocity, and pressure in the arc plasma channel,  $P(t)$ , for 0.5 mm SBSG discharge.

Figure 6.3 presents the mechanical work done by the expanding arc plasma channel, the internal energy stored in the gas, and the light emission as a function of time. These three energy components were calculated using equations (6.23) to (6.26). It can be observed that, at the very beginning of the discharge, the main portion of the electrical energy is converted into the internal energy of the gas. However, the mechanical work component quickly becomes significant. During the evolution of the discharge, the electrical energy partitions mainly into the mechanical work and internal energy. Losses due to light emission, which are constant due to the constant temperature assumption, are significantly smaller than the aforementioned energies.

The internal energy of the plasma channel is calculated using Equation (6.23) and is shown in Figure 6.3(b). The value of the internal energy at each instant of time is the product of the pressure and the volume of the system at each instant of time. Thus, the variations of the internal energy can be explained by the variations of the volume and pressure. During the analysis, the calculated radius presents an increase. However, the calculated pressure decreases. Despite the increasing radius being cubed, the large decrease of the pressure is more dominant. Therefore, the calculated internal energy after approximately 50 ns of the analysis decreases.



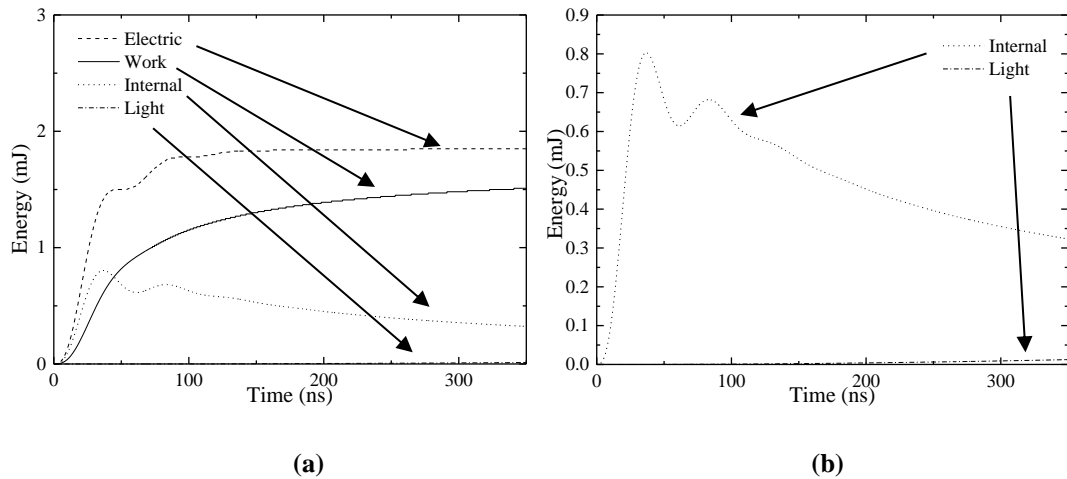


**Figure 6.3** (a) Temporal development of energy partition in a 0.5 mm SBSG discharge, (b) zoom in the graph showing only the internal energy and the light emission.

Pressure, thermal energy and light emission with significant ultraviolet and infrared components, developed due to the mechanical work, the internal energy and the radiant energy, respectively, could potentially cause harm to personnel and damage power equipment in the vicinity of the arcing event. From a safety point of view, it is crucial to define protection boundaries for each of the potential hazards derived from the arc discharge.

Figure 6.4 shows the energy partition as a function of the total electric energy deposited in the discharge. All energy components: internal energy, mechanical energy and light emission energy, shown in Figure 6.4 represent the maximum values of these energies obtained in the simulations for each specific inter-electrode WGSG length. An example of the energy partition in the case of a 0.5-mm discharge is given in Figure 6.3, which corresponds to a single set of data points at ~1.85 mJ in Figure 6.4.

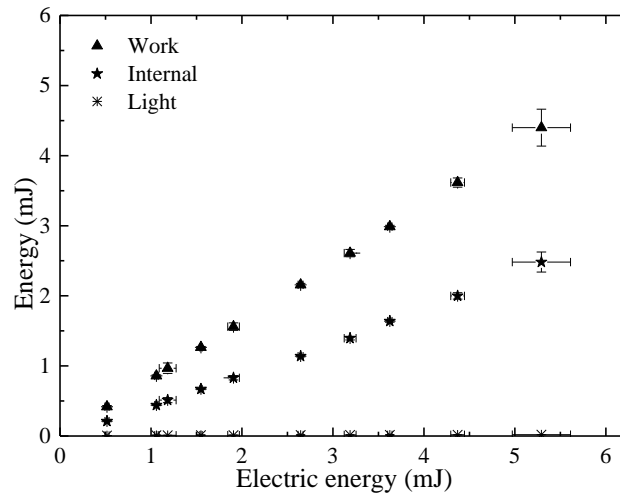


**Figure 6.4** Energy partition as a function of electrical energy deposited into the plasma discharge (SBSG). Data points correspond to the maximum value of energy. The error bars represent standard deviation with respect to each axis.

It was obtained that approximately 71.2% of the electric energy is converted into mechanical work, subsequently contributing to the pressure rise. The rest of the electric energy is converted into the internal energy of the gas, and afterwards into thermal energy. A portion of the electric energy which is converted into radiant energy ( $\sim 0.3\%$ ) is substantially smaller than other energy components. The model has assumed that heat conduction is not significant during the formation and expansion of the arc.

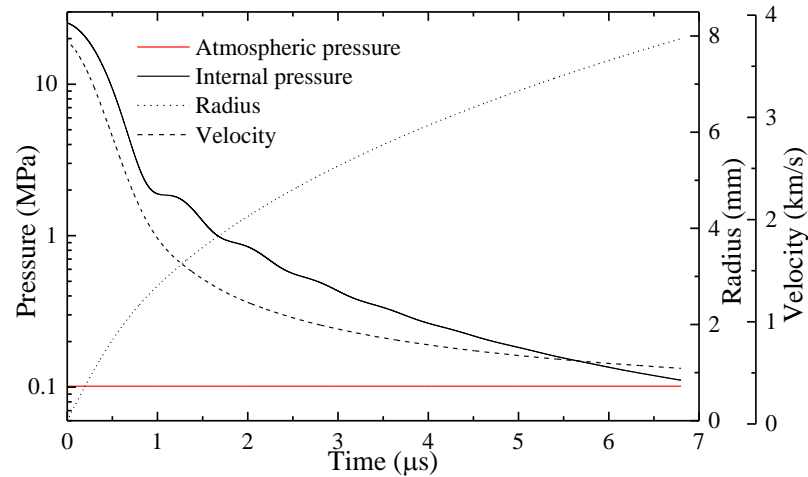
### 6.3.2 Energy partition in WGS topology

Figure 6.5 presents typical waveforms obtained for the radius, velocity and internal pressure of the arc plasma channel for a 3-cm wire-guided discharge and 80 nF capacitor in the WGS topology. Table 6.2 summarises the input parameters used in the analytical model developed for the thesis in this subchapter.

**Table 6.2** Model input parameters used in the analytical model developed in the thesis. The case examined is 80 nF capacitor and 3 cm inter-electrode spark gap length.

Model input parameters	Thesis analytical model
$c_{pv}$	1.4
$\rho_0$	1.204 kg/m <sup>3</sup>
$P_0$	101,325 Pa
$r(0)$	10 <sup>-6</sup> m
$dr(0)/dt$	10 <sup>-6</sup> m/s
$R_{eqarc}$	0.4386 $\Omega$
$\omega$	4,168,457.2 rad/s
$\zeta$	531,139.3 rad/s
$I_0$	2,712.9 A
$\eta$	5.67·10 <sup>-8</sup> W/m <sup>2</sup> K <sup>4</sup>
$\xi$	0.1
$T$	7,000 K

At the end of the energy deposition phase, the value of the arc plasma channel radius is of the order of several mm. The obtained velocities of expansion of the arc are of a few km/s. Even at the end of the energy deposition stage, the calculated velocity of the arc plasma channel is higher than the speed of sound. Moreover, the internal pressure developed within the arc plasma channel can reach extremely high values, of the order of tens of MPa, especially in the very early stages. During the evolution of the phenomenon, the internal pressure of the plasma channel decreases rapidly until it becomes equal to the normal atmospheric pressure when the expansion of the plasma channel ceases.



**Figure 6.5** Temporal development of arc plasma channel radius,  $r(t)$ , velocity, and pressure in the arc plasma channel,  $P(t)$ , for 3 cm wire-guided discharge.

Figure 6.6 presents the mechanical work done by the expanding arc plasma channel as a function of time, the internal energy stored in the gas, and light emission. These three energy components were calculated using equations (6.23) to (6.26). It can be observed that, at the very beginning of the discharge, the main portion of the electrical energy is converted into the internal energy of the gas. However, the mechanical work component quickly becomes significant. During the evolution of the discharge, the electrical energy partitions mainly into the mechanical work and internal energy. Losses due to light emission are significantly smaller than the aforementioned energies.

The internal energy of the plasma channel is calculated using Equation (6.23) and is shown in Figure 6.6(b). The value of the internal energy at each instant of time is the product of the pressure and the volume of the system at each instant of time. Thus, the variations of the internal energy can be explained by the variations of the volume and pressure. During the analysis, the calculated radius presents an increase while the calculated pressure decreases. In the present analysis, the decrease of the pressure and the increase of the radius result to a less prominent decrease of the internal energy than the one presented for the SBSG.

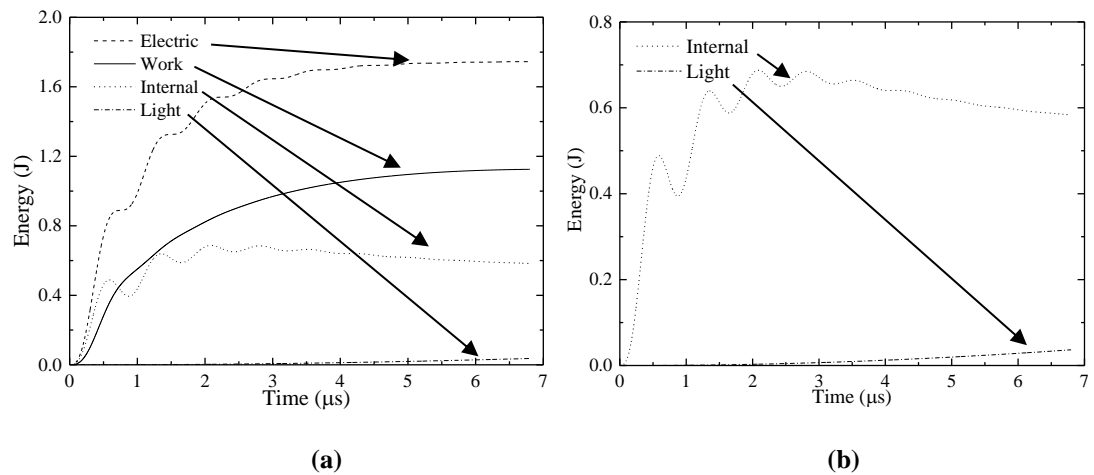


**Figure 6.6** (a) Temporal development of energy partition in a 3 cm wire-guided discharge (b) zoom in the graph showing only the internal energy and the light emission.

Figure 6.7 shows the energy partition as a function of the total electric energy deposited in the discharge. All energy components: internal energy, mechanical energy and light emission energy, shown in Figure 6.7 represent the maximum values of these energies obtained in the simulations for each specific inter-electrode WGSG length. An example of the energy partition in the case of a 3-cm discharge is given in Figure 6.6, which corresponds to a single set of data points at  $\sim 1.75$  J in Figure 6.7.

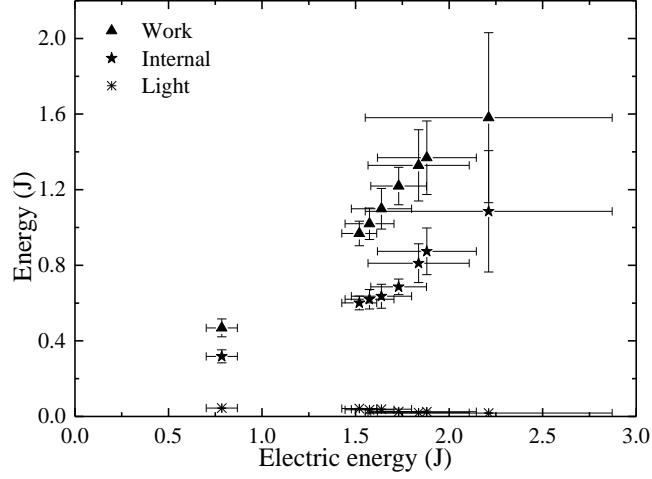


**Figure 6.7** Energy partition as a function of electrical energy deposited into the plasma discharge (WGS). Data points correspond to the maximum value of energy. The error bars represent standard deviation with respect to each axis.

It was obtained that approximately 65.5% of the electric energy is converted into mechanical work, subsequently contributing to the pressure rise. The rest of the electric energy is converted into the internal energy of the gas, and afterwards into thermal energy. A portion of the electric energy which is converted into radiant energy (~1%) is substantially smaller than other energy components. The model has assumed that heat conduction is not significant during the formation and expansion of the arc.

### 6.3.3 Acoustic pressure approximation

The acoustic pressure,  $P_{ac}$  (the pressure in the radiated acoustic impulse), was obtained using the acoustic approximation. The pressure wave is assumed to be a compression wave that propagates in air at the speed of sound,  $c$ , transmission losses are neglected, and its measured value at a certain distance away from the plasma discharge source,  $\chi$ , is given by Equation (6.27), where  $\tau$  is the retarded time  $\tau = t - \chi/c$ :

$$P_{ac} = P_0 + \rho_0 \left\{ \frac{1}{\chi} \left( r(\tau)^2 \frac{d^2 r(\tau)}{d\tau^2} + 2r(\tau) \left( \frac{dr(\tau)}{d\tau} \right)^2 \right) - \frac{r(\tau)^4}{2\chi^4} \left( \frac{dr(\tau)}{d\tau} \right)^2 \right\} \quad (6.27)$$

Figure 6.8 presents the temporal acoustic pressure wave,  $P_{ac}$ , for 7 different distances away from the discharge. It can be seen that, during the first  $\mu\text{s}$  for the SBSG, and the first 50 ns

for the WSGG the pressure pulse reaches its maximum value and then gradually decreases over time until the time that it gets equal to the atmospheric pressure. The graph shows the duration of the discharge. However, it can be seen that, especially for distances very close to the discharge, the pressure still has a value greater than the atmospheric pressure even after the end of the electrical energy deposition phase (which is considered to define the duration of the discharge).

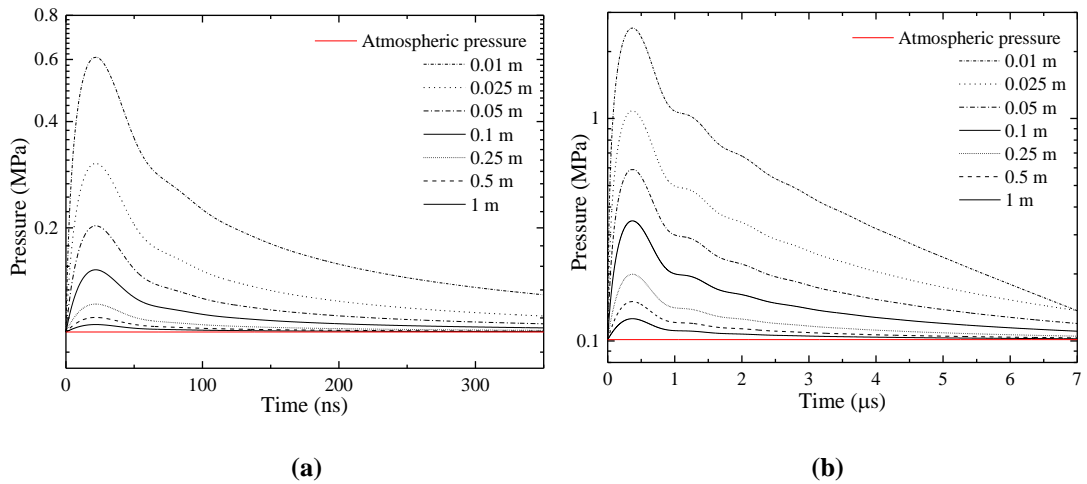


**Figure 6.8** Temporal development (retarded time axis) of the acoustic pressure wave developed at 7 different distances away from the discharge. **(a)** 1.9 nF capacitor and 0.5 mm inter-electrode spark gap length in the SBSG topology and **(b)** 80 nF capacitor and 3 cm inter-electrode spark gap length in the WSGG topology.

Figure 6.9 presents the acoustic pressure,  $P_{ac}$ , as a function of  $\chi$  from the plasma discharge for all tested plasma arc lengths. It is expected from the literature that the pressure should decrease rapidly as the distance from the spark plasma discharge increases: the pressure waveform is expected to follow a power allometric law,  $P_{ac}(\chi) \propto \chi^{-2}$ , [TFG+06], [NR71]. In the present model, the pressure decreases rapidly and seems to follow a hyperbolic form. The pressure levels developed are dependent on the WSGG/SBSG length and specific energy available in the discharge. However, this dependence is only evident at distances which are very close to the discharge. For longer distances, the peak pressure in the pressure impulse is independent of the energy deposition. In the given experimental conditions, the pressure developed at ~50 cm away from the discharge does not exceed 200 kPa, and the pressure is essentially equal to the normal atmospheric pressure for longer distances, 1 m and above.

Figure 6.9 is showing the temporal development of the pressure wave developed at 7 different distances away from the discharge.

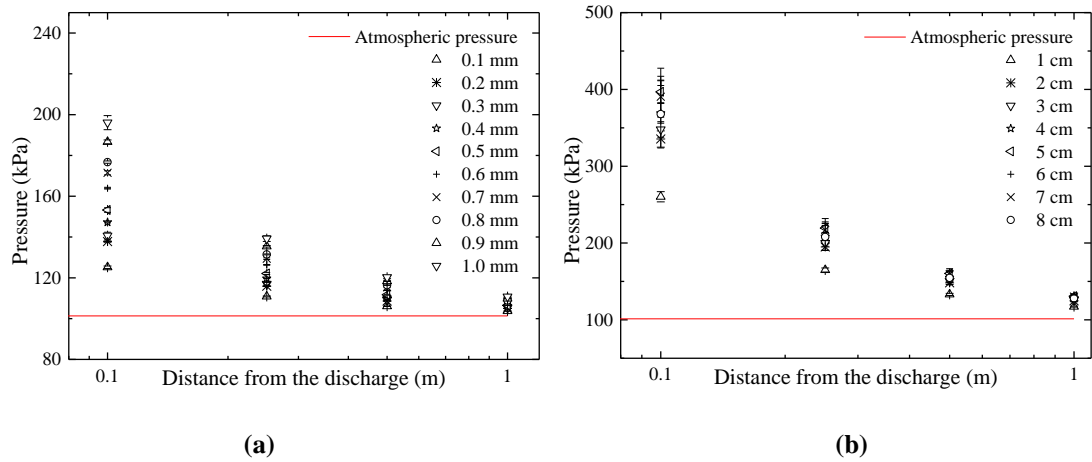


**Figure 6.9** Acoustic pressure wave as a function of distance from the discharge. The error bars represent standard deviation. (a) 1.9 nF capacitor and 0.5 mm inter-electrode spark gap length in the SBSG topology and (b) 80 nF capacitor and 3 cm inter-electrode spark gap length in the WGSG topology.

## 6.4 Shock-wave approximation

Previously research on the topic of the arc plasma channel dynamics has shown that the temporal development of the arc plasma channel discharge can be approximated with the shock-wave theory. The shock-wave is a propagating disturbance that moves faster than the speed of sound in a fluid and carries energy in the form of wave. It is characterised by an abrupt, nearly discontinuous change in the pressure, temperature and density of the medium, flow velocity and Mach number. Moreover, the energy of the shock-wave dissipates relatively quickly with distance.

An accompanying expansion wave approaches and eventually merges with the shock-wave and partially cancels it out. Actually, the shock-wave is the fact that, at the region where this occurs, the flow of the disturbance reaches a point where they cannot travel any further upstream and pressure progressively builds in that region and a high-pressure shock-wave rapidly forms [CF85], [TBI+07].

Drabkina originally indicated that the rapid development of an arc channel can be accounted by the excitation of a shock-wave [Dra51]. Braginskii developed a theory for gases in which the outer boundary of the channel is described as a piston that pushes the surrounding



medium in such a way as to establish a shock-wave [Bra58], [Ham95]. Braginskii used the assumption of a steady shock-wave (the particle velocity does not vary over the region between the channel boundary and the shock front) and determined the pressure in the channel at the boundary, Equation (6.28), where  $K_p$  is the resistance coefficient which was determined as 0.9 using the equations of mass, momentum and energy conservation and  $\rho_0 = 1.2$  (the density of air).

$$P(t) = K_p \rho_0 \left( \frac{dr}{dt} \right)^2 = 0.9 \cdot 1.2 \left( \frac{dr}{dt} \right)^2 \approx \left( \frac{dr}{dt} \right)^2 \quad (6.28)$$

Braginskii assumed that the electrical energy separates into mechanical work and internal energy of the gas, Equation (6.29). Differentiation of both sides of Equation (6.29) results in Equation (6.30).

$$\frac{P(t)\Omega(t)}{c_{pv} - 1} + \int_0^\Omega P(t) d\Omega = \int_0^t I_{\text{arc}}(t)^2 R_{\text{eqarc}} dt \quad (6.29)$$

$$\frac{dP}{dt} \frac{c_{pv}\Omega(t)}{c_{pv} - 1} + \frac{d\Omega}{dt} \frac{P(t)}{c_{pv} - 1} + P(t) \frac{d\Omega}{dt} = I_{\text{arc}}(t)^2 R_{\text{eqarc}} \quad (6.30)$$

By substituting Equation (6.28) in Equation (6.30), a combined differential and integral equation is formed which presents the arc channel radius expression, Equation (6.31).

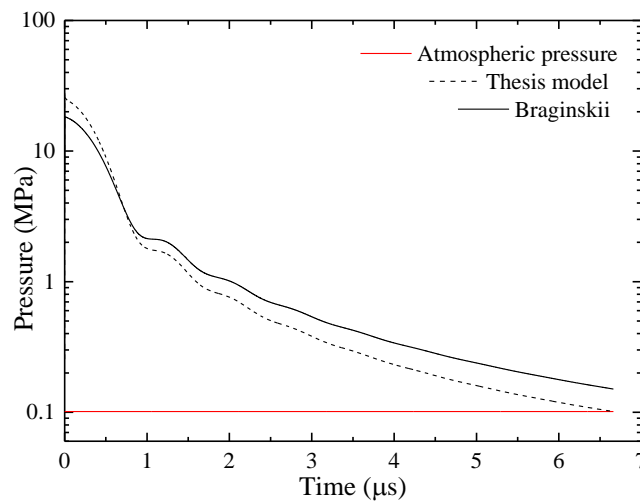
$$\begin{aligned} \frac{8}{3} \frac{dr}{dt} \frac{d^2 r}{dt^2} \frac{\pi K_p \rho_0 r^3}{c_{pv} - 1} + \left( \frac{dr}{dt} \right)^3 \frac{4\pi K_p \rho_0 r^2}{c_{pv} - 1} + \left( \frac{dr}{dt} \right)^3 4\pi K_p \rho_0 r^2 &= I_{\text{arc}}(t)^2 R_{\text{eqarc}} \\ \frac{d^2 r}{dt^2} &= \frac{3 I_{\text{arc}}(t)^2 R_{\text{eqarc}} (c_{pv} - 1)}{8 \pi K_p \rho_0 r^3 \frac{dr}{dt}} - \frac{3}{2r} \left( \frac{dr}{dt} \right)^2 - \frac{3(c_{pv} - 1)}{2r} \left( \frac{dr}{dt} \right)^2 \\ \frac{d^2 r}{dt^2} &= \frac{3 I_{\text{arc}}(t)^2 R_{\text{eqarc}} (c_{pv} - 1)}{8 \pi K_p \rho_0 r^3 \frac{dr}{dt}} - \frac{3c_{pv}}{2r} \left( \frac{dr}{dt} \right)^2 \end{aligned} \quad (6.31)$$

Table 6.3 summarises the input parameters used in the two models specific in this subchapter. It should be highlighted that the Braginskii model refers to two energy components, the internal energy and the mechanical work done by the expanding plasma channel radius. The analytical model developed in the present thesis refers to three energy components: the internal energy, the mechanical work done by the expanding plasma channel radius and the light emission. Since, the light emission is not a significant portion of the total energy; this energy contribution will not be taken into further consideration for the needs of the present verification process.

**Table 6.3** Model input parameters used in the simulations for Braginskii model and the analytical model developed for the thesis. The case examined is 80 nF capacitor and 3 cm inter-electrode spark gap length.

Model input parameters	Braginskii	Thesis analytical model
$K_p$	0.9	-
$c_{pv}$		1.4
$\rho_0$		1.204 kg/m <sup>3</sup>
$P_0$	-	101,325 Pa
$r(0)$		10 <sup>-6</sup> m
$dr(0)/dt$		10 <sup>-6</sup> m/s
$R_{eqarc}$		0.4386 $\Omega$
$\omega$		4,168,457.2 rad/s
$\zeta$		531,139.3 rad/s
$I_0$		2,712.9 A
$\eta$	-	5.67·10 <sup>-8</sup> W/m <sup>2</sup> K <sup>4</sup>
$\xi$	-	0.1
$T$	-	7,000 K

Using the aforementioned input parameters which correspond to 80 nF capacitor and 3 cm inter-electrode spark gap length, comparison of the Braginskii and the original analytical model developed for the thesis is conducted. Figure 6.10 presents the arc plasma channel pressure obtained using both approaches. As it can be seen, the two models demonstrate very similar behaviour in terms of how the pressure builds up and develops. Both models present pressure levels which are several times higher than the atmospheric pressure, especially at the early stage of the arc discharge. Figure 6.11(a) and (b) presents comparison of radii and velocities obtained using both models. Again, it is evident that both models produce very similar results. Figure 6.12(a) presents internal energy comparison for the two models and Figure 6.12(b) work comparison for the two models. Electrical energy comparison for the two models is given in Figure 6.13.



**Figure 6.10** Pressure level comparison for the two models.

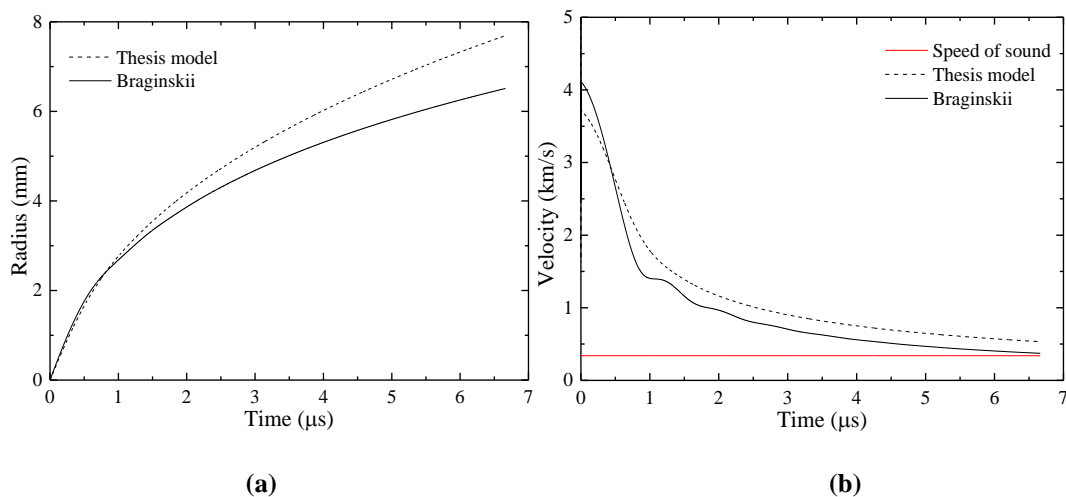


**Figure 6.11** (a) Radius level comparison for the two models and (b) velocity level comparison for the two models.

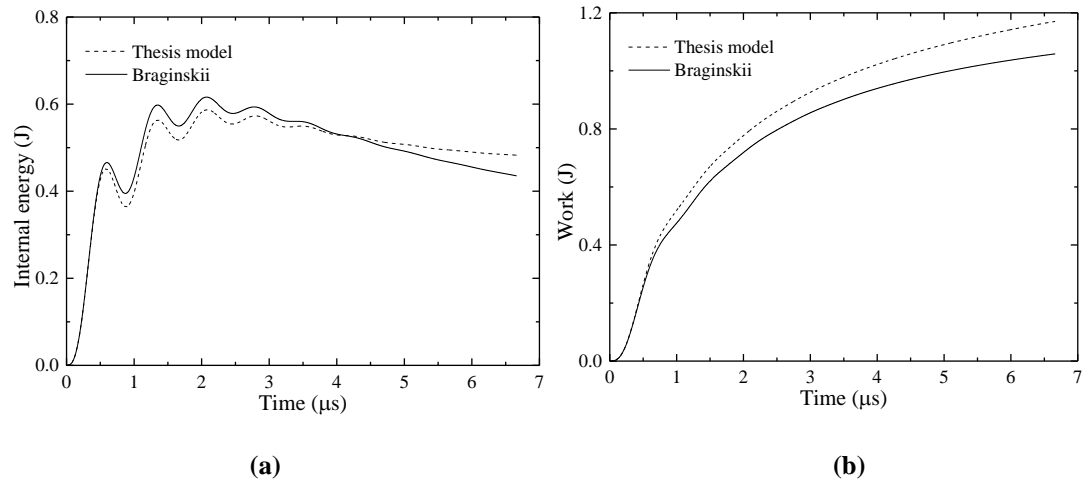


**Figure 6.12** (a) Internal energy comparison for the two models and (b) work comparison for the two models.

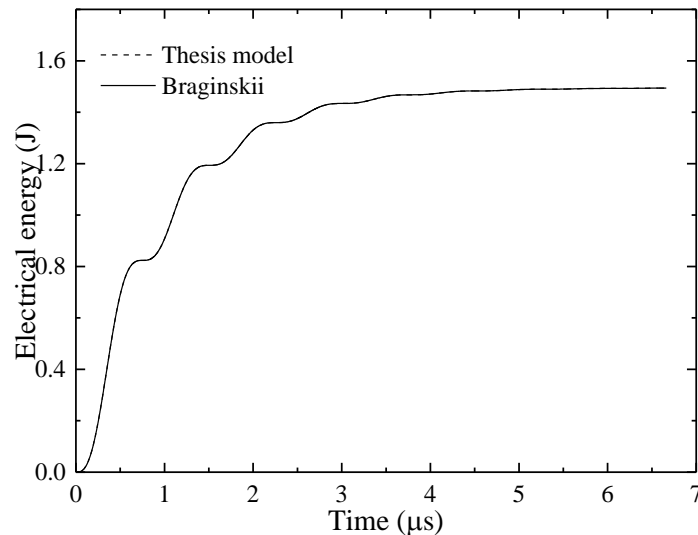


**Figure 6.13** Electric energy comparison for the two models (waveforms coincide).

## 6.5 Conclusions

In Chapter 6, the energy partition during the initiation phase of the arc fault was investigated. An analytical model has been developed on the basis of hydrodynamic theory. This novel model has been developed, presented and discussed in this chapter. The analytical model is the primary focus of the thesis. Using the developed model, the energy components associated with thermal, acoustic-kinetic and light emission processes during arc initiation have been obtained for the case of the SBSG and the WGS. These two ways of arc

initiation was found to exhibit similar behaviour characteristics. In both cases, the bulk energy was converted to internal energy and mechanical work due to the expansion of the arc plasma channel. The portion of the light emission is significantly smaller than the other two components, it is almost negligible.

Specifically, for a typical SBSG discharge, it was obtained that:

- ~71.2 % of the electric energy transforms into work
- ~28.5 % of the electric energy transforms into internal energy
- ~0.3 % of the electric energy transforms into light emission

For a typical WGSg discharge, it was found that:

- ~65.5 % of the electric energy transforms into work
- ~33.5 % of the electric energy transforms into internal energy
- ~1 % of the electric energy transforms into light emission

Similar energy partition percentages are observed for all the individual discharges created in the SBSG and the WGSg topologies.

As discussed previously, the energy partition follows similar trends for the two ways of the arc initiation. It was observed that, at the very beginning of the discharge, the main portion of the electrical energy is converted into the internal energy of the gas. However, the mechanical work component quickly becomes significant. During the evolution of the discharge, the electric energy partitions mainly into the mechanical work and internal energy. Losses due to light emission are significantly smaller than the aforementioned energies. This behaviour was exhibited for both ways of arc initiation.

The important role in the energy partition process plays the duration of the energy deposition phase. Thus, the longer the energy deposition phase is, the longer the internal energy and the mechanical work will have their maximums.

Finally, verification of the present model was performed through comparison with the model developed by Braginskii based on the shock-wave theory. The results obtained for the two ways of the arc initiation were very similar, thus the model developed for the thesis can readily describe the development of the phenomenon. The assumption made that the disturbance is not a shock-wave does not influence much the expected results.

## Chapter 7

---

# Black-box approach to modelling the initial stage of arc

Chapter 7 is focused on the analysis of application of the arc black-box models of Mayr and Cassie to the transient arc discharge processes investigated in the present work. It is proposed to use the obtained current and voltage waveforms as initial conditions in the Mayr and Cassie models of arc discharges. Thus, the developed transient model and the classic black-box models can potentially be used for accurate description of practical arc discharges. In order to develop this unified approach, the recorded voltage and current waveforms (used also in Chapter 5) have been analysed in the framework of Mayr and Cassie approaches. A discussion on the arc models with emphasis given in the black-box models is provided in Subchapter 7.1. The developed combined models and the results of simulations performed utilising these models are presented in Subchapter 7.2. Simulations results are discussed and analysed. Conclusions on the arc-electrical circuit interaction are given in Subchapter 7.3 and further considerations are raised for subsequent research.

### 7.1 Arc models

Accurate simulation of the arc behaviour is of great technical importance, especially for the circuit breakers research [Cigre93]. Arc properties, mainly their non-linearity and their transient nature, can be useful for certain applications, such as gas filled spark gaps. However, they can also be troublesome when they appear unexpectedly, such as electrical arcing faults [Bro55]. Physical electric arc models developed to describe arc behaviour and properties can be separated in two wide categories [MPS13], [Wal13], [LBR17]:

- **Physical models:** based on fluid dynamics equations, laws of thermodynamics and Maxwell's equations.

- **Mathematical models:** which are phenomenological models, often simple descriptions of a single process of the arc behaviour based on mathematical equations relating arc electrical parameters. “**Black-box models**” term can be used to describe these models.

### 7.1.1 Physical arc models

Fluid dynamics and thermodynamics laws combined with Maxwell’s equations are used to form differential equations describing the behaviour of the arc. Arc physical models are quite complex models with a high accuracy and they can be used for example, in the design phase of a circuit breaker. However, for the purposes of this study, there is no need for employing the complex physical model to predict the arc behaviour. Instead, the analysis will be conducted using the black-box arc models. The reasons for selection of such approach are explained in Subchapter 7.1.2.

### 7.1.2 Mathematical black-box arc models

A differential equation can describe the temporal arc behaviour as a part of an electrical circuit, only partly based on physical considerations. The most basic well-known black-box arc models are the Cassie and Mayr models [May43], [Cas39], [Cigre93], [OIT+10]. There are also several other arc models that are derived as either modifications or extensions of the classic Mayr and Cassie models, for example [SS00], [SK00], [Hab88].

The mathematical model is developed based on the energy balance equation. The arc conductance,  $G$ , can be expressed as a function of the stored energy,  $Q_e$ , Equation (7.1), which is the excess energy resulting from the deduction of the energy losses,  $Q_L$ , from the electrical power input,  $Q_I$ , [Bro55].

$$G = f(Q_e) = f(Q_I, Q_L) \quad (7.1)$$

The general differential equation for  $G$  expressing the macroscopic arc properties is given in Equation (7.2).

$$\frac{1}{G} \frac{\partial G}{\partial t} = \frac{1}{\tau_{MC}} \left( \frac{V_{arc} I_{arc}}{P_{MC}} - 1 \right) \quad (7.2)$$

$V_{\text{arc}}$  : arc voltage [V]

$I_{\text{arc}}$  : arc current [A]

$P_{\text{MC}}$  : general arc parameter depending on  $G$  and  $I_{\text{arc}}$  determined empirically [VA]

$\tau_{\text{MC}}$  : general arc parameter depending on  $G$  and  $I_{\text{arc}}$  determined empirically [s]

Cassie and Mayr developed their specific models based on the differential equation (7.2) applying additional assumptions.

### 7.1.2.1 Mayr arc model

The assumptions made in the Mayr's model are:

- The rate of energy loss caused by thermal conduction from the arc to environment is constant.
- The cross-section area of the arc is assumed constant.
- The arc conductance is dependent on the temperature and on the change of ionisation degree.

Equation (7.3) expresses the Mayr model [May43], [Bro55] which is generally used for currents near zero or low currents and is most suitable for low temperature arcs up to 8000 K.

$$\frac{dG}{dt} = \frac{I_{\text{arc}}^2}{P_{\text{M}}\tau_{\text{M}}} - \frac{G}{\tau_{\text{M}}} \quad (7.3)$$

$P_{\text{M}}$  : arc parameter for Mayr model [W]

$\tau_{\text{M}}$  : arc parameter for Mayr model [s]

### 7.1.2.2 Cassie arc model

The assumptions made in the Cassie's model are:

- The voltage over the duration of the arc is constant.
- The arc has a fixed temperature being cooled by forced convection.



- The cross-section area of the arc is proportional to the current.
- The arc conductance is dependent on the arc diameter.

Equation (7.4) expresses the Cassie model [Cas39] which generally is used around the current maximum point or high current and is most suitable for high temperature arcs over 8000 K.

$$\frac{dG}{dt} = \frac{I_{\text{arc}}^2}{U_C \tau_C G} - \frac{G}{\tau_C} \quad (7.4)$$

$U_C$  : arc parameter for Cassie model [V<sup>2</sup>]

$\tau_C$  : arc parameter for Cassie model [s]

### 7.1.3 Limitations of black-box models

Black-box models have been well developed and used especially in the field of circuit-breakers. More specifically, the models are used to capture the behaviour of a circuit breaker interrupting a short-line fault. Due to their popularity, they have been implemented in software packages used in industry and academia [Matlab] allowing the user to incorporate them into a certain range of electrical power systems. Limited research on the implementation of the black-box models in other areas such as arcs within cables [LBR17] have been presented to date.

The most challenging part of the black-box model analysis is the determination of the arc parameters that is based on the measured voltage and current arc waveforms [Cigre93], [Wal13]. Although there are arc parameters available in the literature, they are suitable only for the specific circuit configuration they were calculated for. For a different circuit configuration, new arc parameters need to be defined since the arc parameters are strongly depended on the network elements [Cigre93]. Thus, multiple limitations exist on the range of altered circuit conditions in which the models can be used to extrapolate experimental results and predict the arc-circuit interaction. It has been reported [Cigre93] that implementing the model within a circuit with altered peak current magnitude, without re-defining new arc parameters, lead to questionable results.

### 7.1.4 Research contributions

The focus of the present chapter is the determination of the black-box additional parameters for the experimental set-up used in this research. The set-up (WGSG) (see Subchapter 4.1.4) is a capacitive energy storage circuit with a PCS and a wire-guided spark gap. Using Mayr and Cassie models, the aim is to predict arc current and voltage of the probe waveforms. The main contribution of this chapter is in the analysis and evaluation of the suitability of black-box models for predicting the arc-circuit interaction:

- Within a capacitive circuit; research to date has been focused on AC power system topologies.
- At the arc initiation stage with duration of a few  $\mu\text{s}$ ; (to date black-box models have been used for investigation of the arc behaviour within a time range of ms and longer).

This is an initial step towards establishment of the complete accurate link between arc initiation and its evolution, which is not a trivial task. Since the energy partition analysis during arc initiation has been performed (see Chapter 6), when the link between arc initiation and evolution will be established, it could facilitate prediction of the energy partition during arc's full development. There are many challenges related to the black-box approach application which are discussed in the rest of the chapter.

## 7.2 Model and simulations

Analysis of the circuit with capacitive energy storage and with the PCS and the wire-guided spark gap (WGSG) has been performed to develop the model in MATLAB/Simulink software. The resulting ordinary differential equation (ODE) describing the circuit behaviour along with the suggested modified ODE (for the Mayr model see Equation (7.3) and for the Cassie model see Equation (7.4)) are solved with stiff solver that is suitable for solving highly non-linear problems.

The suggested modified Mayr's and Cassie's ODEs do not express the arc conductance. In the present modelling approach, it is assumed that both equations can be used to express the ratio between the arc current,  $I_{\text{arc}}$ , over the voltage of the probe,  $V_{\text{probe}}$ . Thus, a step by step calculation of the ratio of the arc current over the voltage of the probe is achieved.

The circuit analysis is presented in Subchapter 7.2.1 and derivation of the waveform of the experimental ratio of the arc current over the voltage of the probe is described in Subchapter 7.2.2. Thereafter, simulations results are presented in Subchapter 7.2.3 and 7.2.4 for Mayr and Cassie model, respectively. Finally, conclusions and further research considerations are discussed in Subchapter 7.3.

## 7.2.1 Circuit analysis

The experimental WGSG topology, with a 4-mm PCS, a 3-cm wire-guided spark gap and 80 nF capacitor has been considered in the analysis. The simplified circuit of the topology is presented in Figure 7.1. The capacitor is charged before breakdown.

The loop total inductance was calculated using the formulas from [Gro04] (see Subchapter 5.1.2.2) and found to be 710 nH. This value has been used as a first approximation of the assumed inductance of the yellow highlighted branch of the circuit, shown in Figure 7.1. Thus, the yellow highlighted branch of the circuit is considered to have 710 nH inductance. The shunt resistance is assumed to be  $\sim 0 \Omega$  and the yellow highlighted branch resistance is assumed  $\sim 0.3 \Omega$ . The green highlighted branch of the circuit is consisted of the PCS and the WGSG. This branch has an inductive and resistive character. However, for the present analysis, no further separation between the inductive and resistive voltage parts will be conducted. The branch behaviour will be reported using the acquired voltage probe waveform without further data processing.

Equation (7.5) describes the transient process in the circuit. The ODE gives the arc current time derivative,  $dI_{\text{arc}}/dt$ , as a function of the resistive,  $R$ , inductive,  $L$ , and capacitive,  $C$ , circuit elements and the voltage of the probe,  $V_{\text{probe}}$ .

$$\begin{aligned}
 V_c &= V_L + V_R + V_{\text{probe}} \Rightarrow \\
 V_c(0) - \frac{1}{C} \int_0^t I_{\text{arc}}(t) dt &= L \frac{dI_{\text{arc}}}{dt} + RI_{\text{arc}} + V_{\text{probe}} \Rightarrow \\
 \frac{dI_{\text{arc}}}{dt} &= \frac{V_c(0)}{L} - \frac{1}{CL} \int_0^t I_{\text{arc}}(t) dt - \frac{R}{L} I_{\text{arc}} - \frac{V_{\text{probe}}}{L}
 \end{aligned} \tag{7.5}$$

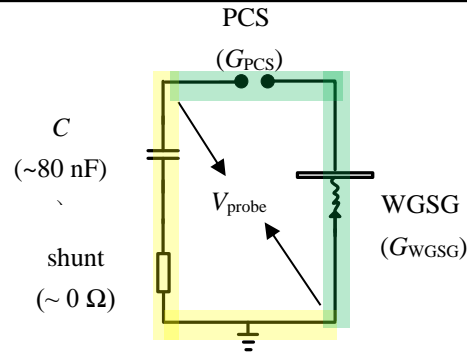


**Figure 7.1** The WGSG topology, with the 4-mm PCS, the 3-cm wire-guided spark gap and the 80 nF capacitor.

## 7.2.2 Ratio of experimental arc current over voltage of the probe waveform calculation using experimental results

The current,  $I_{\text{arc}}$ , and the voltage waveforms,  $V_{\text{probe}}$ , obtained experimentally for the topology presented in Figure 7.1 are re-produced in Figure 7.2(a) and Figure 7.2(b). Based on these waveforms, the experimental ratio waveform of the arc current over the voltage of the probe,  $I_{\text{arc}}/V_{\text{probe}}$ , has been calculated and presented in Figure 7.3.

Unlike in Chapter 5 and Chapter 6, no smoothing or further time alignment of the acquired voltage and current waveforms has been performed. Raw data used as reference waveforms for qualitative investigation of suitability of black-box models for describing arc-circuit behaviour within the experimental topology.

As mentioned before, no further separation between the voltage inductive and resistive parts is conducted. Since, it is the first attempt to simulate arc-circuit interaction within the specified experimental conditions, it is decided to accept this approach, sacrificing investigation of the arc conductance.

The research is intended to continue in the future, focusing on the arc conductance specifically to produce higher validity results compared to the present approach. It should be stressed, though, that as a first bulk approximation of the behaviour of the branch in which the arc is created, the results obtained open a new promising pathway for future research.

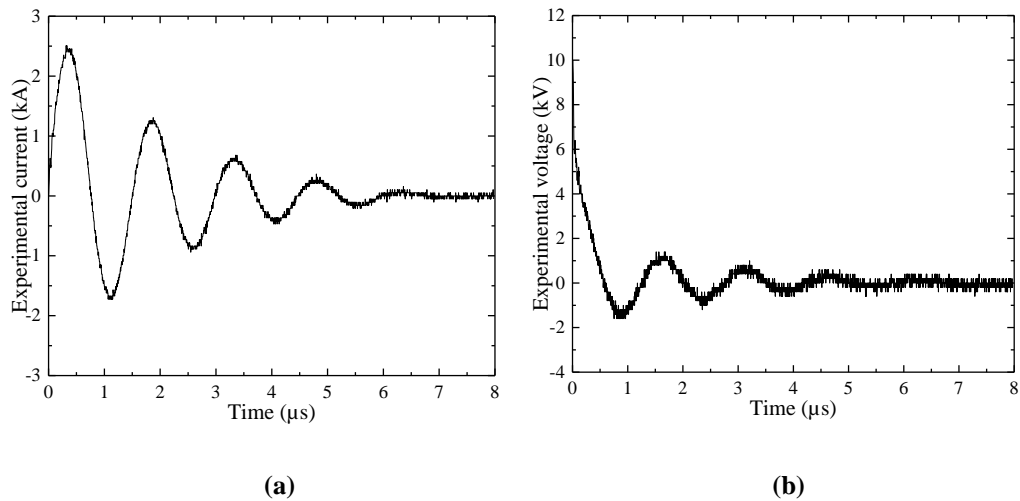


**Figure 7.2** Experimental arc current (a) and voltage of the probe (b) waveforms.

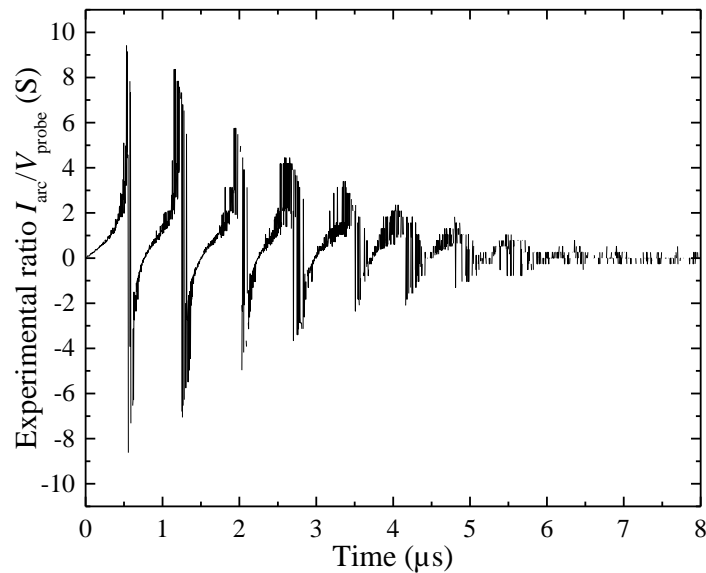


**Figure 7.3** Ratio of experimental arc voltage over voltage of the probe waveform.

### 7.2.3 Arc initial conditions

Initial conditions, presented below, obtained from the experimental results, are used to determine the additional parameters for the Mayr approach ( $\tau_M$ ,  $P_M$ ) and for the Cassie approach ( $\tau_C$ ,  $U_C$ ) in Subchapters 7.2.4 and 7.2.5.

- $I_{\text{arc}}(0) = 52.26$  A (initial arc current value)
- $V_c(0) = 10$  kV (initial capacitor voltage value)
- $I_{\text{arc}}(0)/V_{\text{probe}}(0) = 5.23 \times 10^{-3}$  S (initial ratio value)

## 7.2.4 Simulations results – The Mayr approach

With the initial conditions presented in Subchapter 7.2.3, the system of equations composed of equations (7.3) and (7.5) was solved to re-produce experimental results presented in Figure 7.2 and Figure 7.3. The Mayr model with the additional parameters  $\tau_M$  and  $P_M$ , chosen after a trial and error process was used, to better match experimental results, are presented. Comparison between results obtained using chosen parameter values and values found in the literature is presented in Subchapter 7.2.4.1. Furthermore, sensitivity studies for  $\tau_M$  and  $P_M$  parameter variation are discussed in Subchapter 7.2.4.2.

### 7.2.4.1 Mayr parameters determination – $\tau_M$ and $P_M$

Parameters  $\tau_M$ ,  $P_M$  and initial value for ratio,  $I_{\text{arc}}(0)/V_{\text{probe}}(0)$ , available in the literature [SS02], valid for a circuit which represents a short-line fault interruption by a circuit breaker are presented in the first line of Table 7.1. The same  $\tau_M$  and  $P_M$  values are presented in the second line of Table 7.1 along with experimentally determined  $I_{\text{arc}}(0)/V_{\text{probe}}(0)$  value for the present topology (also presented in Subchapter 7.2.3). Moreover, the third line of Table 7.1 contains experimentally determined  $I_{\text{arc}}/V_{\text{probe}}$  and the  $\tau_M$  and  $P_M$  values chosen after a trial and error process to better match obtained experimental results.

In Figure 7.4, the ratio waveforms resulting from the three sets of input presented in Table 7.1 are compared to experimental waveforms. Since a logarithmic scale has been used, only the positive values of the  $I_{\text{arc}}(0)/V_{\text{probe}}(0)$  (see Figure 7.3) are presented. As discussed in Subchapter 7.1.3, since the model parameters are sensitive to circuit topology, the model results corresponding to literature parameters do not match the experimental ones. Model results based on the values of the third line of Table 7.1 match the experimental results reasonably well since they are chosen for this particular topology.

Similar comparison is given in Figure 7.5 for the arc current waveforms. All model input combinations result in identical current waveforms that have the same period and small difference in amplitude with the experimentally obtained curve. Therefore, for the present topology, the arc current model results are insensitive to the choice of  $\tau_M$ ,  $P_M$  and  $I_{\text{arc}}(0)/V_{\text{probe}}(0)$ . They do depend on the current initial condition and the passive, inductive and resistive, elements of the circuit.

Furthermore, the experimental and model voltage waveforms are compared in Figure 7.6. Only the waveform for the chosen model parameters gives a voltage of the same order of magnitude as the experimental one. However, due to the mathematical formulation of Mayr's black-box model, results for the chosen model parameters yield amplification rather than the damping observed in the experiment.

**Table 7.1** Parameters used in the simulations using Mayr's model.

Source	$\tau_M$	$P_M$	$I_{\text{arc}}(0)/V_{\text{probe}}(0)$
Literature parameters	$0.3 \times 10^{-6}$	$3.09 \times 10^4$	$1 \times 10^4$
Literature parameters & experimental $I_{\text{arc}}(0)/V_{\text{probe}}(0)$	$0.3 \times 10^{-6}$	$3.09 \times 10^4$	$5.23 \times 10^{-3}$
Chosen $\tau_M$ , $P_M$ & experimental $I_{\text{arc}}(0)/V_{\text{probe}}(0)$	$5 \times 10^{-8}$	$2 \times 10^6$	$5.23 \times 10^{-3}$

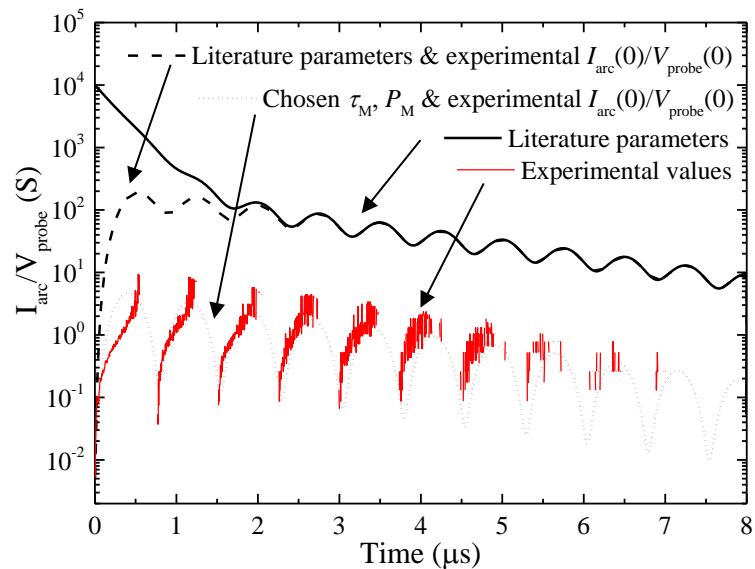


**Figure 7.4** Ratio of experimental arc current over voltage of the probe waveforms comparison using different initial conditions for the  $\tau_M$ ,  $P_M$  and  $I_{\text{arc}}(0)/V_{\text{probe}}(0)$

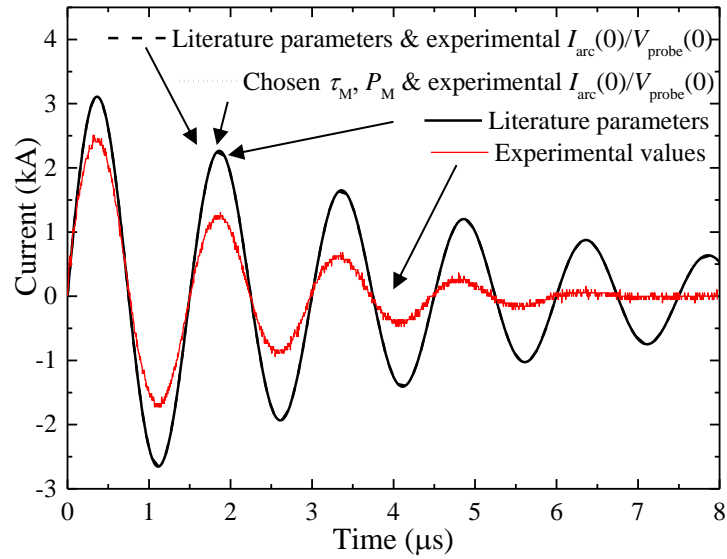


**Figure 7.5** Current waveforms comparison using different initial conditions for the  $\tau_M$ ,  $P_M$  and  $I_{\text{arc}}(0)/V_{\text{probe}}(0)$  (all simulated waveforms coincide)

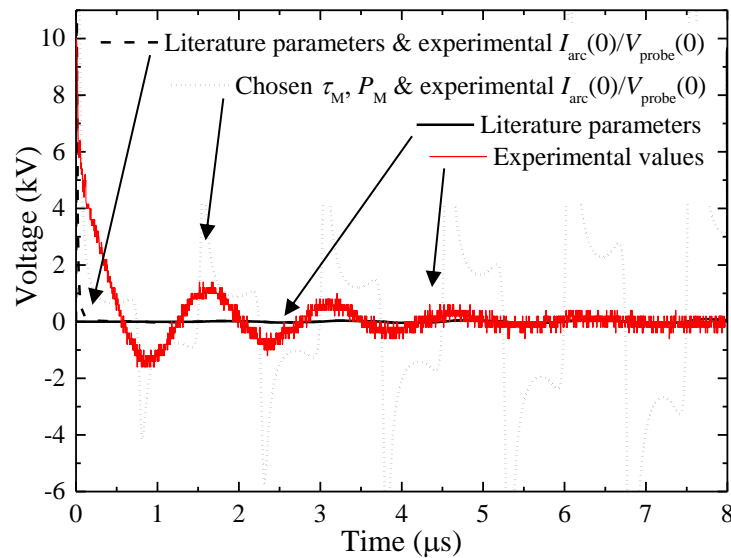


**Figure 7.6** Voltage waveforms comparison using different initial conditions for the  $\tau_M$ ,  $P_M$  and  $I_{\text{arc}}(0)/V_{\text{probe}}(0)$

#### 7.2.4.2 Sensitivity of the model: variation of the Mayr parameters ( $\tau_M, P_M$ )

A comparison of ratio of experimental arc current over voltage of the probe waveforms for varying  $\tau_M = 5 \times 10^{-6}$ ,  $5 \times 10^{-7}$ ,  $5 \times 10^{-8}$ ,  $5 \times 10^{-9}$  and  $5 \times 10^{-10}$  and constant  $P_M = 2 \times 10^6$  is



presented in Figure 7.7. As  $\tau_M$  increases, the shape of the waveform changes and its maximum  $I_{\text{arc}}/V_{\text{probe}}$  value occurs at lower time values. For  $\tau_M \leq 5 \times 10^{-8}$ , the waveforms present insignificant changes.

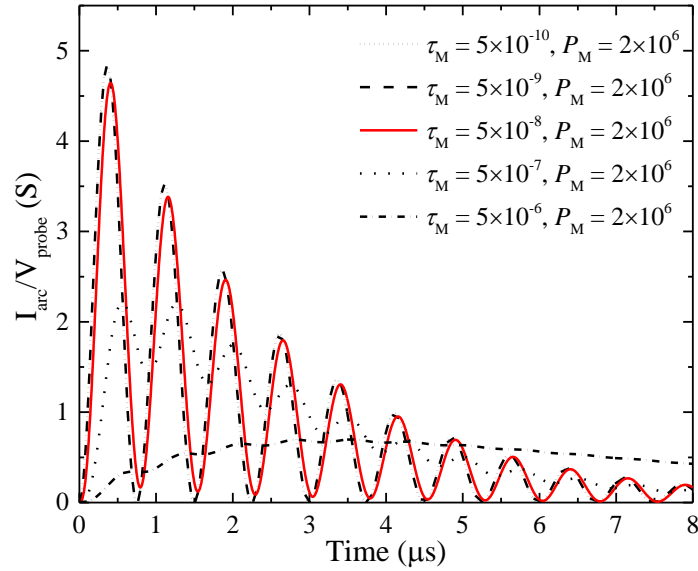


**Figure 7.7** Ratio of experimental arc current over voltage of the probe waveforms for varying  $\tau_M$  (waveforms for  $\tau_M = 5 \times 10^{-9}$  and  $5 \times 10^{-10}$  coincide).

Moreover, the ratio of experimental arc current over voltage of the probe waveforms for varying  $P_M = 2 \times 10^4, 2 \times 10^5, 2 \times 10^6, 2 \times 10^7$  and  $2 \times 10^8$  and constant  $\tau_M = 5 \times 10^{-8}$  are compared in Figure 7.8, where  $I_{\text{arc}}/V_{\text{probe}}$  is presented in log scale on the vertical axis. As  $\tau_M$  changes by an order of magnitude, for the same time value, the ratio falls by an order of magnitude as well. Moreover, the shape of  $I_{\text{arc}}/V_{\text{probe}}$  waveforms is preserved in the log scale for varying  $P_M$ .

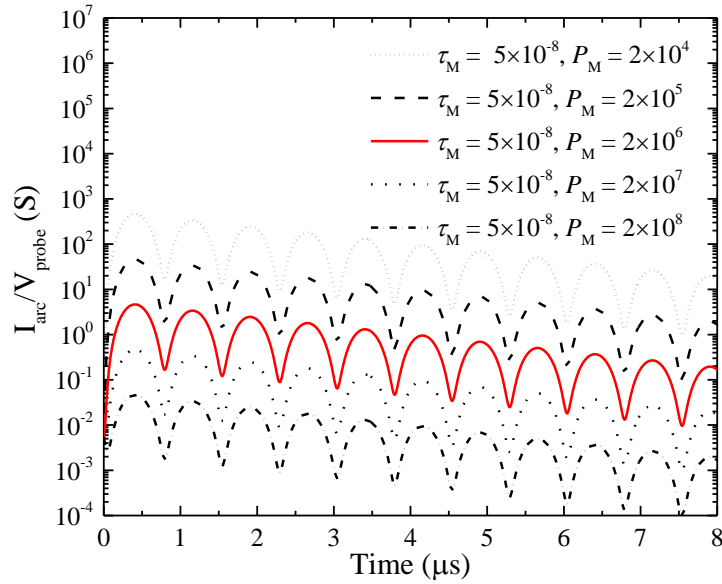


**Figure 7.8** Ratio of experimental arc current over voltage of the probe waveforms for varying  $P_M$ .

## 7.2.5 Simulations results – The Cassie approach

Similarly to Subchapter 7.2.4, experimental waveforms presented in Figure 7.2 and Figure 7.3 were compared with the analytical results obtained using Cassie's model. System of equations (7.4) and (7.5) is solved and model parameters  $\tau_C$  and  $U_C$  are chosen after a trial and error process to better match experimental results. Subchapter 7.2.5.1 shows a comparison of Cassie's model results for chosen parameter values and values presented in the literature. Furthermore, sensitivity studies for  $\tau_C$  and  $U_C$  parameters variations are discussed in Subchapter 7.2.5.2.

### 7.2.5.1 Cassie parameters determination – $\tau_C$ and $U_C$

Parameters  $\tau_C$ ,  $U_C$  and initial value for ratio  $I_{\text{arc}}(0)/V_{\text{probe}}(0)$ , available in the literature [Matlab], valid for a circuit which represents a short-line fault interruption by a circuit breaker are presented in the first line of Table 7.2. The same  $\tau_C$  and  $U_C$  values are presented in the second line of Table 7.2 along with experimentally determined  $I_{\text{arc}}(0)/V_{\text{probe}}(0)$  value for the present topology (also presented in Subchapter 7.2.3). Moreover, the third line of Table 7.2 contains experimentally determined  $I_{\text{arc}}(0)/V_{\text{probe}}(0)$  and the  $\tau_C$  and  $U_C$  values chosen after a trial and error process to better match obtained experimental results.

In Figure 7.9, ratio of experimental arc current over voltage of the probe waveforms resulting from the three sets of input presented in Table 7.2 are compared with experimental

waveforms. Since logarithmic scale has been used, only the positive values of the  $I_{\text{arc}}/V_{\text{probe}}$  (see Figure 7.3) are presented. As discussed in Subchapter 7.1.3, since the model parameters are sensitive to circuit topology, the model results corresponding to literature parameters do not match the experimental ones. Model results based on the values of the third line of Table 7.2 match the experimental results reasonably well since they are chosen for this particular topology.

A similar comparison is presented in Figure 7.10 for the arc current waveforms. All model input combinations result in identical current waveforms that have the same period and small difference in amplitude with the experimentally obtained curve. Therefore, for the present topology, arc current model results are insensitive to the choice of  $\tau_C$ ,  $U_C$  and  $I_{\text{arc}}(0)/V_{\text{probe}}(0)$ . It does depend on the current initial condition and the passive, inductive and resistive, elements of the circuit.

Furthermore, the experimental and model voltage waveforms are compared in Figure 7.11. Waveforms with  $I_{\text{arc}}(0)/V_{\text{probe}}(0)$  equal to the experimental results present voltage of the same order of magnitude as the experimental one. Better fitting is observed for the chosen parameters. Due to the mathematical formulation of Cassie's model, the voltage waveform presents a very slight damping compared with the measured waveform.

**Table 7.2** Parameters used in the simulations using Cassie's model.

Source	$\tau_C$	$U_C$	$I_{\text{arc}}(0)/V_{\text{probe}}(0)$
Literature parameters	$1.2 \times 10^{-6}$	3850	$1 \times 10^4$
Literature parameters & experimental $I_{\text{arc}}(0)/V_{\text{probe}}(0)$	$1.2 \times 10^{-6}$	3850	$5.23 \times 10^{-3}$
Chosen $\tau_C$ , $U_C$ & experimental $I_{\text{arc}}(0)/V_{\text{probe}}(0)$	$1 \times 10^{-8}$	700	$5.23 \times 10^{-3}$

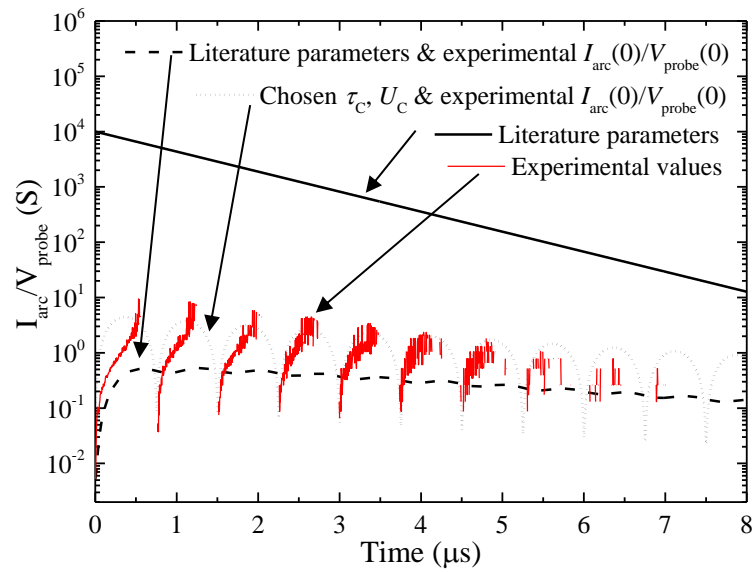


**Figure 7.9** Ratio of experimental arc current over voltage of the probe waveforms comparison using different initial conditions for the  $\tau_c$ ,  $U_c$  and  $I_{\text{arc}}(0)/V_{\text{probe}}(0)$ .

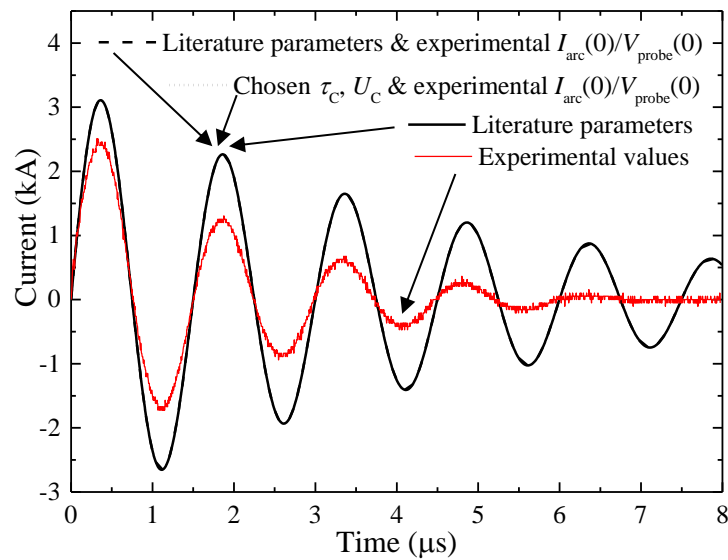


**Figure 7.10** Current waveforms comparison using different initial conditions for the  $\tau_c$ ,  $U_c$  and  $I_{\text{arc}}(0)/V_{\text{probe}}(0)$  (all simulated waveforms coincide)

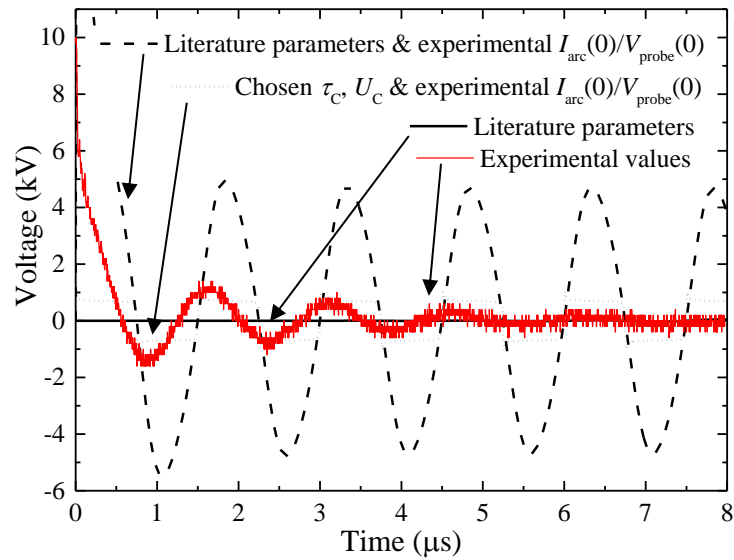
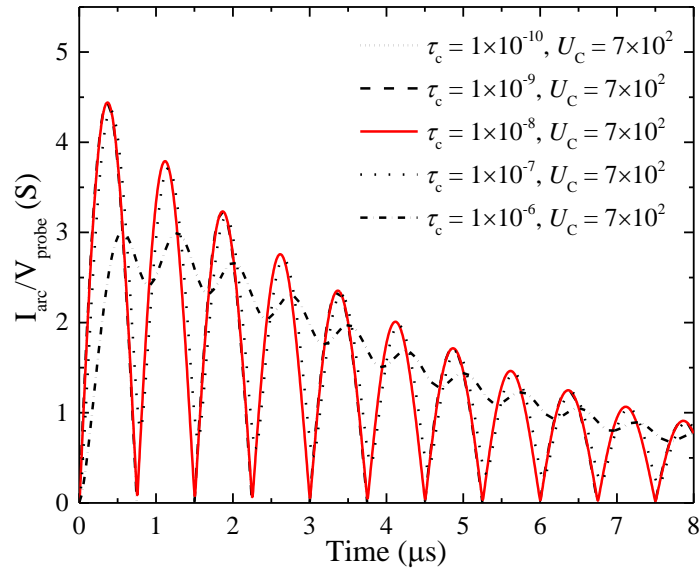


**Figure 7.11** Voltage waveforms comparison using different initial conditions for the  $\tau_c$ ,  $U_c$  and  $I_{\text{arc}}(0)/V_{\text{probe}}(0)$

### 7.2.5.2 Sensitivity of the model: variation of the Cassie parameters ( $\tau_c$ , $U_c$ )

Comparison of ratio of experimental arc current over voltage of the probe waveforms for varying  $\tau_c = 1 \times 10^{-10}$ ,  $1 \times 10^{-9}$ ,  $1 \times 10^{-8}$ ,  $1 \times 10^{-7}$  and  $1 \times 10^{-6}$  and constant  $U_c = 3850$  is presented in Figure 7.12. As  $\tau_c$  increases, the shape of the waveform changes and its maximum  $I_{\text{arc}}/V_{\text{probe}}$  value occurs at lower time values. For  $\tau_c \leq 1 \times 10^{-8}$ , the waveforms present insignificant changes.



- **Figure 7.12** Ratio of experimental arc current over voltage of the probe waveforms for varying  $\tau_c$  (waveforms for  $\tau_c = 1 \times 10^{-10}$ ,  $1 \times 10^{-9}$  and  $1 \times 10^{-8}$  coincide).

Moreover, ratio of experimental arc current over voltage of the probe waveforms for varying  $U_C = 7, 7 \times 10^1, 7 \times 10^2, 7 \times 10^3$  and  $7 \times 10^4$  and constant  $\tau_c = 1 \times 10^{-8}$  are compared in Figure 7.13 where  $I_{\text{arc}}/V_{\text{probe}}$  is presented in log scale on the vertical axis. As  $U_C$  changes by an order of magnitude, for the same time value, the ratio falls by an order of magnitude as well. Moreover, the shape of  $I_{\text{arc}}/V_{\text{probe}}$  waveforms is preserved in the log scale for varying  $U_C$ .

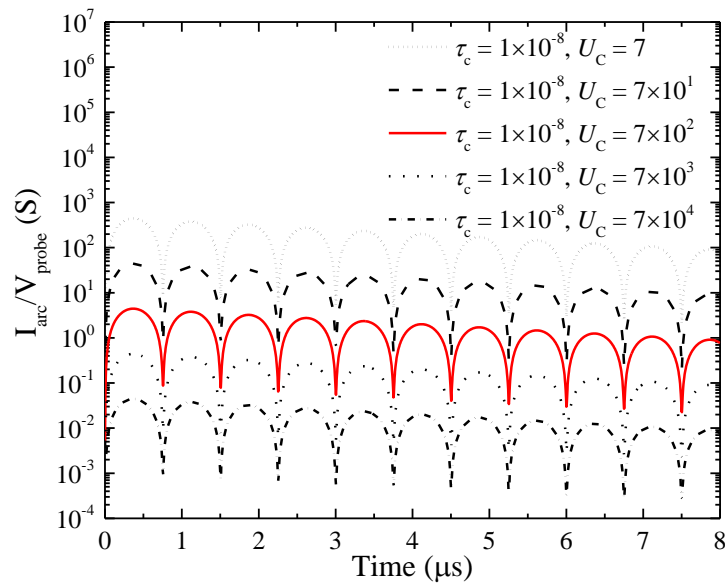


**Figure 7.13** Ratio of experimental arc current over voltage of the probe waveforms for varying  $U_C$ .

### 7.3 Conclusions

Investigation of the suitability of the black-box model analysis for predicting the arc-circuit interaction within a capacitive circuit and for arc initiation (order of  $\mu\text{s}$ ) was presented.

It was found that, with the chosen model parameters, both the Cassie and Mayr models are suitable for prediction of the behaviour of the initial stage of arc formed within an electric circuit. Both models re-produce the arc current and voltage of the probe waveforms. The damping nature of the voltage waveform is not adequately re-produced, and this is attributed to modelling limitations. Voltage waveform obtained with the Cassie model presents almost non-damping waveform, while usage of the Mayr model showed an amplifying voltage waveform.

Black-box models have already been successfully applied for capturing arc behaviour within power systems at the fully developed stage of the arc. Therefore, outcome of this investigation on the ratio of the arc current over voltage shows that the same models can be used for description of the processes at the arc initiation. Hence, a consistent implementation of the same type of model could offer a link between arc initiation and its evolution.

Future work is required to establish the complete accurate link between arc initiation and evolution. The network configuration influences to a certain degree the initiation, development and the evolution of the arc. It is important to investigate this connection from

an energy point of view. Since energy partition analysis during arc initiation has been performed in Chapter 6, establishing this connection could contribute towards the prediction of energy partition during the arc's full development.



# Chapter 8

---

## Conclusions and future work

Chapter 8 summarises the main conclusions drawn from the current work and discusses possible extensions of the research.

### 8.1 Conclusions

The aim of the present research was to advance our knowledge and understanding of electrical arc flash and arc blast hazards through experimentation, modelling and analysis. To achieve this, the research conducted has been consisted of two main parts. In the first part, significant work has been carried out to analyse data on arc flash hazards and mitigation engineering practises in industrial premises. In the second part, the focus of the research has been directed in the arc onset to understand better the energy conversion processes taking place and quantify the associated energy components.

#### 8.1.1 Arc flash studies review

In the beginning of the research project, data derived from arc flash hazard calculation studies and arc flash hazard risk mitigation studies conducted by GSE Systems (former TAS Consultancy) have been analysed.

The following main conclusions have been derived from the analysis of the well-established and approved industrial engineering approach:

- Both HV buses and LV buses can exhibit high levels of arc incident energy levels.
- All incident energy levels can occur in any facility type.
- All types of facility can exhibit dangerous incident energy levels.

- Risk control measures can lead to significant reductions in potential harm and damage should an arc flash occur.
- The discussed mitigation methods alone do not prevent arc initiation.
- Every installation is different and requires its own unique solution to ensure that risk is reduced as much as possible.
- In some cases, the hazard can be reduced without significant investment in equipment.
- The use of PPE is suggested as the last line of protection.

The following item is drawn to the reader's attention:

- Quantification tools for the hazards related to different energy components in the arc are still under development, and further research and validation is required. Only the thermal hazard levels associated with an arc flash and arc blast incident can be addressed in accordance with current standards. A major collaborative research project between the Institute of Electrical and Electronics Engineers (IEEE) and the National Fire Protection Association (NFPA) started in 2004 to experimentally investigate the heat and thermal energy, blast pressure, sound, and light during an arcing fault, to update the current standards concerning arc flash safety.

These findings, and primarily that the mitigation methods alone do not prevent arc initiation, provided direction on the research progress towards an investigation into the initiation of electrical arcs. Thus, research into novel approaches to understand the hazards posed during the arcing fault onset has been conducted.

### **8.1.2 Arc onset**

For the scope of the present study two similar experimental topologies have been designed and built and two sets of high voltage tests have been conducted. During the first set of tests, spark discharges were generated in a self-breakdown air spark gap (SBSG). Then, the SBSG topology was slightly amended to be used for the second set of tests where discharges were initiated with a thin conducting wire (wire-guided spark gap (WGSG)). Finally, a series of preliminary tests and simulations have been performed to validate the suitability of the set-up for subsequent testing.

The developed experimental set-up includes two major novel elements:

- The busbar to point electrode gap topology. The inclusion of a busbar in the experimental topology allows the representation of a topology like an industrial one, where the busbar location is one of the most likely locations for a severe arc flash incident to occur.
- The voltage-dividing current shunt custom-built to be utilised for the current sensing in the SBSG topology. There was a necessity for developing measuring equipment to fit within the small dimensions of the SBSG topology which simultaneously should withstand the high levels of voltage.

The acquired waveforms during arc onset have been analysed with the aid of MATLAB/Simulink software. Data post-processing techniques have been developed and implemented to extract arc voltage and current waveforms for calculating the electrical arc energy available in the discharge.

The energy calculations primarily performed by following the technique developed by William Greason [Gre97], [Gre99] considering the resistance of the spark as a constant. Analysis of the dynamic resistance poses many challenges which are related to the very fast evolving processes taking place within very short time scales. These processes are also difficult to be monitored due to equipment limitations.

The comparison between the energy calculation based on the dynamic and the equivalent constant arc resistance showed that the equivalent constant resistance seems to fit well enough the transient resistance when it reaches its minimum. Moreover, it has been observed that the calculated transient and constant energy values for the WSGS are of the same order of magnitude. Thus, the equivalent constant arc resistance represents adequately the relationship between the voltage and the current of the arc discharge during its initiation.

Using the hydrodynamic model developed in Chapter 6, the calculated electrical energy deposited into the arc plasma channel has been analysed in three energy components.

### **8.1.3 Hydrodynamic model analysis**

In Chapter 6 a novel analytical model has been developed on the basis of the hydrodynamic theory. This novel model allows the energy components associated with thermal, acoustic-kinetic and light emissions during arc initiation to be obtained providing useful information for safety considerations.

The energy components have been obtained for the case of the SBSG and the WGSG. These two ways of arc initiation was found to exhibit similar behaviour characteristics. In both cases the bulk energy was converted in internal energy and mechanical work due to the expansion of the arc plasma channel. The portion of the light emission is significantly smaller than the other two components, it is almost negligible.

Specifically, for a typical SBSG discharge it was obtained that:

- ~71.2 % of the electric energy transforms into work
- ~28.5 % of the electric energy transforms into internal energy
- ~0.3 % of the electric energy transforms into light emission

For a typical WGSG discharge it was found that:

- ~65.5 % of the electric energy transforms into work
- ~33.5 % of the electric energy transforms into internal energy
- ~1 % of the electric energy transforms into light emission

Similar energy partition percentages are observed for all the individual discharges created in the SBSG and the WGSG topologies.

As discussed previously, the energy partition follows similar trends for the two ways of the arc initiation. It was observed that, at the very beginning of the discharge, the main portion of the electrical energy is converted into the internal energy of the gas. However, the mechanical work component quickly becomes significant. During the evolution of the discharge, the electrical energy partitions mainly into the mechanical work and internal energy. Losses due to light emission are significantly smaller than the aforementioned energies. This behaviour was exhibited for both ways of arc initiation.

The important role in the energy partition process plays the duration of the energy deposition phase. Thus, the longer the energy deposition phase the longer the internal energy and the mechanical work have their maximums.

Finally, verification of the present model was performed through comparison with the model developed by Braginskii based on the shock-wave theory. The results obtained for the two ways of the arc initiation were very similar, thus the model developed for the thesis can readily describe the development of the phenomenon. The assumption made that the disturbance is not a shock-wave does not influence much the expected results.

### 8.1.4 Black-box model analysis

The main contribution of Chapter 7 was in the analysis and evaluation of the suitability of black-box models for predicting the arc-circuit interaction:

- Within a capacitive circuit; research to date has been focused on AC power system topologies.
- At the arc initiation stage with duration of a few  $\mu\text{s}$ ; (to date black-box models have been used for investigation of the arc behaviour within a time range of ms and longer).

It was found that with chosen model parameters both the Cassie and Mayr models are suitable for prediction of the behaviour of the initial stage of arc formed within an electric circuit. Both models re-produce the arc current and voltage of the probe waveforms. The damping nature of the voltage waveform is not adequately re-produced, and this is attributed to modelling limitations. Voltage waveform obtained with the Cassie model presents almost non-damping waveform, while, usage of the Mayr model showed an amplifying voltage waveform.

Black-box models have already been successfully applied for capturing arc behaviour within power systems at the fully developed stage of the arc. Therefore, outcome of this investigation on the ratio of the arc current over voltage shows that the same models can be used for description of the processes at the arc initiation. Hence, a consistent implementation of the same type of model could offer a link between arc initiation and its evolution.

This is an initial step towards establishment of the complete accurate link between arc initiation and its evolution. Since the energy partition analysis during arc initiation has been performed (see Chapter 6), when the link between arc initiation and evolution will be established, it could facilitate prediction of the energy partition during arc's full development.

## 8.2 Future work

The focus of the present research was on the development of a novel analytical model on the basis of hydrodynamic theory. Thus, the energy components associated with thermal,

acoustic-kinetic and light emissions during arc initiation can be obtained providing useful information for safety considerations. During the research, emphasis was also given on the analysis and evaluation of the suitability of black-box models for predicting the arc-circuit interaction during arc onset. Outcome of this investigation shows that the same models with the ones used in the power systems industry can be used for description of the processes at the arc initiation.

Possible extensions of the current work could go beyond the confines of the present research which are:

- The experimental data include low energy levels with short time durations which are limited by laboratory capabilities. Higher energy levels with larger time duration could potentially be examined to analyse the transient behaviour of the arc. The role of additional variables, i.e. thermal conduction, can be examined to understand their effects on the results.
- Future experimental work can be conducted for other type of electrical circuit apart from the capacitive energy storage circuit. For arc initiation the behaviour of the electrical circuit does not affect much the characteristics of the arc. However, during its full development the arc characteristics do have a dependency on the electrical circuit.
- Additional research on establishing the complete accurate link between arc initiation and evolution can be conducted. Hydrodynamic model analysis can be used on the potential data derived from future research to predict the energy partition beyond the arc initiation phase. Ultimately goal is to define the energy partition during arc's full development.
- It is expected that IEEE/NPFA data on energy components of an arc flash and arc blast obtained experimentally will be publicly available. The present analytical work along with the extended suggested investigations can be further validated against the organisations results to establish a complete accurate link between empirical and analytical approaches regarding arc flash and arc blast hazards.

# References

---

- [AGS+10] R. F. Ammerman, T. Gammon, P. K. Sen, and J. P. Nelson, "DC-Arc Models and Incident-Energy Calculations," *IEEE Transactions on Industry Applications*, vol. 46, no. 5, pp. 1810-1819, Sept./Oct. 2010.
- [AKK+88] H. Akiyama, M. Kristiansen, H. Krompholz and B. Maas, "Current voltage characteristics of high-current pulsed discharge in air," *IEEE Transactions on Plasma Science*, vol. 16, no. 2, pp. 312-316, 1988.
- [Bel99] S. Bell, *Measurement Good Practice Guide No.11: A Beginner's Guide to Uncertainty of Measurement*, National Physical Laboratory Teddington Middlesex, UK, 1999.
- [BNG+02] A. Bogaerts, E. Neyts, R. Gijbels, and J. Van Der Mullen, "Gas discharge plasmas and their applications," *Spectrochimica Acta Part B: Atomic Spectroscopy*, vol. 57, no. 4, pp. 609-658, 2002.
- [BPV09] S. Buogo, J. Plocek and K. Vokurka, "Efficiency of energy conversion in low-voltage spark discharges and associated bubble oscillations: Experimental results," *Acta Acustica united with Acustica*, vol. 95, no. 1, pp. 46-59, Jan./Feb. 2009.
- [Bra58] S. I. Braginskii, "Theory of the Development of a Spark Channel," *Journal of Experimental and Theoretical Physics*, vol. 34, no. 6, pp. 1068-1074, Dec. 1958.
- [Bro55] T. E. Browne, "The Electric Arc as a Circuit Element," *Journal of The Electrochemical Society*, vol. 102, no.1, pp. 27-37, Jan. 1955.
- [Buc14] M. K. Bucher, *Transient Fault Currents in HVDC VSC Networks During Pole-to-Ground Faults*, Doctoral dissertation, ETH Zurich, 2014.
- [BVL75] S. I. Barannik, S. B. Vasserman and A. N. Lukin, "Resistance and Inductance of a Gas Arc," *Soviet Physics Technical Physics*, vol. 19, pp. 1449-1453, May 1975.
- [Cas39] A. M. Cassie, "Arc rupture and circuit severity: A new theory," *CIGRE Report 102*, pp. 2-14, 1939.
- [CD89/391EEC] Council Directive 89/391 EEC, "On the introduction of measures to encourage improvements in the safety and health of workers at work," *Official Journal of the European Communities*, Luxemburg, June 1989.

- [CF85] R. Courant and K. O. Friedrichs, "Shock Waves versus Sound Waves," *Los Alamos Science*, pp. 42-43, 1985.
- [Cigre93] Working Group 13.01 Cigre, "Applications of black box modelling to circuit breakers," *Electra No. 149*, pp. 40-71, Aug.1993.
- [CJS75] A. Chapman, G. R. Jones and D. Strachan, *Arc Research Report ULAP-T36*, University of Liverpool, 1975.
- [CLS16] R. Catlett, M. Lang and S. Scala, "Novel Approach to Arc Flash Mitigation for Low-Voltage Equipment," *IEEE Transactions on Industry Applications*, vol. 52, no. 6, pp. 5262-5270, 2016.
- [Coo14] V. Cooray, *The lightning flash*, The Institution of Engineering and Technology, 2014.
- [Das12] J. C. Das, *Arc Flash Hazard Analysis and Mitigation*, Piscataway, NJ, USA, IEEE Press, 2012.
- [DMS+68] I. V. Demenik, V. E. Mnuskin, B. V. Skortsov, and V. B. Fedorov, "Resistance of a Xenon Plasma in a Large Flash Lamp," *Soviet Physics Technical Physics*, vol. 13, no. 6, pp. 829-832, 1968.
- [DNA+13] M. D' Mello, M. Noonan, H. Aulakh, and J. Mirabent, "Arc flash energy reduction - Case studies," *IEEE Transactions on Industry Applications*, vol. 49, no. 3, pp. 1198-1204, Mar. 2013.
- [Dra51] S. I. Drabkina, "The Theory of the Development of the Channel of the Spark Discharge," *Journal of Experimental and Theoretical Physics*, vol. 21, no. 4, pp. 473-483, 1951.
- [DSB09] D. R. Doan, J. K. Slivka, and C. J. Bohrer, "A Summary of Arc Flash Hazard Assessments and Safety Improvements," *IEEE Transactions on Industry Applications*, vol. 45, no. 4, pp. 1210-1216, 2009
- [DuPont] DuPont, *The DuPont<sup>(TM)</sup> Arc-Guide: The European Approach to Electric Arc Risk Assessment*, viewed 15 November 2017, [www2.dupont.com/Electrical\\_Arc\\_Protection/en\\_GB/assets/downloads/E\\_Arc\\_Flyer.pdf](http://www2.dupont.com/Electrical_Arc_Protection/en_GB/assets/downloads/E_Arc_Flyer.pdf)
- [EAWR89] *The Electricity at Work Regulations 1989 No. 635*, Statutory Instruments, 1989.
- [Ede61] H. Edels, "Properties and theory of the electric arc. A review of progress," *Proceedings of the IEE - Part A: Power Engineering*, vol. 108, no. 37, pp. 55-69, Feb. 1961.



- [EDK89] T. G. Engel, A. L. Donaldson, and M. Kristiansen, "The Pulsed Discharge Arc Resistance and its Functional Behavior," *IEEE Transactions on Plasma Science*, vol. 17, no. 2, pp. 323-329, Apr. 1989.
- [FJ13] H. L. Floyd and B. C. Johnson, "A global approach to managing risks of arc flash hazards," *Conference Record PCIC Europe*, Istanbul, Turkey, May 2013.
- [Fri08] A. Fridman, *Plasma Chemistry*, Cambridge, Cambridge University Press, 2008
- [GCG17] L. B. Gordon, K. D. Carr and N. Graham, "Complete Electrical Arc Hazard Classification System and Its Application", *IEEE Transactions on Industry Applications*, vol. 53, no. 5, pp. 5078-5087 Sept./Oct. 2017
- [GG15] L. B. Gordon and N. Graham, "A complete electrical arc hazard classification system and its application," *Proceedings of the IEEE IAS Electrical Safety Workshop*, Louisville, KY, USA, Jan. 2015.
- [GHS+15] M. Golovkov, E. Hoagland, H. Schau, and C. Maurice, "Effect of Arc Electrode Geometry and Distance on Cotton Shirt Ignition," *IEEE Transactions on Industry Applications*, vol. 51, no.1, pp. 36-44, 2015.
- [GLZ+15] T. Gammon, W. Lee, Z. Zhang, and B. C. Johnson, "Electrical safety, electrical hazards, and the 2018 NFPA 70E: Time to update annex K?," *IEEE Transactions on Industry Applications*, vol. 51, no. 4, pp. 2709-2716, Jul./Aug. 2015
- [GR71] G. M. Goncharenko and I. N. Romanenko, "Discharge channel in helium at 100 atm and in air," *Soviet Physics Technical Physics*, vol. 15, pp. 1990-1998, 1971.
- [Gre97] W. D. Greason, "Methodology to study the resistance of spark discharges," *Proceedings of the IEEE IAS Annual Meeting*, New Orleans, LA, USA, Oct. 1997.
- [Gre99] W. D. Greason, "Methodology to study the resistance of spark discharges," *IEEE Transactions on Industry Applications*, vol. 35, no. 2, pp. 359-365, Mar./Apr. 1999.
- [Gro04] F. W. Grover, *Inductance calculations: working formulas and tables*, Courier Corporation, 2004.
- [GSES15] Arc flash analysis data received from GSE Systems on 25<sup>th</sup> March 2015.
- [Hab88] U. Habedank, "On the Mathematical Description of Arc Behaviour in the

- Vicinity of Current Zero,” *ETZ Archiv Bd.*, vol. 10, no.11, 1988, pp. 339-343.
- [Ham95] L. Hammond, “Underwater shock wave characteristics of cylindrical charges,” *Aeronautical and Maritime Research Laboratory Ship Structures and Materials Division, Report No. DSTO-GD-0029*, Melbourne, Australia, 1995.
- [HG04] K. S. Hunter and T. L. Geers, “Pressure and velocity fields produced by an underwater explosion,” *The Journal of the Acoustical Society of America*, vol. 115, no. 4, pp. 1483-1496, 2004.
- [HHJ+12] R. M. Harris, X. Hu, M. D. Judd, and P. J. Moore, “Detection and location of arcing faults in distribution networks using a non-contact approach,” *Proceedings of IEEE International Power Modulator and High Voltage Conference*, San Diego, CA, USA, June 2012, pp. 583-586.
- [HMH17] E. H. Hoagland, C. Maurice, A. Haines and A. Maurice, “Arc Flash Pressure Measurement by Physical Method, Effect of Metal Vapor on Arc Blast,” *IEEE Transactions on Industry Applications*, vol. 53, no. 2, pp. 1576-1582, Apr. 2017.
- [HMS16] R. Hasan, R. Mendler and L. Steinbeigle, “Hybrid arc flash protection within electrically classified areas,” *IEEE Transactions on Industry Applications*, vol. 52, no. 4, pp. 3548-3556, 2016.
- [HSD+10] B. Hughes, V. Skendzic, D. Das and J. Carver, “High-current qualification testing of an arc-flash detection system,” *Proceedings of the 9th Annual Clemson University Power Systems Conference*, March 2010.
- [HSE15] Guidance on Regulations: The Electricity at Work Regulations 1989, *Health and Safety Executive*, Crown, 2015.
- [Hug16] B. Hughes, “Arc-flash detection prevents catastrophic damage,” *IEEE IAS Electrical Safety Workshop*, Jacksonville, FL, USA, March 2016, pp. 1-5.
- [IEEE1584] *IEEE Guide for Performing Arc Flash Hazard Calculations*, IEEE Standard 1584, 2002.
- [ISO31000] *ISO31000 Risk Management-Principles and Guidelines*, 2009
- [IUPAC14] International Union of Pure and Applied Chemistry, *Electrical arcs*,

<http://iupac.org/publications/analyticalcompendium/Cha10sec312.pdf>  
(accessed: 13 October 2014)

- [Jon88] G. R. Jones, *High pressure arcs in industrial devices: diagnostic and monitoring techniques*, Cambridge, Cambridge University Press, 1988.
- [KF01] D. Kind and K. Feser, *High Voltage Test Techniques*, Oxford, Newnes, 2001.
- [KGV11] J. Kudelčik, M. Gutten and P. Virdzek, "Measurement of electrical parameters of breakdown in transformer oil," *Przegląd Elektrotechniczny (Electrical Review)*, vol. 87, no. 6, pp. 159-162, 2011.
- [Kim09] C. J. Kim, "Electromagnetic Radiation Behavior of Low-Voltage Arcing Fault," *IEEE Transactions on Power Delivery*, vol. 24, no. 1, pp. 416-423, Jan. 2009.
- [KKB85] M. J. Kushner, W. D. Kimura, and S. R. Byron, "Arc resistance of laser triggered spark gaps," *Journal of Applied Physics*, vol. 58, no. 5, pp. 1744-1751, 1985.
- [Küc17] A. Küchler, *High Voltage Engineering: Fundamentals-Technology-Applications*. Germany, Springer, 2017.
- [KZ94] E. Kuffel, and W. S. Zaengl, *High Voltage Engineering Fundamentals*, Pergamon Press, Oxford, 1994.
- [Lan08] H. B. Land, "The behavior of arcing faults in low voltage switchboards," *IEEE Transactions on Industry Applications*, vol. 44, no. 2, pp. 437-444, Mar./April 2008.
- [LBR17] V. B. Litovski, S. P. Le Blond, B. P. Ross, "Transient circuit implementation of arc models with particular focus on arcs in low-voltage power cables," *Electric Power Systems Research*, vol. 147, pp. 105-114, June 2017.
- [Lee82] R. H. Lee, "The Other Electrical Hazard: Electric Arc Blast Burns," *IEEE Transactions on Industry Applications*, vol. IA-18, no.3, pp. 246-251, May 1982
- [Lee87] R. H. Lee, "Pressures Developed by Arcs," *IEEE Transactions on Industry Applications*, vol. IA-23, no. 4, pp. 760-763, July 1987.
- [LGZ+12] W.-J. Lee, T. Gammon, Z. Zhang, B. Johnson, and S. Vogel, "IEEE/NFPA collaboration on arc flash phenomena research project," *IEEE Power Energy Magazine*, vol. 10, no. 2, pp. 116-123,

Mar./Apr. 2012.

- [LM40] L. B. Loeb and J. M. Meek. *The Mechanism of Electric Spark*, Stanford University Press, 1940.
- [LRB+11] F. Leonard, L. Reynaud, J. Bherer, and D. Pineau, "Partial Discharge (PD) Sniffer for Workers' Safety in Underground Vaults," *presented at the CIGRE 21<sup>st</sup> International Conference on Electricity Distribution*, Frankfurt, 2011.
- [Maa85] B. L. Maas, "Arc current, voltage, and resistance in high energy, gas-filled spark gap," Doctoral dissertation, Texas Tech University, May 1985.
- [Mar60] E. A. Martin, "Experimental Investigation of a High-Energy Density, High-Pressure Arc Plasma," *Journal of Applied Physics*, vol. 31, no. 2, pp. 255-267, 1960.
- [Matlab] MATLAB, Cassie and Mayr Arc Models for a Circuit Breaker
- [May43] O. Mayr, "Beitrage zur Theorie des Statischen und des Dynamischen Lichtbogens," *Archiv fur Electrotechnik*, vol. 37, no. 12, pp. 588-608, 1943.
- [McG17] C. McGarvey, "Characterisation of plasma closing switches filled with different gases", Doctoral dissertation, University of Strathclyde, 2017
- [Mee40] J. M. Meek, "A Theory of Spark Discharge," *Physical Review*, vol. 57, no.8, pp. 722-728, Apr. 1940.
- [Men15] W. P. Mendenhall, "DC arc hazard mitigation design at a nuclear research facility," *IEEE Transactions on Industry Applications*, vol. 51, no. 1, pp. 69-72, 2015.
- [MPS13] N. S. Mahajan, K. R. Patil, S. M. Shembekar, "Electric arc model for high voltage circuit breakers based on Matlab/Simulink," *Pratibha: International Journal of Science, Spirituality, Business and Technology*, vol. 1, no.2, pp. 15-21, Feb. 2013.
- [Nei06] D. K. Neitzel, "The Hazards of Electricity- Do You Know What They Are?," *presented at the IEEE IAS Electrical Safety Workshop*, Philadelphia, PA, Feb. 2006.
- [Nei08] D. K. Neitzel, "Understanding NFPA 70E electrical safety requirements," *Proceedings of IEEE/IAS Industrial and Commercial Power Systems Technical Conference*, Clearwater Beach, FL, USA, May

2008.

- [NFPA70E] *NFPA 70E: Standard for Electrical Safety in the Workplace*, NFPA Standard 70E, 2012.
- [NR71] K. A. Naugol'nykh and N. A. Roi, *Spark Discharges in Water (A Hydrodynamical Description)*, translation, Foreign Technology Division, Wright-Patterson AFB, OH, 1974), Nauka, Moscow, 1971.
- [OIT+10] T. Ohtaka, M. Iwata, S. Tanaka and Y. Goda, "Development of an EMTP Simulation Model of Arcing Horns Interrupting Fault Current," *IEEE Transactions on Power Delivery*, vol. 25, no. 3, July 2010.
- [PF12] P. E. J. Phillips and M. Frain, "A European view of arc flash hazards and electrical safety," *Proceedings of the IEEE IAS Electrical Safety Workshop*, Daytona Beach, FL, USA, Feb. 2012.
- [Phi11] J. Phillips. *Complete Guide to Arc Flash Hazard Calculation Studies*. Brainfiller, Incorporated, 2011.
- [Pie10] A. Piel, *Plasma Physics: An Introduction to Laboratory, Space, and Fusion Plasmas*, Springer-Verlag Berlin Heidelberg, 2010.
- [PPP74] M. M. Popovic, S. S. Popovic and M. M. Platisa, "Investigation of the beginning of high current discharges in pulsed arcs," *Proceedings of International Conference on Gaseous Discharges*, p.32-36, 1974.
- [PS16] K. D. Parrott and D. R. Stahl, "*Electrical arcs and sparks: A literature review of definitions and their implications in the analysis of 12-volt direct current electrical system fires (white paper)*," viewed 25 September 2016, [www.stahl-engineering.com](http://www.stahl-engineering.com).
- [PS17] J. Prigmore and J. S. Schaffer, "Triggered Current Limiters - Their Arc Flash Mitigation and Damage Limitation Capabilities," *IEEE Transactions on Power Delivery*, vol. 32, no.2, pp. 1114-1122, Apr. 2017.
- [PVG+92] P. Persephonis, K. Vlachos, C. Georgiades, and J. Parthenios, "The Inductance of the Discharge in a Spark Gap," *Journal of Applied Physics*, vol. 71, no. 10, pp. 4755-4762, 1992.
- [PVL13] H. Picard, J. Verstraten, and R. Luchtenberg, "Practical approaches to mitigating Arc Flash exposure in Europe," *Conference Record of PCIC Europe, Istanbul, Turkey*, May 2013.
- [RCR+96] R. M. Roberts, J. A. Cook, R. L. Rogers, A. M. Gleeson, and

- T. A. Griffy, "The energy partition of underwater sparks," *The Journal of the Acoustical Society of America*, vol. 99, no. 6, pp. 3465-3475, 1996.
- [Rob12] D. Roberts, "Risk management of electrical hazards," *Proceedings of IEEE IAS Electrical Safety Workshop*, Daytona Beach, FL, USA, Feb. 2012.
- [RPV11] G. Roscoe, T. Papallo, and M. Valdes, "Fast energy capture," *IEEE Industry Applications Magazine*, vol. 17, no. 4, pp. 43-52, 2011.
- [RW44] R. Rompe and W. Weizel, "Über das Toeplersche Funkengesetz," *Z. Phys*, vol. 122, pp. 636-639, 1944.
- [SJB+98] A. Schutze, J. Y. Jeong, S. E. Babayan, J. Park, G. S. Selwyn and R. F. Hicks, "The atmospheric-pressure plasma jet: a review and comparison to other plasma sources" *IEEE Transactions on Plasma Science*, vol. 26, no. 6, pp. 1685-1694, Dec. 1998.
- [SK00] R. P. P. Smeets and V. Kertesz, "Evaluation of high-voltage circuit breaker performance with a validated arc model," *IEE Proceedings-Generation, Transmission and Distribution*, vol. 147, no. 2, pp. 121-125, Mar. 2000.
- [SS00] P. H. Schavemaker and L. Van Der Slui, "An improved Mayr-type arc model based on current-zero measurements," *IEEE Transactions on Power Delivery*, vol. 15, no. 2, pp. 580-584, Apr. 2000.
- [SS02] P. H. Schavemaker and L. Van Der Sluis "The arc model blockset," *Proceedings of the 2<sup>nd</sup> IASTED International Conference Power and Energy Systems*, Crete, Greece, 2002.
- [SS06] A. D. Stokes and D. K. Sweeting, "Electric arcing burn hazards," *IEEE Transactions on Industry Applications*, vol. 42, no.1, pp. 134-141, Jan./Feb. 2006.
- [SS07] D. K. Sweeting and A. D. Stokes, "Energy transfers within arcing faults in electrical equipment," *Proceedings of the 8<sup>th</sup> International Conference on Electric Fuses and their Applications*, Clermont-Ferrand, France, Sep. 2007, pp. 169-178.
- [SW11] D. D. Shipp and D. M. Wood, "Mitigating Arc-Flash Exposure," *IEEE Industry Applications Magazine*, vol. 17, no. 4, pp. 28-37, July/Aug. 2011.
- [TBI+07] S. I. Tkachenko, D. V. Barishpoltsev, G. V. Ivanenkov,

- V. M. Romanova, A. E. Ter-Oganesyan, A. R. Mingaleev, T. A. Shelkovenko, and S. A. Pikuz, "Different mechanisms of shock wave generation and scenarios of second breakdown development upon electrical explosion of wires," *Proceedings of 16th IEEE International Pulsed Power Conference*, Albuquerque, NM, USA, June 2007, vol. 1, pp. 877-880.
- [TFG+06] I. V. Timoshkin, R. A. Fouracre, M. J. Given, and S. J. MacGregor, "Hydrodynamic modelling of transient cavities in fluids generated by high voltage spark discharges," *Journal of Physics D: Applied Physics*, vol. 39, no. 22, p. 4808-4817, 2006.
- [Tho70] R. J. Thomas, "High-Impulse Current and Voltage Measurement," *IEEE Transactions on Instrumentation and Measurement*, vol. 19, no. 2, pp. 102-117, May 1970.
- [TMG+08] I. V. Timoshkin, S. J. MacGregor, M. J. Given, and M. P. Wilson, "Plasma-acoustic sources and their practical applications," *Proceedings of the 17th International Conference on Gas Discharges and Their Applications*, Cardiff, UK, Sept. 2008, pp. 381-384.
- [Toe06] M. Toepler, "Zur kenntnis der gesetz der gleitfunkenbildung," *Annalen der Physik*, vol. 326, no. 12, pp. 193-222, 1906.
- [Tow14] J. Townsend, *Electricity in Gases*, Oxford, Clarendon Press, 1914.
- [TTT+06] C. Tendero, C. Tixier, P. Tristant, J. Desmaison, and P. Leprince, "Atmospheric pressure plasmas: A review," *Spectrochimica Acta Part B: Atomic Spectroscopy*, vol. 61, no. 1, pp. 2-30, 2006.
- [Vla72] A. E. Vlastos, "The resistance of sparks", *Journal of Applied physics*, vol. 43, no. 4, pp.1987-1989, 1972.
- [VPR05] G. D. Vendelin, A. M. Pavio and U. L. Rohde, *Microwave Circuit Design Using Linear and Nonlinear Techniques*, Wiley-Blackwell, 2005.
- [Wal13] M. M. Walter, "Switching arcs in passive resonance HVDC circuit breakers," Doctoral dissertation, ETH Zurich, 2013.
- [WP17] P. R. Walsh, and M. M. Price, "Reducing Arc-Flash Hazards: Installing MV-Controllable Fuses on the Secondary Side of the Transformer in a Pumped Storage Plant," *IEEE Industry Applications Magazine*, vol. 23, no. 5, pp: 21-27, 2017.
- [Xia16] D. Xiao, *Gas discharge and gas insulation*, Shanghai, Shanghai Jiao

Tong University Press, 2016.

[XZY+11]

W. Xi-xiu, L. Zhen-Biao, T. Yun, M. Wenjun and X. Xun, "Investigate on the simulation of black-box arc model," *Proceedings of the 1<sup>st</sup> International Conference on Electric Power Equipment - Switching Technology*, Xi'an, China, Oct. 2011, pp. 629-636.



# Appendix A: Protective clothing and personal protective equipment

**Table A.1** Body Protection - Arc Flash [NFPA70E], [GSES15]

Incident Energy (cal/cm <sup>2</sup> )		Hazard/Risk Category	Clothing Description	Clothing Layers	Min Arc Rating of PPE and Min APTV Value of Clothing (cal/cm <sup>2</sup> )
From	To				
0	1.2	Category 0	Untreated Cotton, Shirt (Long Sleeve), Pants (Long)	1	N/A
1.2	4	Category 1	Arc Rated Long Sleeve Shirt & Pants or Coverall + Arc Rated Jacket, Parka, Rainwear, or Hard Hat Liner	1 or 2	4
4	8	Category 2	Arc Rated Long Sleeve Shirt & Pants or Coverall + Arc Rated Jacket, Parka, Rainwear, or Hard Hat Liner	1 or 2	8
8	25	Category 3	Arc Rated Long Sleeve Shirt & Pants or Coverall + Arc Flash Suit Hood, Jacket, Pants + Jacket, Arc Rated Parka, Rainwear, or Hard Hat Liner	2 or 3	25
25	40	Category 4	Arc Rated Long Sleeve Shirt & Pants or Coverall + Arc Flash Multi Layer Suit Hood, Jacket, Pants + Arc Rated Jacket, Parka, Rainwear, or Hard Hat Liner	3 or more	40

**Table A.2** Head, Hand and Foot Protection - Arc Flash [NFPA70E], [GSES15]

Incident Energy (cal/cm <sup>2</sup> )		Hazard/Risk Category	Head Protection Requirements	Hand and Foot Protection Requirements	Min PPE APTV Rating Required (cal/cm <sup>2</sup> )
From	To				
0	1.2	Category 0	Safety Glasses or Safety Goggles + Hearing Protection	Heavy Duty Leather Gloves	N/A
1.2	4	Category 1	Hard Hat, Safety Glasses or Safety Goggles, Arc Rated Face Shield or Suit Hood + Hearing Protection	Heavy Duty Leather Gloves, Leather Work Shoes	4
4	8	Category 2	Hard Hat, Safety Glasses or Safety Goggles, Arc Rated Face Shield and Balaclava or Suit Hood + Hearing Protection	Heavy Duty Leather Gloves, Leather Work Shoes	8
8	25	Category 3	Hard Hat, Safety Glasses or Safety Goggles, Arc Rated Arc Flash Suit Hood + Hearing Protection	Arc Rated Gloves, Leather Work Shoes	25
25	40	Category 4	Hard Hat, Safety Glasses or Safety Goggles, Arc Rated Arc Flash Suit Hood + Hearing Protection	Arc Rated Gloves, Leather Work Shoes	40
> 40	PPE alone cannot provide adequate protection. Use special procedures and arrange permission, similar to testing and prohibit live working				

Note: ATPV is the minimum Arc Thermal Performance Value or Break open Threshold Energy rating of PPE fabric. This is defined as the standard test method for flame resistant fabrics as the incident energy that would just cause a second-degree burn (1.2 cal/cm<sup>2</sup>).

Note: Face shields (visors) made of polycarbonate material is more appropriate for use in situations with relatively low radiation exposure and protect against projectile impact. Safety glasses and goggles provide lesser protection, but in low risk tasks they may be justified if the task involves substantial physical work in combination with good visual requirements. Eye protection (safety glasses or goggles) shall always be worn under face shields or hoods regardless of the chosen head protection.

Note: For tasks requiring a Category 2 or higher clothing system, a face shield is unacceptable and a flame resistant hood with a long flame resistant bib and polycarbonate window, safety glasses, and hard hat should be used.

Note: Heavy duty leather work shoes normally provide a significant degree of protection to the feet. They are recommended for all tasks and shall be used for incident energy exposure levels 4 cal/cm<sup>2</sup> and higher (Hazard/Risk Category 2 and higher).

# Appendix B: PCS equivalent constant resistance

The plasma closing switch, PCS, which was inserted in series with the capacitor in the WGS topology, serves to release the required energy for the short transient arc discharge across the WGS. Thus, it is critical to model the PCS electrical behaviour in order to proceed with the subsequent analysis and to extract the electrical characteristics of the arc discharge across the wire-guided spark gap.

As it was mentioned in Chapter 4, the inter-electrode gap length of the PCS was 4 mm and this value was selected to limit the breakdown voltage to <20 kV and the energy available in the discharge to <10 J. For the purposes of the present study the PCS was assumed a time-independent passive circuit element with linear characteristics. It was also assumed to be a purely resistive element. In order to calculate its resistance value (constant resistance of plasma in the switch), the methodology developed by Greason [Gre97] is used in the present work.

To determine the electrical parameters, voltage across, current through and plasma resistance of the PCS alone, the WGS was excluded from the test system by setting a 0-mm gap, i.e. the WGS electrodes were in contact, and the copper wire was absent (nodes 5 – 6), Figure B.1.

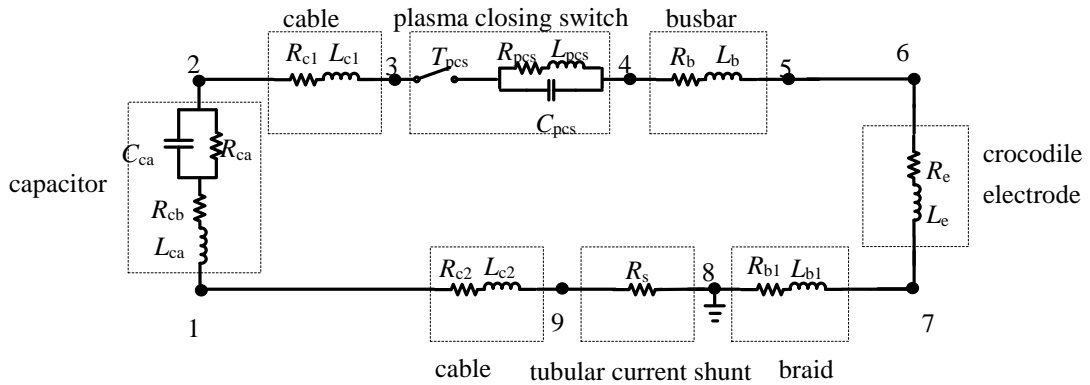


**Figure B.1** Lumped element model for 0-mm wire-guided spark gap length.

Typical voltage and current waveforms of the PCS are given in Figure B.2. Current waveform is being used to calculate the PCS resistance followed the method described in [Gre97].

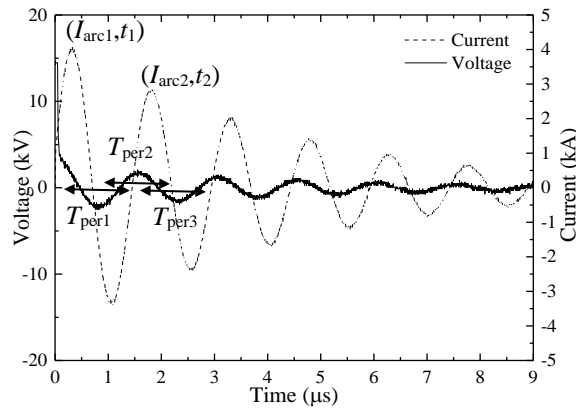


**Figure B.2** Voltage and current waveforms for the plasma closing switch with inter-electrode gap of 4 mm, acquired to calculate the energy losses in the switch.

The equivalent constant resistance of the circuit with the PCS only,  $R_{\text{pcs}}$ , consists of two components: the constant resistance of the spark discharge in this gap,  $R_{\text{spark}}$ , and the stray resistance of the remaining circuit,  $R_{\text{stray}}$ :  $R_{\text{pcs}} = R_{\text{spark}} + R_{\text{stray}}$ .  $R_{\text{pcs}}$  was calculated following the methodology described in Section III when the inter-electrode gap in the WGSG was 0 mm, as stated above. The average value of  $R_{\text{pcs}}$  was calculated using 5 independent measurements and found to be  $0.3 \Omega$  with a standard deviation value of  $0.01 \Omega$ . The methodology described in Subchapter 5.4, Equation (5.17) – Equation (5.23) are followed to extract the equivalent constant resistance for a single spark and the results presented in Table B.1.

**Table B.1** Equivalent constant resistance results for a single spark measurement across the PCS.

Variable	Value
$C$ [nF]	80
$I_{\text{arc1}}$ [kA]	4.129
$I_{\text{arc2}}$ [kA]	2.875
$t_1$ [ $\mu\text{s}$ ]	0.290
$t_2$ [ $\mu\text{s}$ ]	1.784
$T_{\text{per}}$ [ $\mu\text{s}$ ]	1.474
$R_d$ [ $\Omega$ ]	0.334
$R_{\text{eqarc}}$ [ $\Omega$ ]	<b>0.309</b>

# Appendix C: Example of obtaining arc current waveform (SBSG topology)

Figure C.1 shows the location of the current sensing resistor with the compensating capacitor in parallel where the voltage waveform is acquired. Figure C.2 shows an example of the acquired voltage waveform for 0.5 mm gap length and 1.9 nF capacitor through the current sensing resistor. An exponentially damped equation is fitted to the measured voltage waveform and the 1<sup>st</sup> order ordinary differential equation (ODE) is formed, Equation (5.14). The current sensing resistor, according to the manufacturing datasheet, is a low inductive resistor having,  $L_s = 0.7$  nH inductance value and resistance value,  $R_s = 25$  m $\Omega$ . The first order differential equation is solved obtaining the arc current waveform,  $I_{arc}$ , with the aid of MATLAB ( $I_{arc}(0)$  is assumed 0).

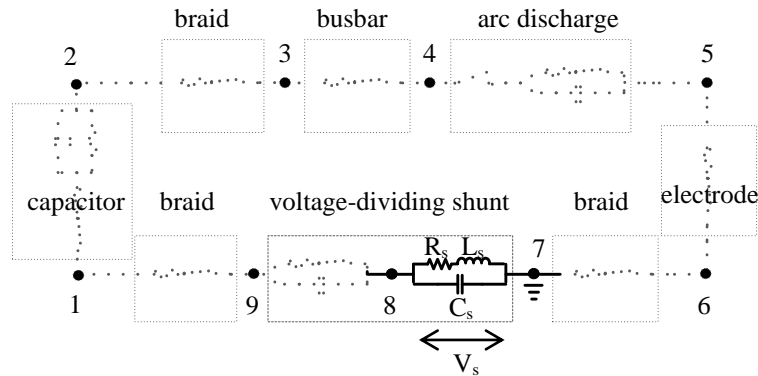


**Figure C.1** Location of the current sensing resistor with the compensating capacitor in parallel.

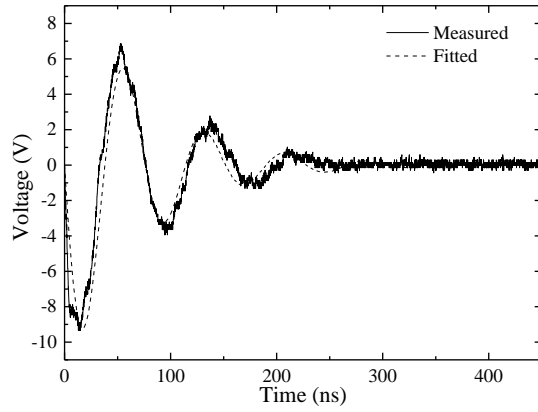


**Figure C.2** Voltage waveform acquired for 0.5 mm gap length and 1.9 nF capacitor and the fitted curve ( $V_s(t) = V_0 \sin(\omega t) e^{-\zeta t}$ ) used to form the ODE to extract the arc current.

After breakdown in the SBSG the current waveform,  $I_{arc}(t)$ , is described by an exponentially-damped sinusoidal function, equations (5.17) to (5.20), Figure C.3.

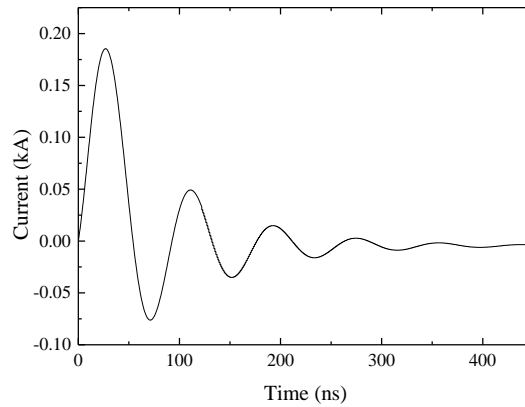


**Figure C.3** Extracted arc current waveform, the solution of the ODE, for 0.5 mm gap length and 1.9 nF capacitor.

The leakage current passing through the 1 nF capacitor placed in parallel with the current sensing resistor for compensating reasons was calculated ( $I_{C_s}(t) = C_s dV_s/dt$ ). The leakage current found to be  $\sim 0.4\%$  of the total current of the circuit, thus it was neglected considering the total current of the circuit as the arc current.



# Appendix D: List of publications

## Published journal paper

S. G. Koutoula, I. V. Timoshkin, M. D. Judd, S. J. MacGregor, M. P. Wilson, M. J. Given, T. Wang and E. I. Harrison, "A study of energy partition during arc initiation," *IEEE Transactions on Plasma Science*, vol. 44, no. 10, pp. 2137-2144, Oct. 2016.

## Journal paper in preparation

S. G. Koutoula, I. V. Timoshkin, S. J. MacGregor, M. P. Wilson, M. J. Given and T. Wang, "Black-box approach to modelling the initial stage of the arc", *in preparation to be submitted to IEEE Transactions on Dielectrics and Electrical Insulation*, 2018.

## Published conference presentations and papers

S. Koutoula, E. Harrison and M. Judd, "Arc Flash: Review of Studies and an Approach to Risk Management", *Proceedings of the 11<sup>th</sup> Annual Euro TechCon Conference and Expo*, Glasgow, UK, Nov. 2013. (paper)

S. Koutoula, E. Harrison and M. Judd, "Approaches to Arc Flash Hazard Assessment", *presented in the 7<sup>th</sup> UHVnet Colloquium*, Guildford, UK, Jan. 2014. (poster)

S. Koutoula, I. Timoshkin, N. Roscoe, M. Judd and E. Harrison, "Investigating the resistance of an electrical spark", *presented in the 8<sup>th</sup> UHVnet Colloquium*, Stafford, UK, Jan. 2015. (poster)

S. G. Koutoula, M. D. Judd, I. V. Timoshkin and E. I. Harrison, "Investigating Ways to Prevent Electrical Arc Flash", *Proceedings of the 12<sup>th</sup> Petroleum and Chemical Industry Committee Conference Europe*, London, UK, June 2015. (paper)

E. Harrison, P. Welford, M. Judd and S. Koutoula, "An Overview of Arc Flash Hazard Assessments and Mitigation Studies", *Proceedings of the Arc Flash & Isolation Safety Conference*, Manchester, UK, June 2015. (paper)

S.G.Koutoula, I.V.Timoshkin, M.D.Judd, S.J.MacGregor, M.P.Wilson, M.J.Given, T.Wang and E.I.Harrison, "Transient arcing process: Energy components and associated risks", *presented in the 9<sup>th</sup> UHVnet Colloquium*, Cardiff, UK, Jan. 2016. (poster)

## Student presentation competition

Presentation title: "Energy dissipation and partition during an electrical discharge initiation", *Student Presentation Competition by the Institute for Energy and Environment, University of Strathclyde and IEEE Power & Energy Society - UK and Ireland Chapter*, Glasgow, Sep. 2015. (won the runner up prize)